

**Mesoscale Saturated & Unsaturated Poroelasticity of  
Highly Heterogeneous Porous Solids- Discrete Solid &  
Fluid Descriptions**

by

Siavash Khosh Sokhan Monfared

B.S., University of Oklahoma (2012)

S.M., Massachusetts Institute of Technology (2015)



Submitted to the Department of Civil and Environmental Engineering  
in partial fulfillment of the requirements for the degree of

Doctor of Philosophy in Civil and Environmental Engineering

at the

MASSACHUSETTS INSTITUTE OF TECHNOLOGY

June 2019

© Massachusetts Institute of Technology 2019. All rights reserved.

**Signature redacted**

Author.....  
Department of Civil and Environmental Engineering  
March 27, 2019

Certified by.....  
**Signature redacted**  
Franz-Josef Ulm  
Professor of Civil and Environmental Engineering  
Thesis Supervisor

Accepted by.....  
**Signature redacted**  
Heidi Nepf  
Donald and Martha Harleman Professor of Civil and Environmental  
Engineering, Chair, Graduate Program Committee



# **Mesoscale Saturated & Unsaturated Poroelasticity of Highly Heterogeneous Porous Solids- Discrete Solid & Fluid Descriptions**

by

Siavash Khosh Sokhan Monfared

Submitted to the Department of Civil and Environmental Engineering  
on March 27, 2019, in partial fulfillment of the  
requirements for the degree of  
Doctor of Philosophy in Civil and Environmental Engineering

## **Abstract**

The capacity of the continuum approach to capture the effective poromechanical response of highly heterogeneous porous solids is limited. Specifically, the mean-field theories of continuum micromechanics cannot capture the full spatial variations of mechanical properties and restricted to scale separability. Additionally, any approach to unsaturated poromechanics requires a description for fluids that accounts for confinement, temperature variations and the strength of fluid-fluid and fluid-solid interactions. Most prevailing models are phenomenological in approach and hinge on the concept of effective stress for capturing liquid and gas interactions with solid(s). Thus, a framework is implemented based on discrete descriptions for solids and fluids. The behavior of solids is captured through Lattice Element Method. This method utilizes a finite number of mass points, each interacting with their nearest neighbors through linear or non-linear effective interaction potentials while capable to account for anisotropy. The fluid behavior is described in the grand canonical ensemble in a statistical mechanics approach which paves the way to study the behavior of confined fluids while providing access to the capillary stress tensorial field in the pore domain. The two descriptions are brought together via a local pore pressure force formulation that links capillary pressures to solid deformation. For the case of fully saturated poroelasticity, generalized discrete expressions for Biot poroelastic coefficients defined in statistical mechanics ensembles are presented. The developed theoretical model and its implementation are validated on simple porous media for which micromechanics based solution exist. By way of application to real heterogeneous materials imported from computed tomography (CT) scans, a methodology is presented to merge lab-measured nanoindentation data and CT scans into the developed computational framework. Finally, capillary condensation in disordered granular packings is studied. The results provide insights into confined fluid behavior, fluid criticality, the interplay of disorder, temperature and capillary stress fields as well as liquid clustering formation, growth and coalescence.

Thesis Supervisor: Franz-Josef Ulm

Title: Professor of Civil and Environmental Engineering



## Acknowledgments

I am truly grateful to my advisor, Franz-Josef Ulm, for his unconditional support and guidance. Sharing Franz's passion for poromechanics, it has been an elating experience working with him on a topic that is near and dear to his heart. I am also indebted to Roland J.-M. Pellenq who helped me ease my way into physics and statistical mechanics. Without Roland, it's hard to imagine that I would have overcome some of the challenges I faced in pursuit of this thesis. Together, Franz and Roland have created a rich and diverse research community with many national and international collaborations. This is how I came to work with Farhang Radjai who profoundly shaped my graduate research experience. Farhang's influence can be seen in every chapter of this thesis. I am thankful to Ken Kamrin, my external committee member, who despite his many commitments provided me with insightful comments that helped shape this thesis.

I would like to thank Hadrien Laubie, my main collaborator during my graduate studies - a world class mechanic turned a world class pilot. I am also grateful to Sina Moeini Ardakani. Sina's confidence in approaching seemingly impossible tasks has been a source of inspiration for me. Without his encouragement and support, I would have not considered parallelizing LEM. I am thankful to Tingtao Zhou whose enthusiasm for a wide range of scientific phenomena has broaden my horizons. I should also thank Kiley Clapper, Donna Hudson, Melody Abedinejad and Jeanette Marchocki for their support and kindness throughout these years.

Last but by no means least, I deeply appreciate my fiancé, Bridget. She was the light at the end of the tunnel everyday as I wrestled with equations and codes during these years. I have cherished every moment we have spent together and excited for the future ahead of us.

THIS PAGE INTENTIONALLY LEFT BLANK

# Contents

<b>1</b>	<b>Introduction</b>	<b>21</b>
1.1	General Context . . . . .	21
1.2	Research Objectives & Approach . . . . .	23
1.3	Thesis Outline . . . . .	24
<b>2</b>	<b>Discrete Solid Description: Effective Potentials &amp; Elastic Properties in Lattice Element Method</b>	<b>27</b>
2.1	Lattice Element Method . . . . .	28
2.1.1	Lattice & Network . . . . .	28
2.1.2	Interaction Potentials . . . . .	29
2.2	Effective Elastic Properties . . . . .	33
2.2.1	From Microscopic Link Properties to Macroscopic Effective Behavior	33
2.2.2	Cubic & Isotropic Elastic Symmetries . . . . .	35
2.2.3	Transversely Isotropic Elastic Symmetry . . . . .	37
2.3	Numerical Implementation . . . . .	39
2.4	Validation . . . . .	41
2.4.1	Continuum Micromechanics Reference Solutions . . . . .	41
2.4.2	Validation Results . . . . .	43
2.5	Chapter Summary . . . . .	45
<b>3</b>	<b>Mesoscale Poroelasticity of Heterogeneous Porous Solids - Fully Saturated Case</b>	<b>47</b>
3.1	Effective Pore-Pressure Force Field Potential . . . . .	49
3.2	Poroelastic Properties and Ensemble Definitions . . . . .	51

3.2.1	Drained Elasticity Properties in the $NVT$ -Ensemble . . . . .	52
3.2.2	Biot Pore Pressure Coefficients in the $\mu VT$ -Ensemble . . . . .	52
3.2.3	Biot Modulus in the $NPT$ -Ensemble . . . . .	54
3.3	Application . . . . .	56
3.3.1	Solid Potential Parameter Calibration . . . . .	56
3.3.2	Continuum Microporomechanics Reference Solutions . . . . .	57
3.3.3	Validation Results . . . . .	58
3.4	Discussions . . . . .	63
3.5	Chapter Summary . . . . .	65
<b>4</b>	<b>Application to Real Heterogeneous Porous Media from Imported Computed Tomography Scans</b>	<b>69</b>
4.1	Materials . . . . .	71
4.1.1	Calibration & Validation Structure Sets . . . . .	72
4.2	Methodology for Calibrations of Energy Parameters . . . . .	73
4.2.1	Input Elasticity of the Organic Phase . . . . .	77
4.2.2	Degrees of Freedom: Clay and Inclusion Effective Potentials . . . . .	78
4.2.3	Numerical Optimization . . . . .	81
4.3	Results . . . . .	82
4.3.1	Calibration & Validation Results . . . . .	82
4.3.2	Biot Poroelastic Coefficients . . . . .	86
4.3.3	Interface Behavior Sensitivity Analysis . . . . .	88
4.3.4	Stress Transmission . . . . .	89
4.4	Discussions . . . . .	96
4.5	Chapter Summary . . . . .	100
<b>5</b>	<b>Temperature Dependent Capillary Pressure Fields in Disordered Confinement</b>	<b>101</b>
5.1	Introduction . . . . .	101
5.2	Materials & Methods . . . . .	103
5.2.1	Monodisperse Particle Packings . . . . .	103
5.2.2	Discrete Fluid Description . . . . .	108

5.3	Results . . . . .	118
5.3.1	Criticality & Confinement . . . . .	118
5.3.2	Capillary Pressure in Disordered Granular Packings . . . . .	122
5.3.3	Liquid Texturing & Morphology . . . . .	124
5.3.4	Poromechanics of Unsaturated Media . . . . .	124
5.4	Discussions . . . . .	127
5.5	Chapter Summary . . . . .	135
<b>6</b>	<b>Conclusions</b>	<b>137</b>
6.1	Summary of Main Findings . . . . .	137
6.2	Limitations & Future Perspectives . . . . .	139
<b>A</b>	<b>Global to Local Coordinate Transformation</b>	<b>141</b>
<b>B</b>	<b>Nodal Displacements for Uniform Imposed Deformation</b>	<b>143</b>
<b>C</b>	<b>Hill Concentration Tensor</b>	<b>145</b>
C.1	Spheroidal Inclusion in an Isotropic Medium . . . . .	146
C.2	Spheroidal Inclusion in a Transversely Isotropic Medium . . . . .	146

**THIS PAGE INTENTIONALLY LEFT BLANK**

# List of Figures

2-1	2-1a: D3Q26 network for a unit cell; 2-1b: simple cubic lattice for material discretization. . . . .	28
2-2	Translational and rotational degrees of freedom associated with a bond element between nodes $i$ and $j$ in the local coordinate system. . . . .	29
2-3	Superposition of lattice and material representation. After discretization of the material domain, calibrated energy parameters are assigned to solid phase(s). . . . .	33
2-4	Schematics for a set of structures used for validation. Each structure contains a centric spherical pore. A range of pore radii are used to achieve different porosities. . . . .	39
2-5	Validation of closed form calibration expressions (Theoretical) against numerical implementation from LEM (Numerical) for the isotropic case (2-5a) and transversely isotropic case (2-5b and 2-5c). . . . .	42
2-6	$C_{ij}$ - in Voigt's notations - variations versus $R/L$ for the isotropic case (2-6a) and transversely isotropic case (2-6b). "MT" refers to Mori-Tanaka continuum solution whereas "LEM" represents discrete simulations. . . . .	43
3-1	Radial - $\tilde{\sigma}_{rr} = \sigma_{rr}/M_s$ - (3-1a) and tangential - $\tilde{\sigma}_{\theta\theta} = \sigma_{\theta\theta}/M_s$ - stresses (3-1b) corresponding to Lamé's problem calculated from analytical solutions and numerical simulations. $M_s$ is the imposed isotropic indention modulus for the solid shell. . . . .	49

3-2	Normalized bulk (3-2a) and shear (3-2b) moduli, normalized indentation moduli (3-2c and 3-2d); $\delta_{iso}$ (3-2e) and $\delta_{ti}$ (3-2f) versus $R/L$ for isotropic and transversely isotropic cases, respectively. "MT" refers to Mori-Tanaka continuum solution whereas "LEM" represents discrete simulations. . . . .	60
3-3	These plots correspond to the isotropic solid case. 3-3a: Simulated $b$ labeled as "LEM ( $\mu VT$ )", continuum based $b$ calculated from effective elasticity obtained from simulations in LEM, labeled as "Direct" and $b$ estimated from Mori-Tanaka labeled as "MT". 3-3b: $N$ with simulated $b$ labeled as "LEM ( $NPT^*$ )", with calculated $b$ determined directly from simulations in LEM, labeled as "LEM ( $NPT^{**}$ )". $N$ from Mori-Tanaka estimation is labeled as "MT". . . . .	61
3-4	These plots correspond to the transversely isotropic solid case. 3-4a and 3-4b: Simulated $b_1$ and $b_3$ labeled as "LEM ( $\mu VT$ )", continuum based $b_1$ and $b_3$ using effective elasticity obtained from direct simulations, labeled as "Direct" and the Mori-Tanaka estimations labeled as "MT". 3-4c: $N$ using $b$ from simulations labeled as "LEM ( $NPT^*$ )" and from $b$ obtained through direct effective elasticity simulations labeled as "LEM ( $NPT^{**}$ )". The Mori-Tanaka estimation for $N$ is labeled as "MT". . . . .	62
3-5	Probability density functions of $\sigma_{xx}/p$ in the $\mu VT$ ensemble for the considered matrix-pore structures for a transversely isotropic solid. Among the three $R/L$ ratios plotted, one can observed the long distribution tails for $R/L = 0.443$ , indicative of high stress concentration between the pore wall and simulation boundary box. . . . .	62
4-1	A cross-section of scan B displaying raw CT data (left) and the segmented image (right). . . . .	72
4-2	Probability density functions for the volume fraction of the considered four phases as a function of coarse-graining length-scale $\lambda$ in scan A. . . . .	73
4-3	Probability density functions for the volume fraction of the considered four phases as a function of coarse-graining length-scale $\lambda$ in scan B. . . . .	74

4-4	Probability density (4-4a and 4-4b), cumulative probability density (4-4c and 4-4d) and quantile-quantile plots (4-4e and 4-4f) for experimentally measured nanoindentation moduli for scan A with fitted Lognormal, Stable and non-parametric normal kernel distributions. . . . .	75
4-5	Probability density (4-5a and 4-5b), cumulative probability density (4-5c and 4-5d) and quantile-quantile plots (4-5e and 4-5f) for experimentally measured nanoindentation moduli for scan B with fitted Lognormal, Stable and non-parametric normal kernel distributions. . . . .	76
4-6	Mineralogical composition of the inclusions phase from XRD data as reported in [92] for scan A (4-6a) and scan B(4-6b). . . . .	80
4-7	4-7a: Cross-section of a discretized sub-volume extracted from CT scans. Colors Red, Orange, Blue and Gray correspond to inclusions, clay, pore and kerogen phases respectively.; 4-7b: Color map for $\epsilon_1^n$ variations in the inclusions phase as shown in 4-7a ; 4-7c: Weibull distribution of $\epsilon_1^n$ energy parameter, as an example, shown spatially in 4-7b. . . . .	80
4-8	Optimized and experimentally measured $\langle M_1 \rangle_c, \langle M_1^2 \rangle_c^{0.5}, \langle M_3 \rangle_c$ and $\langle M_3^2 \rangle_c^{0.5}$ for scans A and B. . . . .	82
4-9	Probability density and cumulative probability density functions for optimized shape factors, $\{\alpha_i\}$ , and scale factors, $\{\beta_i\}$ , characterizing the Weibull distributions for the inclusions phase for scan A (4-9a,4-9c,4-9e and 4-9g) and scan B (4-9b,4-9d,4-9f and 4-9h). . . . .	83
4-10	Distributions of calibrated isotropic elasticity ( $M^{inc}, \nu^{inc}$ ) of the inclusions phase with three-components Gaussian-mixture model fits for $M^{inc}$ for scan A (4-10a and 4-10c) and scan B (4-10b and 4-10d). See Tab. 4.2 for three-component Gaussian-mixture model fitting parameters. . . . .	84
4-11	Distributions of calibrated quasi-transversely isotropic ( $M_1, M_3, K_{VRH}, G_{VRH}$ ) for the clay phase with normal fits for scan A (4-11a, 4-11c, 4-11e and 4-11g) and scan B (4-11b, 4-11d, 4-11f and 4-11h). . . . .	85

4-12	Probability density (4-12a and 4-12b) and cumulative probability density (4-12c and 4-12d) of scan A for simulated indentation moduli and experimentally measured nanoindentation moduli using validation structure set in a forward application for validation. . . . .	86
4-13	Probability density (4-13a and 4-13b) and cumulative probability density (4-13c and 4-13d) of scan B for simulated indentation moduli and experimentally measured nanoindentation moduli using validation structure set in a forward application for validation. . . . .	87
4-14	Probability density (4-14a, 4-14b and 4-14c), cumulative probability density (4-14d, 4-14e and 4-14f) and quantile-quantile plots (4-14g, 4-14h and 4-14i) for simulated Biot pore-pressure coefficients $b_1$ , $b_2$ , $b_3$ for scan A with fitted Weibull and Stable distributions. . . . .	90
4-15	Probability density (4-15a, 4-15b and 4-15c), cumulative probability density (4-15d, 4-15e and 4-15f) and quantile-quantile plots (4-15g, 4-15h and 4-15i) for simulated Biot pore-pressure coefficients $b_1$ , $b_2$ , $b_3$ for scan B with fitted Weibull and Stable distributions. . . . .	91
4-16	The distributions for Biot solid modulus for scan A (4-16a) and scan B (4-16b). . . . .	92
4-17	Distributions for simulated indentation moduli, $M_1$ as shown in 4-17a and $M_3$ as shown in 4-17b, for different interface models. . . . .	92
4-18	Pair-correlation function for clay, pore, kerogen and inclusions phases corresponding to sub-volumes of size $150 \times 150 \times 150$ voxels. . . . .	93
4-19	Percolating stress path in $\vec{e}_1$ and for scan A (4-19a), for scan B (4-19b), in $\vec{e}_2$ and for scan A (4-19c) and scan B (4-19d), in $\vec{e}_3$ and for scan A (4-19e) and scan B (4-19f). Colors Red and Orange indicate inclusions and clay phases, respectively. 4-19g defines the coordinate system. . . . .	94
4-20	Radial distribution function for the percolated stress path due to imposed uniaxial displacement in different directions for scan A (4-20a, 4-20b, 4-20c) and scan B (4-20d, 4-20e, 4-20f). . . . .	95

4-21	Coarse-grained stresses for different $\lambda$ for scan A with five realizations for inclusions stiffness, labeld as cases $A - E$ . 4-21a, 4-21b, 4-21c, 4-21d correspond to coarse-grained stresses, $\sigma_{11}$ due to $\vec{\xi}^d = \xi^d \vec{e}_1$ ; 4-21e, 4-21f, 4-21g, 4-21h correspond to coarse-grained stresses, $\sigma_{22}$ due to $\vec{\xi}^d = \xi^d \vec{e}_2$ and 4-21i, 4-21j, 4-21k, 4-21l correspond to coarse-grained stresses, $\sigma_{33}$ due to $\vec{\xi}^d = \xi^d \vec{e}_3$ . . . . .	96
4-22	Coarse-grained stresses for different $\lambda$ for scan B with five realizations for inclusions stiffness, labeld as cases $A - E$ . 4-22a, 4-22b, 4-22c, 4-22d correspond to coarse-grained stresses, $\sigma_{11}$ due to $\vec{\xi}^d = \xi^d \vec{e}_1$ ; 4-22e, 4-22f, 4-22g, 4-22h correspond to coarse-grained stresses, $\sigma_{22}$ due to $\vec{\xi}^d = \xi^d \vec{e}_2$ and 4-22i, 4-22j, 4-22k, 4-22l correspond to coarse-grained stresses, $\sigma_{33}$ due to $\vec{\xi}^d = \xi^d \vec{e}_3$ . . . . .	97
5-1	Type A structures - $\lambda^A = 1.064$ (5-1a), $\lambda^A = 1.021$ (5-1b), $\lambda^A = 1.0$ (5-1c) and Type B structures - $\lambda^B = 0.2$ (5-1d), $\lambda^B = 0.5$ (5-1e) and $\lambda^B = 1.0$ (5-1f). The voronoi cell tessellations were created using Voropp [107]. . . .	103
5-2	Radial distribution function $g(r)$ for Type A (5-2a) and Type B (5-2b) structures. . . . .	104
5-3	Distributions for $m_\eta$ computed at different coarse graining scale for Type A (5-3a) and Type B (5-3b) structures. . . . .	104
5-4	Pore size (radius $r_p$ ) distributions for Type A (5-4a) and Type B (5-4b) structures. . . . .	106
5-5	Averaged statistical descriptors, mean (5-5a), variance (5-5b), skewness (5-5c) and kurtosis (5-5d) plotted against the corresponding coarse-graining length scale $\ell_{cg}$ for Type A and B structures. . . . .	107
5-6	Isotherms for bulk fluid for different temperatures. The critical point of bulk fluid for a simple cubic lattice ( $\tilde{T} = 1.5, \rho_c = 0.5$ ) is captured. . . . .	109

5-7	Density map for sorption in cylindrical pores (in 3D) with lengths $L_x = 100$ , $L_y = L_z = 8$ , radius $R = 6$ , lattice-spacing $a_0 = 1.0$ , and reservoir length $L_x^{\text{res}} = 4$ added at the ends of the pore. The cross-sections correspond to $z = L_z/2 = 4$ and $y = 3.0, \tilde{T} = 1.2$ (5-7a), $y = 3.0, \tilde{T} = 1.4$ (5-7b), $y = 0.5, \tilde{T} = 1.2$ (5-7c) and $y = 0.5, \tilde{T} = 1.4$ (5-7d). The external reservoir is initiated and kept at $\rho = 1$ for 5-7c and 5-7d while it evolves with the cylindrical pore for 5-7a and 5-7b. . . . .	110
5-8	Isotherms for different structures and $\tilde{T}$ . . . . .	111
5-9	First cumulant of capillary pressure field as it evolves with imposed chemical potential $\mu$ for different structures and temperatures. . . . .	112
5-10	Second cumulant of capillary pressure field as it evolves with imposed chemical potential $\mu$ for different structures and temperatures. . . . .	113
5-11	Skewness of capillary pressure field as it evolves with imposed chemical potential $\mu$ for different structures and temperatures. . . . .	114
5-12	Kurtosis of capillary pressure field as it evolves with imposed chemical potential $\mu$ for different structures and temperatures. . . . .	115
5-13	Coarse-grained mean for capillary pressure field for all structures and temperatures $\tilde{T} = 0.8$ (5-13a), $\tilde{T} = 1.0$ (5-13b), $\tilde{T} = 1.2$ (5-13c), $\tilde{T} = 1.4$ (5-13d) and $\tilde{T} = 1.5$ (5-13e) plotted against the corresponding coarse-graining length scale $\ell_{cg}$ at $h = 0.90$ . . . . .	119
5-14	Coarse-grained variance for capillary pressure field for all structures and temperatures $\tilde{T} = 0.8$ (5-14a), $\tilde{T} = 1.0$ (5-14b), $\tilde{T} = 1.2$ (5-14c), $\tilde{T} = 1.4$ (5-14d) and $\tilde{T} = 1.5$ (5-14e) plotted against the corresponding coarse-graining length scale $\ell_{cg}$ at $h = 0.90$ . . . . .	120
5-15	Distributions for $m_p$ computed at different coarse-graining length scale for different structures, $\tilde{T} = 1.2$ and $h = 0.90$ . . . . .	121
5-16	Shift in capillary critical temperature $T_{cc}$ as a function of $2\sigma/R_p$ . . . . .	122
5-17	Shift in capillary critical temperature $T_{cc}$ as a function of $\lambda^A$ and $\lambda^B$ for an initial assessment of confinement effects on $T_{cc}$ . . . . .	123

5-18	Radial - $\tilde{\sigma}_{rr} = \sigma_{rr}/M_s$ - (5-18a) and tangential - $\tilde{\sigma}_{\theta\theta} = \sigma_{\theta\theta}/M_s$ - stresses (5-18b) corresponding to Lamé's problem calculated from analytical solutions and numerical simulations. $M_s$ is the imposed isotropic indentation modulus for the solid shell. . . . .	127
5-19	Number of clusters at different relative humidities for $\lambda^A = 1.064$ (5-19a), $\lambda^A = 1.021$ (5-19b) and $\lambda^A = 1.0$ . . . . .	127
5-20	First moment of cluster volume, $V_c$ (in voxels) normalized by the total simulation box volume $V$ for $\lambda^A = 1.064$ (5-20a), $\lambda^A = 1.021$ (5-20b) and $\lambda^A = 1.0$ . . . . .	128
5-21	Visualizations for liquid clusters for $\lambda^A = 1.0$ , $\tilde{T} = 0.80$ and for $h = 0.82$ (5-21a), $h = 0.84$ (5-21b), $h = 0.88$ (5-21c), $h = 0.90$ (5-21d), $h = 0.94$ (5-21e) and $h = 0.98$ (5-21f). . . . .	128
5-22	Cross-sections at $z = 44$ , $\lambda^A = 1.0$ , $h = 0.91$ and for $\tilde{T} = 0.8$ (5-22a), $\tilde{T} = 1.0$ (5-22b), $\tilde{T} = 1.2$ (5-22c), $\tilde{T} = 1.4$ (5-22d) and $\tilde{T} = 1.5$ (5-22e). . . .	129
5-23	Cross-sections at $z = 44$ , $\lambda^B = 0.20$ , $h = 0.82$ and for $\tilde{T} = 0.8$ (5-23a), $\tilde{T} = 1.0$ (5-23b), $\tilde{T} = 1.2$ (5-23c), $\tilde{T} = 1.4$ (5-23d) and $\tilde{T} = 1.5$ (5-23e). . . .	130
5-24	Cross-section at $z = 40$ and for $h = 0.85$ displaying normalized density (5-24a), capillary pressure (5-24b) and solid stresses $\sigma_{zz}$ induced by $\langle p \rangle$ (5-24c) and $p(\vec{x})$ (5-24b). . . . .	131
5-25	PDFs for solid stresses $\sigma_{zz}$ induced by $\langle p \rangle$ and $p(\vec{x})$ for $h = 0.8$ (5-25a), $h = 0.85$ (5-25b), $h = 0.88$ (5-25c) and $h = 0.90$ (5-25d). . . . .	132
5-26	The mean, $m_p$ evolution of capillary pressure field (in real units) with $p/p_{sat} = \exp(\mu - \mu_{sat}) / k_B T$ for different structures at $\tilde{T} = 1.2$ . . . . .	133

THIS PAGE INTENTIONALLY LEFT BLANK

# List of Tables

2.1	Link index, length, number and energy parameters for isotropic and transversely isotropic elastic symmetries for the D3Q26 lattice and D3Q18 (first 9 lines) lattice. . . . .	33
2.2	Expressions for calibrations of the elastic energy content of the finite sized simulation box in terms of energy parameters. . . . .	38
4.1	First and second cumulants of the distributions of indentation moduli of calibration structure set and experimentally measured. . . . .	82
4.2	Three component Gaussian-mixture model fitting parameters for the isotropic indentation modulus, $M$ , of the inclusion phase for scans A and B as shown in Fig. 4-10. $\mu_i$ [GPa] denotes the mean of the $i^{th}$ -component and $w_i$ the associated weight. . . . .	88
4.3	First and second cumulants of the distributions of indentation moduli of validation structure set and experimentally measured. . . . .	89
4.4	First and second cumulants of the distributions for Biot poroelastic coefficients.	92
4.5	Ratio of mean stresses to stress threshold for a given direction of applied load.	95

**THIS PAGE INTENTIONALLY LEFT BLANK**

# Chapter 1

## Introduction

### 1.1 General Context

The response of a porous continuum comprised of a heterogeneous solid backbone to external perturbations such as fluid pressure or some other physical chemistry phenomena at the pore scale such as adsorption often involves addressing a multitude of coupled multi-physics responses, spanning a range of time and length scales. Resolving the physics of fluid-solid interactions at the pore scale is a fundamental step towards understanding physical phenomena such as wave propagation [23], fracture [59, 79], earthquakes [65], adsorption [38], capillary condensation and liquid-gas phase transition [117], wet granular mixing [19, 108, 50], cell mechanics [28, 89], biomechanics [39, 57], plant movement [115, 46] and relevant for applications such as carbon sequestration [120], geothermal energy extraction and hydraulic fracturing while providing a pathway to engineer materials with prescribed functionalities for drug delivery, tissue engineering and additive manufacturing to name a few.

A particularly challenging case in poromechanics involves capturing the interactions between a heterogeneous fluid and a heterogeneous solid wall. Gaining insights into such a system require a description of a fluid in confinement while accounting for temperature effects as well as the strength of fluid-fluid and fluid-solid interactions. At the same time, one needs a framework to describe the mechanics of a heterogeneous solid. Lastly, the fluid

and solid descriptions need to be merged to resolve induced solid deformation (and stresses) by accounting for the mechanical work with pressure-volume as (thermodynamic) conjugate coordinates [16, 106] and/or surface tension-area in case of a thin-film formation for e.g. during adsorption [127, 25] or chemical work with chemical potential-particle density as its conjugate coordinates [36, 5]. Typical approaches to the mechanics of unsaturated porous media involve an effective stress definition that is tasked to encapsulate the independent interactions of liquid and gas phases with the solid wall [18, 29, 37]. Such concept is directly linked to the behavior of a confined fluid which is significantly different than a bulk fluid. This is mainly due to constraints introduced by pore topology and the strength of fluid-solid (wall) interactions that alters the energy landscape of a fluid. However, the role of confinement on fluid criticality and the nature of capillary condensation as a phase transition (first order vs. continuous) is far from a unanimous resolution [70, 33]. Additionally, the behavior of wet granular materials [19, 50, 9] as well as liquid cluster formation and coalescence during capillary condensation [108, 42, 88] interests many in the physics and mechanics communities. There are however limited studies of wet granular systems for a wide range of saturation due to intricacies involved in liquid texturing as a consequence of disorder introduced via confinement. Additionally, (temperature dependent) evolution of capillary pressure field in the pore domain due to the liquid-gas interface while accounting for confinement is yet to be fully explored.

The continuum approach to the mechanics of heterogeneous continua are primarily built on Eshelby's [48] inclusion problem and mean-field based homogenization methods [119, 134]. These continuum micromechanics approaches often account for spatial distributions of the solid constituents only through their one-point correlation functions, i.e. volume fractions, while reducing their mechanical interactions to effective textures (see for e.g. [93, 10, 60, 74, 26, 61]). In addition, perturbation based solutions in statistical continuum mechanics are limited to small fluctuations in mechanical properties [11] and thus unable to capture heavy-tailed distributions characteristics of highly heterogeneous media. For highly heterogeneous materials with the length scale of observation often on par with that of the inclusions, defining a representative elementary volume (REV) that satisfies

scale separability - a requirement for any continuum approach - becomes an impractical task. Thus, these continuum micromechanics approaches have a very limited capacity to deal with highly heterogeneous solids. By extension, the micromechanics approach to poromechanics known as microporomechanics [45, 44] suffers from the same limitations.

## 1.2 Research Objectives & Approach

The objective of this thesis is to develop theoretical modeling and computational tools to explore the saturated and unsaturated poromechanics of highly heterogeneous porous solids. This work is motivated partly by the limitations of the continuum approach to the mechanics and poromechanics of heterogeneous porous solids and partly by the limited insights into the behavior of confined heterogeneous fluids. Resolving such interactions at the pore scale and translating that into mechanical or chemical work would be critical for accurate poromechanics modeling.

From materials perspective, solids in general can be organized into 1. a continuum such as a rock formation and 2. discrete particles such as sand grains. From a modeling perspective however, both these materials can be modeled in a continuum and/or a discrete fashion depending on boundary conditions, relevant time and length scales associated with the underlying mechanisms being modeled and the application under consideration. Primarily focused on (highly heterogeneous) solid continua, this thesis adapts a discrete description for solids. This enables us to go beyond limited continuum micromechanics approaches for capturing spatial variations of mechanical properties as a consequence of mesoscale texture effects (see for e.g. [84, 85, 64, 92]). While continuum based Finite Element Method (FEM) has proved to be a powerful tool for probing the mechanical behavior of materials, its direct application for highly heterogeneous systems require very fine meshing schemes leading to high computational costs. At the same time, discrete fluid and solid descriptions can benefit from statistical mechanics ensembles which provide rigorous tools to study equilibrium properties of macroscopic bodies based on relatively few thermodynamic coordinates [68]. It is in this vein that we set to reformulate poroelasticity of highly heterogeneous porous

solids by defining Biot poroelastic coefficients in statistical mechanics ensembles and for the fully saturated case. For the unsaturated case, we utilize a statistical mechanics approach to describe a heterogeneous fluid in grand canonical ensemble in a porous medium. This paves the way to study mechanics of unsaturated heterogeneous porous solids while exploring the physics behind capillary condensation, fluid criticality and liquid texturing due to disordered confinement in three-dimensions (3D).

Any theoretical modeling development along with its implementation in this thesis is followed by a validation exercise. This is to ensure that a model and its implementation reproduce consistent behaviors known for example from mean-field theories of continuum micromechanics, analytical solutions of continuum mechanics and/or lab-measured experimental data. Additionally, the computational frameworks for both fluids and solids are fully parallelized with distributed memory utilizing Message Passing Interface (MPI). This allows us to probe large number of structures and the relevant variables.

### **1.3 Thesis Outline**

Following this introduction, Chapter 2 provides the framework for discrete solid(s) description utilizing a Lattice-based discretization of materials - generally called Lattice Element Method (LEM). At its core, LEM can be described as a discrete number of points that interact with a fixed number of neighboring mass points through effective interaction potentials. Formulated within the framework of empirical force fields, harmonic-type interaction potentials are employed. Closed-form solutions to calibrate the elastic energy content of a finite sized simulation box in terms of the interaction potentials are outlined for two cases of isotropic and transversely isotropic elastic symmetries. The theoretical model including the calibration procedure and its implementation are validated considering both homogeneous and heterogeneous systems. This chapter is mostly adapted from [78, 91].

Chapter 3 is dedicated to development of a generalized framework for mesoscale poroelasticity of highly heterogeneous porous solids. In this vein, discrete expressions for

simulating Biot poroelastic coefficients [16, 106] within well-defined statistical mechanics ensembles are presented. To validate the developed model against existing continuum based analytical solutions for a fully-saturated homogeneous porous solid, we introduce an effective pore pressure force field potential that utilizes the fabric tensor characterizing the morphology of the pore space for imposing a fluid pore pressure. Finally, validation results for Biot poroelastic coefficients for both isotropic and transversely isotropic elastic symmetry cases are presented. This chapter is mostly adapted from [91].

Chapter 4 applies the developments of Chapter 2 and Chapter 3 to real porous heterogeneous materials. This is done by importing 3D computed tomography scans of highly heterogeneous organic shales LEM thus directly accounting for mesoscale textural contribution of different phases to the effective elastic and poroelastic response of these materials. A methodology is presented to calibrate the effective interaction potential of the solids from experimentally measured nanoindentation data on the same materials by accounting for spatial variations of solid interaction potentials. After this calibration and validation exercise, Biot poroelastic coefficients of these highly heterogeneous porous solids are simulated and stress transmission through them are examined. This chapter closely follows [90].

Lastly, Chapter 5 is dedicated to exploring the behavior of binary fluids in confinement and as a function of temperature. This is achieved through a discrete description of fluids by implementation of the coarse-grained lattice gas density functional theory [70, 71]. In the continuum limit, Zhou et al. [137] have shown that the lattice gas model approaches Cahn-Hilliard model. This paves the way to employ the Kortweg capillary stress tensor [72]. These theoretical models are then applied to a set of disordered granular packings. The capillary stress tensorial field is simulated in these packings, exhibiting different spatial disorder and for various temperatures. The formation and coalescence of liquid clusters are examined and a local pore pressure force formulation is proposed to account for the mechanical work due to capillary pressure scalar field that leads to solid(s) deformation. A simple example is presented to examine the induced solid stresses in response to an averaged capillary pressure field against the pressure field itself.

**THIS PAGE INTENTIONALLY LEFT BLANK**

## Chapter 2

# Discrete Solid Description: Effective Potentials & Elastic Properties in Lattice Element Method

The mechanics community has enjoyed discrete description of solids for decades (see for e.g. [62]). Generally, such discrete representation of solids involves a finite number of mass points forming a regular or irregular lattice that interact through a fixed number of neighboring mass points (see for e.g. in two dimensions (2D) [55, 124] and three dimensions (3D) [94, 73, 3]) through a network of bonds (or links). In its classical formulation, the interaction forces were derived based on a mechanics analogy with truss (or spring) systems leading to central-force lattices. This however was problematic since central-force based description of solids restricts the range of isotropic elastic behavior to materials with a Poisson's ratio,  $\nu = 1/3$  in 2D and  $\nu = 1/4$  in 3D. This is also consistent with the relationship between crystal symmetries and deformation behavior of materials [54]. Different approaches have been proposed over the years to address this limitation including accounting for beam-type interactions between mass points [109, 110, 20] with or without rotational degrees of freedom [135] and up to 178 interactions for each node in the (random lattice) system [83, 82]. However, there are no consistent frameworks for linking nodal interaction potentials to the effective behavior of the lattice. To this end, Laubie et al. [78] reformulated Lattice Element Method [124, 3] utilizing effective interaction potentials

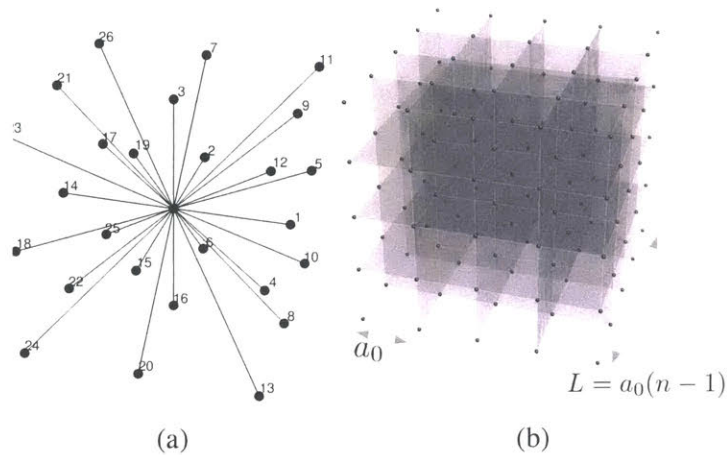


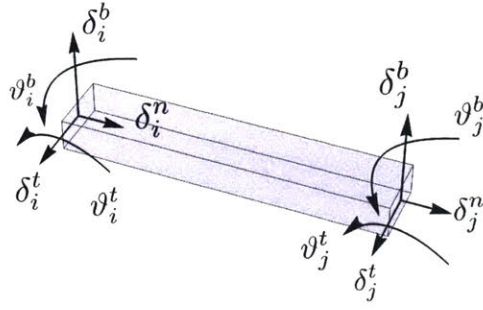
Figure 2-1: 2-1a: D3Q26 network for a unit cell; 2-1b: simple cubic lattice for material discretization.

and established a framework that allows calibration of elastic energy content of a finite-sized simulation box. While focused on the elastic behavior, a reversible phenomena, this method can be extended to poroelasticity [91] and irreversible phenomena related to plastic deformation, fracture [79] and so on (see for e.g. [55, 109, 110, 20, 124, 135, 73, 90]). The focus of this chapter is to review the elements of LEM using the conceptual framework of empirical force field as developed in [78].

## 2.1 Lattice Element Method

### 2.1.1 Lattice & Network

Spatial discretization of materials forms the core of any discrete description for solids and their mechanical behavior. In Lattice Element Method (LEM), this is done through a number of mass points that form a regular or irregular lattice. Additionally, the interactions between mass points are captured via a network of bonds that provide a mechanism for information flow in space. The formulation presented herein employs a simple cubic lattice. This is partly due to the convenience of a simple cubic lattice for representing voxels captured through advanced imaging techniques such as computed tomography scans of highly heterogeneous media (see Chapter. 4). A typical network of bonds for simple cubic lattices in 3D are  $D3Qn$  networks where  $n$  stands for the number of bonds (links). D3Q18(26) lattice networks are



(a)

Figure 2-2: Translational and rotational degrees of freedom associated with a bond element between nodes  $i$  and  $j$  in the local coordinate system.

frequently employed in lattice-Boltzmann method for fluid transport simulations (see for e.g. [118]). A D3Q18(D3Q26) lattice network implies that each mass point interacts with 18(26) neighboring mass points while propagating information in 9(13) directions. For a cubic unit cell (voxel) of size  $a_0$  centered on node 0, a D3Q18 lattice network has 6 bonds of rest-length  $l^0 = a_0$  and 12 bonds of rest-length  $l^0 = \sqrt{2}a_0$  while D3Q26 contains an additional 8 bonds of rest-length  $l^0 = \sqrt{3}a_0$  (see Fig. 2-1a). For a simple cubic lattice (see Fig. 2-1b), there are  $n_x, n_y$  and  $n_z$  mass-points in x, y and z directions. For such regular lattice, the number of bonds,  $N_{ij}$ , of lengths  $a_0$ ,  $\sqrt{2}a_0$  and  $\sqrt{3}a_0$  are summarized in Table 2.1.

## 2.1.2 Interaction Potentials

While a lattice provides the means for material discretization, the lattice network enables flow of information between discrete sites (mass points). For solid mechanics applications, one needs to define the interaction energies between various mass points. In LEM, this is achieved for mass point  $i$  and  $j$  by effective potential  $U_{ij}$  as a function of translational  $\vec{\delta}_i = \vec{x}_i - \vec{X}_i$  and rotational  $\vec{\vartheta}_i$  degrees of freedom.  $\vec{X}_i$  and  $\vec{x}_i$  denote the position vectors of mass point  $i$  in the reference and the deformed configurations, respectively. The interaction forces,  $\vec{F}$ , and moments,  $\vec{M}$ , conjugates to translational and rotational degrees of freedom

between mass points  $i$  and  $j$  derive from effective potential  $U_{ij}$ :

$$\vec{F}_i^j = -\frac{\partial U_{ij}}{\partial \vec{\delta}_i}; \quad \vec{F}_j^i = -\frac{\partial U_{ij}}{\partial \vec{\delta}_j}; \quad \vec{F}_i^j + \vec{F}_j^i = \vec{0} \quad (2.1)$$

$$\vec{M}_i^j = -\frac{\partial U_{ij}}{\partial \vec{\vartheta}_i}; \quad \vec{M}_j^i = -\frac{\partial U_{ij}}{\partial \vec{\vartheta}_j}; \quad \vec{M}_i^j + \vec{M}_j^i + \vec{r}_{ij} \times \vec{F}_j^i = \vec{0} \quad (2.2)$$

$\vec{r}_{ij} = l_{ij}^0 \vec{e}_n^{ij}$  is the vector connecting node  $i$  to node  $j$  of rest-length  $l_{ij}^0$  and oriented by the unit vector  $\vec{e}_n^{ij}$  in a local orthonormal basis  $(\vec{e}_n, \vec{e}_b, \vec{e}_t)$  (see Fig. 2-2). Through attributing the same mass to all points, mass is automatically conserved while both forces and moments between two mass points satisfy equilibrium. Rotations are considered to be small ( $\|\vec{\vartheta}_i\| \ll 1$ ) thus standard vector rotation rules apply. The deformation arguments for effective potential  $U_{ij}$  while satisfying Newton constraints Eq. (2.1) are:

$$U_{ij} = U_{ij}(\vec{\delta}_j - \vec{\delta}_i + \vec{r}_{ij} \times \vec{\vartheta}_i; \vec{\vartheta}_j - \vec{\vartheta}_i) \quad (2.3)$$

Eq. (2.3) considers energies associated with both two-body and three-body interactions which can be separated as:

$$U_{ij} = U_{ij}^s + U_{ij}^b \quad (2.4)$$

where  $U_{ij}^s = U_{ij}^s((\vec{x}_j - \vec{x}_i) \cdot \vec{e}_n = \delta_j^n - \delta_i^n)$  stands for any suitable pairwise potential representative of the solid. A linear elastic solids implies a harmonic pairwise potential:

$$U_{ij}^s = \frac{1}{2} \epsilon_{ij}^n \left( \frac{\delta_j^n - \delta_i^n}{l_{ij}^0} \right)^2 \quad (2.5)$$

With  $\epsilon_{ij}^n$  denoting the axial energy parameter . Additionally, the three-body interactions,  $U_{ij}^b = U_{ij}^b \left( (\vec{x}_j - \vec{x}_i) \cdot \vec{e}_b; (\vec{x}_j - \vec{x}_i) \cdot \vec{e}_i; \vartheta_j - \vartheta_i \right)$  for the harmonic case reads [78]:

$$\begin{aligned}
U_{ij}^b &= \frac{1}{2} \epsilon_{ij}^t \left\{ \left( \frac{\delta_j^b - \delta_i^b}{l_{ij}^0} - \vartheta_i^t \right)^2 + \left( \frac{\delta_j^t - \delta_i^t}{l_{ij}^0} + \vartheta_i^b \right)^2 \right. \\
&\quad + \left( \frac{\delta_j^b - \delta_i^b}{l_{ij}^0} - \vartheta_i^t \right) (\vartheta_i^t - \vartheta_j^t) + \left( \frac{\delta_j^t - \delta_i^t}{l_{ij}^0} + \vartheta_i^b \right) (\vartheta_j^b - \vartheta_i^b) \\
&\quad \left. + \frac{1}{3} \left( (\vartheta_j^b - \vartheta_i^b)^2 + (\vartheta_i^t - \vartheta_j^t)^2 \right) \right\} \quad (2.6)
\end{aligned}$$

where  $\epsilon_{ij}^t$  is the transverse energy parameter. Energy parameters  $\epsilon_{ij}^{n,t} \geq 0$  govern the elastic two- and three-body interactions and must be positive to ensure convexity of energy function. It should be noted that the defined harmonic potentials are merely Taylor expansions of non-harmonic potentials around the equilibrium state of a system in LEM [78]. Thus, non-harmonic potentials can be considered without much loss of generality. Having defined  $U_{ij}$  (see Eqs. (2.5) and (2.6)), the forces and moments can be readily obtained:

$$\begin{aligned}
\vec{F}_i^j &= -\frac{\partial U_{ij}}{\partial \vec{\delta}_i} = \underbrace{\frac{\epsilon_{ij}^n}{l_{ij}^0} \left( \frac{\delta_j^n - \delta_i^n}{l_{ij}^0} \right)}_{F_i^{j,n}} \vec{e}_n + \underbrace{\frac{\epsilon_{ij}^t}{l_{ij}^0} \left( \frac{\delta_j^b - \delta_i^b}{l_{ij}^0} - \frac{1}{2} (\vartheta_j^t + \vartheta_i^t) \right)}_{F_i^{j,b}} \vec{e}_b \\
&\quad + \underbrace{\frac{\epsilon_{ij}^t}{l_{ij}^0} \left( \frac{\delta_j^t - \delta_i^t}{l_{ij}^0} + \frac{1}{2} (\vartheta_j^b + \vartheta_i^b) \right)}_{F_i^{j,t}} \vec{e}_t \\
\vec{M}_i^j &= -\frac{\partial U_{ij}}{\partial \vec{\vartheta}_i} = \underbrace{-\frac{\epsilon_{ij}^t}{2} \left( \frac{\delta_j^t - \delta_i^t}{l_{ij}^0} + \frac{1}{3} (\vartheta_j^b + 2\vartheta_i^b) \right)}_{M_i^{j,b}} \vec{e}_b \\
&\quad + \underbrace{\frac{\epsilon_{ij}^t}{2} \left( \frac{\delta_j^b - \delta_i^b}{l_{ij}^0} - \frac{1}{3} (\vartheta_j^t + 2\vartheta_i^t) \right)}_{M_i^{j,t}} \vec{e}_t
\end{aligned}$$

The nodal stress is defined by the virial expression [30]. Neglecting the momentum terms, it can be expressed as:

$$\boldsymbol{\sigma}_i = \frac{1}{2V_i} \sum_{j=1}^{N_i^b} \vec{r}_{ij} \otimes \vec{F}_i^j \quad (2.7)$$

with  $V_i = a_0^3$  the volume of a unit cell and  $N_i^b$  the number of neighboring mass points for node  $i$ . It is worth noting that while the bending moments are not directly used to calculate the virial stress, the equilibrium of moments ensures the symmetry of the stress tensor at node  $i$ . Recall from Eq. (2.2) [78]:

$$\vec{0} = \sum_{j=1}^{N_i^b} \vec{r}_{ij} \times \vec{F}_i^j = \sum_{j=1}^{N_i^b} \sum_{k=1}^3 \left\{ (\vec{r}_{ij} \times \vec{F}_i^j \cdot \vec{e}_k) \right\} \cdot \vec{e}_k \quad (2.8)$$

with  $(\vec{e}_k, \vec{e}'_k, \vec{e}''_k)$  denoting a right-handed orthonormal basis. Utilizing the identity:

$$(\vec{a} \times \vec{b}) \cdot \vec{e}_k = \vec{e}'_k \cdot (\vec{a} \otimes \vec{b} - \vec{b} \otimes \vec{a}) \cdot \vec{e}''_k \quad (2.9)$$

the equilibrium of moments can be established as follows:

$$\vec{0} = \sum_{j=1}^{N_i^b} \sum_{k=1}^3 \left\{ \vec{e}'_k \cdot (\vec{r}_{ij} \otimes \vec{F}_i^j - \vec{F}_i^j \otimes \vec{r}_{ij}) \cdot \vec{e}''_k \right\} \vec{e}_k \quad (2.10)$$

$$= \sum_{k=1}^3 \left( \vec{e}'_k \cdot \left\{ \sum_{j=1}^{N_i^b} (\vec{r}_{ij} \otimes \vec{F}_i^j - \vec{F}_i^j \otimes \vec{r}_{ij}) \right\} \cdot \vec{e}''_k \right) \vec{e}_k \quad (2.11)$$

$$= \sum_{k=1}^3 V_i \left( \vec{e}'_k \cdot \left\{ \boldsymbol{\sigma}_i - {}^T \boldsymbol{\sigma}_i \right\} \cdot \vec{e}''_k \right) \vec{e}_k \quad (2.12)$$

Eq. (2.12) ensures the symmetry of stress tensor, i.e.  $\boldsymbol{\sigma}_i = {}^T \boldsymbol{\sigma}_i$ , if the equilibrium of moments are satisfied. This underlines the importance of rotational degrees of freedom,  $\vec{\vartheta}_j$ , and the associated energy parameter  $\epsilon_{ij}^t \neq 0$  for ensuring symmetry of the stress tensor. In addition, rotational degrees of freedom and  $\epsilon_{ij}^t \neq 0$  enable capturing a wide range of elastic behavior in LEM which will be discussed next.

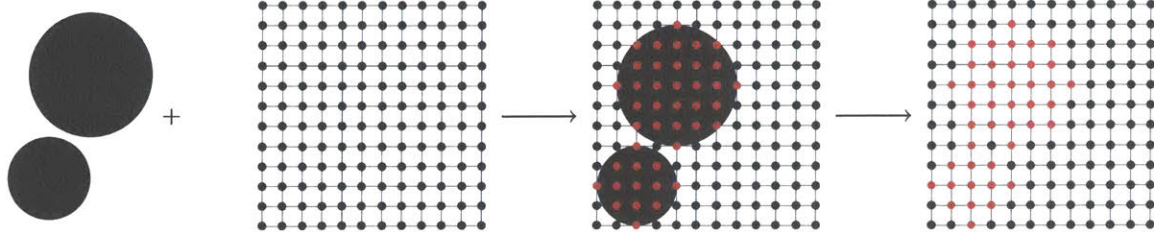


Figure 2-3: Superposition of lattice and material representation. After discretization of the material domain, calibrated energy parameters are assigned to solid phase(s).

## 2.2 Effective Elastic Properties

### 2.2.1 From Microscopic Link Properties to Macroscopic Effective Behavior

The (effective) elastic behavior of the assembly of mass-points and bonds can be readily obtained having defined the core ingredients of LEM, i.e. interaction potentials at the scale of the unit cell for a given lattice network. The elastic energy content of this assembly,  $U_{tot}$ ,

Table 2.1: Link index, length, number and energy parameters for isotropic and transversely isotropic elastic symmetries for the D3Q26 lattice and D3Q18 (first 9 lines) lattice.

Links $i - j$	Length $l_{ij}^0$	Number $N_{ij}$	Isotropy	Transverse Isotropy
0-1/0-14	$a_0$	$(n_x - 1) n_y n_z$	$\epsilon_1^{n,t}$	$\epsilon_1^{n,t}$
0-2/0-15	$a_0$	$n_x (n_y - 1) n_z$	$\epsilon_1^{n,t}$	$\epsilon_1^{n,t}$
0-3/0-16	$a_0$	$n_x n_y (n_z - 1)$	$\epsilon_1^{n,t}$	$\epsilon_3^n, \epsilon_1^t$
0-4/0-17	$\sqrt{2}a_0$	$(n_x - 1) (n_y - 1) n_z$	$\epsilon_4^{n,t}$	$\epsilon_4^{n,t}$
0-5/0-18	$\sqrt{2}a_0$	$(n_x - 1) (n_y - 1) n_z$	$\epsilon_4^{n,t}$	$\epsilon_4^{n,t}$
0-6/0-19	$\sqrt{2}a_0$	$n_x (n_y - 1) (n_z - 1)$	$\epsilon_4^{n,t}$	$\epsilon_6^n, \epsilon_4^t$
0-7/0-20	$\sqrt{2}a_0$	$n_x (n_y - 1) (n_z - 1)$	$\epsilon_4^{n,t}$	$\epsilon_6^n, \epsilon_4^t$
0-8/0-21	$\sqrt{2}a_0$	$(n_x - 1) n_y (n_z - 1)$	$\epsilon_4^{n,t}$	$\epsilon_6^n, \epsilon_4^t$
0-9/0-22	$\sqrt{2}a_0$	$(n_x - 1) n_y (n_z - 1)$	$\epsilon_4^{n,t}$	$\epsilon_6^n, \epsilon_4^t$
0-10/0-23	$\sqrt{3}a_0$	$(n_x - 1) (n_y - 1) (n_z - 1)$	$\epsilon_{10}^{n,t}$	$\epsilon_{10}^{n,t}$
0-11/0-24	$\sqrt{3}a_0$	$(n_x - 1) (n_y - 1) (n_z - 1)$	$\epsilon_{10}^{n,t}$	$\epsilon_{10}^{n,t}$
0-12/0-25	$\sqrt{3}a_0$	$(n_x - 1) (n_y - 1) (n_z - 1)$	$\epsilon_{10}^{n,t}$	$\epsilon_{10}^{n,t}$
0-13/0-26	$\sqrt{3}a_0$	$(n_x - 1) (n_y - 1) (n_z - 1)$	$\epsilon_{10}^{n,t}$	$\epsilon_{10}^{n,t}$

is simply the sum of energy of all bonds:

$$U_{tot} = \sum_{ij} U_{ij} \left( \vec{\delta}_j - \vec{\delta}_i + \vec{r}_{ij} \times \vec{\vartheta}_i; \vec{\vartheta}_j - \vec{\vartheta}_i \right) \quad (2.13)$$

To access the fourth-order elastic stiffness tensor,  $C_{ijkl}$ , around the equilibrium state one needs to prescribe small deformation fields. As stated before, considering a simple cubic lattice with  $n = n_x = n_y = n_z$  mass point in each direction and a lattice size of  $a_0$ , Eq. (2.13) can be re-written as:

$$U_{tot} = \sum_{i=1}^{9(13)} N_{0i} U_{0i} \left( \vec{\delta}_i - \vec{\delta}_0 + \vec{r}_{0i} \times \vec{\vartheta}_i \right) \quad (2.14)$$

with summations over 9(13) bond directions of the D3Q18(26) lattice and  $N_{0i}$  expressed in Table 2.1. Thus, all it takes to evaluate Eq. (2.14) is to express the arguments of energy  $U_{0i}$  in terms of strains and rotations:

$$\left( \delta_i^{n,b,t} - \delta_0^{n,b,t} \right) = l_{0i}^0 \Delta_{ji}^{n,b,t} \varepsilon_j \quad (2.15)$$

$$\vartheta_i^{b,t} = P_{ji}^{b,t} \theta_j \quad (2.16)$$

where Einstein's summation rule is employed. Additionally,  $\varepsilon_j$  represents strain components  $\{\varepsilon\} = (\varepsilon_{xx}, \varepsilon_{yy}, \varepsilon_{zz}, \varepsilon_{yz}, \varepsilon_{xz}, \varepsilon_{xy})$  and  $\theta = (\vartheta_x, \vartheta_y, \vartheta_z)$  the rotational degrees of freedom in the global coordinate system  $(\vec{e}_x, \vec{e}_y, \vec{e}_z)$ . The  $\Delta^{n,b,t}$  and  $\mathbf{P}^{b,t}$  are transformation matrices relating the global and local coordinate systems (see Appendix A and Appendix B). Having  $U_{tot} = U_{tot}(\{\varepsilon\}, \{\theta\})$  at hand, the elastic stiffness of the lattice can be derived:

$$C_{ijkl} = \frac{1}{V} \frac{\partial^2 \bar{U}_{tot}}{\partial \varepsilon_{ij} \partial \varepsilon_{kl}} \quad (2.17)$$

where volume  $V = (nx - 1)(ny - 1)(nz - 1)a_0^3$  and  $\bar{U}_{tot}(\{\varepsilon\}) = \min_{\{\theta\}} U_{tot}(\{\varepsilon\}, \{\theta\})$  is obtained through the theory of minimum potential energy.

## 2.2.2 Cubic & Isotropic Elastic Symmetries

First, the case of isotropic elastic symmetry is considered. For a material exhibiting an isotropic elastic behavior, only two elastic constants are needed to fully characterize its behavior - for example  $C_{1111} = C_{11}$  and  $C_{1122} = C_{12}$  (in Voigt notations) would be sufficient. For this case, the non-zero stiffness constants are  $C_{11} = C_{22} = C_{33}$ ,  $C_{12} = C_{13} = C_{23}$  and  $C_{44} = C_{55} = C_{66} = (C_{11} - C_{12}) / 2$ . Due to directionally independent behavior of isotropic materials, for D3Q18(26) lattices the effective isotropic behavior requires 4(6) energy parameters  $\epsilon_{1,4,(10)}^{n,t}$ . The elastic stiffness constants can be written in a linear form of the energy parameters:

$$C_i = A_{ij}^{Iso} \epsilon_j \quad (2.18)$$

where  $\{C\} = (C_{11}, C_{13}, C_{55})$  and  $\{\epsilon\} = (\epsilon_1^n, \epsilon_4^n, \epsilon_{10}^n, \epsilon_1^t, \epsilon_4^t, \epsilon_{10}^t)$ . The linear operator  $A^{Iso}$  relates energy parameters  $\{\epsilon\}$  to elastic stiffness constants  $\{C\}$  for a finite-sized simulation box of size  $n$ , in 3D:

$$A^{Iso,3D} = \frac{1}{a_0^3} \begin{bmatrix} \frac{n^2}{(n-1)^2} & \frac{n}{(n-1)} & \frac{4}{9} & 0 & \frac{n}{n-1} & \frac{8}{9} \\ 0 & \frac{n}{2(n-1)} & \frac{4}{9} & 0 & -\frac{n}{2(n-1)} & -\frac{4}{9} \\ 0 & \frac{n}{2(n-1)} & \frac{4}{9} & \frac{n^2}{2(n-1)^2} & \frac{n}{2(n-1)} & \frac{2}{9} \end{bmatrix} \quad (2.19)$$

and in quasi-2D ( $n_x = n_z = n, n_y = 2$ ):

$$A^{Iso,2D} = \frac{1}{a_0^3} \begin{bmatrix} \frac{2n}{n-1} & \frac{3n-2}{2(n-1)} & \frac{4}{9} & 0 & \frac{3n-2}{2(n-1)} & \frac{8}{9} \\ 0 & 1 & \frac{4}{9} & 0 & -1 & -\frac{4}{9} \\ 0 & 1 & \frac{4}{9} & \frac{n}{n-1} & \frac{n}{2(n-1)} & \frac{2}{9} \end{bmatrix} \quad (2.20)$$

For  $\epsilon_i^t = 0$  in Eq. (2.18), one can recover the well-known Cauchy condition [122], i.e.  $C_{13} = C_{55}$ . Furthermore, the simple cubic lattice naturally leads to a cubic elastic symmetry. A cubic elastic symmetry is characterized by 3 independent elastic constants. In order to obtain isotropic symmetry, characterized by two independent elastic constants, an additional

constraint needs to be satisfied:

$$G = C_{55} = \frac{C_{11} - C_{13}}{2} = \frac{E}{2(1 + \nu)} \quad (2.21)$$

with  $G$ ,  $E$  and  $\nu$  denoting the shear modulus, the Young's modulus and Poisson's ratio, respectively. In terms of  $C_{ijkl}$ , these moduli can be expressed as, in 3D:

$$E^{3D} = C_{11} - \frac{2C_{13}^2}{C_{11} + C_{13}} \quad (2.22)$$

$$\nu^{3D} = \frac{C_{13}}{C_{11} + C_{13}} \quad (2.23)$$

and in 2D:

$$E^{2D} = C_{11} \left( 1 - \frac{C_{13}^2}{C_{11}^2} \right) \quad (2.24)$$

$$\nu^{2D} = \frac{C_{13}}{C_{11}} \quad (2.25)$$

For a central-force lattice model, i.e.  $\epsilon_i^t = 0$ , the Cauchy condition  $C_{13} = C_{55} = G$  combined with Eq. (2.21) results in  $C_{11} = 3G$ . Thus, from Eq. (2.23) in 3D and Eq. (2.25) in 2D, one can immediately recognize the well-known limitation on central-force lattices, i.e.  $\nu^{3D} = 1/4$  and  $\nu^{2D} = 1/3$ . Thus, rotational degrees of freedom associated with energy parameter  $\epsilon_i^t$  not only plays a critical role in ensuring symmetry of stress tensor as discussed before (see Eq. (2.12)) but it enables the model to capture a wider range of elastic behavior. In the isotropic case and provided  $\epsilon_i^{n,t} \geq 0$  one can capture the following range of Poisson's ratios:

$$-1 < \nu^{3D} \leq 1/4 \quad (2.26)$$

$$-2/3 \leq \nu^{2D} \leq 1/3 \quad (2.27)$$

For  $\epsilon_i^{n,t} < 0$  and with the formulation presented thus far, values outside of this range can be achieved. However, negative energy parameters may lead to instabilities in energy minimization for seeking the equilibrium state. To extend this range, other options include reformulating LEM with a different combination of lattice (regular or irregular) and net-

work [95] and/or considering non-local energy interactions [114]. Inverse application of Eq. (2.18) while respecting the constraint defined in Eq. (2.21), allows calibration of energy parameters  $\epsilon_i^{n,l} \geq 0$  to reproduce a desired isotropic elastic behavior limited by Eq. (2.26) in 3D and Eq. (2.27) in 2D. To this end, a minimum of three non-zero energy parameters  $\epsilon_i^{n,l} \geq 0$  and eighteen bonds are required to model an isotropic elastic behavior using harmonic potentials. Diagonal bonds play a critical role in reproducing Poisson's contraction. Given the finite size of a simulation box  $n$ , Table 2.2 provides expressions to relate energy parameters to the Young's modulus,  $E$ , and the Poisson's ratio,  $\nu$ .

### 2.2.3 Transversely Isotropic Elastic Symmetry

The case of transversely isotropic elastic symmetry - with rotational symmetry around  $\vec{e}_3 = \vec{e}_z$  normal to plane of isotropy - can be also modeled in LEM. In this case, the non-zero elastic stiffness constants are:  $C_{11} = C_{22}$ ,  $C_{13} = C_{23}$ ,  $C_{33}$  and  $C_{44} = C_{55}$ . Similar to the isotropic case, the linear relationship between energy parameters  $\{\epsilon\} = (\epsilon_1^n, \epsilon_3^n, \epsilon_4^n, \epsilon_6^n, \epsilon_{10}^n, \epsilon_1^l, \epsilon_4^l, \epsilon_{10}^l)$  and stiffness constants  $\{C\} = (C_{11}, (C_{12}), C_{13}, C_{33}, C_{55}, (C_{66}))$  in 2D(3D) can be expressed as:

$$C_i = A_{ij}^{TI} \epsilon_j \quad (2.28)$$

with the linear operator  $A_{ij}^{TI}$  defined in 3D:

$$A^{TI,3D} = \frac{1}{a_0^3} \begin{bmatrix} \frac{n^2}{(n-1)^2} & 0 & \frac{n}{2(n-1)} & \frac{n}{2(n-1)} & \frac{4}{9} & 0 & \frac{n}{n-1} & \frac{8}{9} \\ 0 & 0 & \frac{n}{2(n-1)} & 0 & \frac{4}{9} & 0 & -\frac{n}{2(n-1)} & -\frac{4}{9} \\ 0 & 0 & 0 & \frac{n}{2(n-1)} & \frac{4}{9} & 0 & -\frac{n}{2(n-1)} & -\frac{4}{9} \\ 0 & \frac{n^2}{(n-1)^2} & 0 & \frac{n}{n-1} & \frac{4}{9} & 0 & \frac{n}{n-1} & \frac{8}{9} \\ 0 & 0 & 0 & \frac{n}{2(n-1)} & \frac{4}{9} & \frac{n^2}{2(n-1)^2} & \frac{n}{2(n-1)} & \frac{2}{9} \\ 0 & 0 & 0 & 1 & \frac{4}{9} & \frac{n}{n-1} & \frac{n}{2(n-1)} & \frac{2}{9} \end{bmatrix} \quad (2.29)$$

and in 2D:

$$A^{TI,2D} = \frac{1}{a_0^3} \begin{bmatrix} \frac{2n}{n-1} & 0 & \frac{n}{2(n-1)} & 1 & \frac{4}{9} & 0 & \frac{3n-2}{2n-2} & \frac{8}{9} \\ 0 & 0 & 0 & 1 & \frac{4}{9} & 0 & -1 & -\frac{4}{9} \\ 0 & \frac{2n}{n-1} & 0 & \frac{3n-2}{2(n-1)} & \frac{4}{9} & 0 & \frac{3n-2}{2(n-1)} & \frac{8}{9} \\ 0 & 0 & 0 & 1 & \frac{4}{9} & \frac{n}{n-1} & \frac{n}{2(n-1)} & \frac{2}{9} \end{bmatrix} \quad (2.30)$$

Additionally, the energy parameters  $\epsilon_i^{n,t} \geq 0$  need to satisfy  $C_{66} = (C_{11} - C_{12})/2$  for the transversely isotropic case. Similar to the limitations in capturing the full range of Poisson's ratio in the isotropic case, the following restrictions apply for the transversely isotropic case:

$$C_{12} \leq C_{66} \left( \text{i.e., } C_{12} \leq \frac{1}{3}C_{11} \right); C_{13} \leq C_{44} \quad (2.31)$$

Finally, similar to the isotropic case, the inverse application of Eq. (2.28) while respecting  $C_{66} = (C_{11} - C_{12})/2$  and constraints outlined in Eq. (2.31) paves the path for calibration of the harmonic interaction potential parameters for a given set of (effective) transversely isotropic elastic behavior.

Table 2.2: Expressions for calibrations of the elastic energy content of the finite sized simulation box in terms of energy parameters.

Energy parameters	$-1 \leq \nu^{3D} \leq 0$	$0 \leq \nu^{3D} \leq 1/4$	$-2/3 \leq \nu^{2D} \leq 0$	$0 \leq \nu^{2D} \leq 1/3$
$\epsilon_1^n$	$\frac{(n-1)^2 Ea_0^3}{n^2(1-2\nu)}$	$\frac{(n-1)^2(1-3\nu)Ea_0^3}{n^2(1+\nu)(1-2\nu)}$	$\frac{Ea_0^3(n(2+3\nu)-2(1+\nu))}{4n(1-\nu^2)}$	$\frac{Ea_0^3(n(2-3\nu)-2(1-\nu))}{4n(1-\nu^2)}$
$\epsilon_4^n$	0	$\frac{2\nu Ea_0^3(n-1)}{n(1+\nu)(1-2\nu)}$	0	$\frac{\nu Ea_0^3}{1-\nu^2}$
$\epsilon_{10}^n$	0	0	0	0
$\epsilon_1^t$	$\frac{(n-1)^2 Ea_0^3}{n^2(1+\nu)(1-2\nu)}$	$\frac{(n-1)^2(1-4\nu)Ea_0^3}{n^2(1+\nu)(1-2\nu)}$	$\frac{Ea_0^3(n-1+\nu)}{2n(1-\nu^2)}$	$\frac{(n-1)(1-3\nu)Ea_0^3}{2n(1-\nu^2)}$
$\epsilon_4^t$	$-\frac{2(n-1)\nu Ea_0^3}{n(1+\nu)(1-2\nu)}$	0	$\frac{-\nu Ea_0^3}{1-\nu^2}$	0
$\epsilon_{10}^t$	0	0	0	0

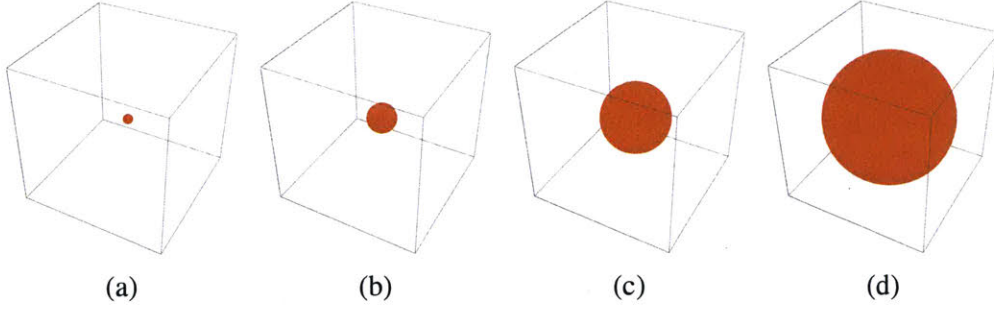


Figure 2-4: Schematics for a set of structures used for validation. Each structure contains a centric spherical pore. A range of pore radii are used to achieve different porosities.

## 2.3 Numerical Implementation

The response of a solid due to a prescribed displacement  $\vec{\xi}^d$  on boundary  $\partial\Omega_{\vec{\xi}^d}$  and/or traction  $\vec{T}^d$  on boundary  $\partial\Omega_{\vec{T}^d}$  can be resolved through the theory of minimum potential energy:

$$\bar{E}_{\text{pot}}^s(\boldsymbol{\varepsilon}, \vec{\xi}) = \min_{\vec{\xi}' \in \text{K.A.}} E_{\text{pot}}^s = \min_{\vec{\xi}' \in \text{K.A.}} \left( \Psi^s(\boldsymbol{\varepsilon}') - W(\vec{\xi}') \right) \quad (2.32)$$

with  $\boldsymbol{\varepsilon}$  denoting the strain tensor and K.A. representing the set of kinematically admissible displacement fields that satisfy displacement boundary conditions:

$$\text{K.A.} = \{ \vec{\xi} \text{ continuous such that } \vec{\xi} = \vec{\xi}^d \text{ on } \partial\Omega_{\vec{\xi}^d} \} \quad (2.33)$$

$E_{\text{pot}}^s$  and  $\Psi^s$  represent the potential energy of the solid and the Helmholtz free energy of the solid, respectively. Additionally,  $W$  is the external work due to body forces  $\vec{b}$  and prescribed traction,  $\vec{T}^d$ :

$$W(\vec{\xi}') = \int_{\Omega} \vec{\xi}' \cdot \vec{b} d\Omega + \int_{\partial\Omega_{\vec{T}^d}} \vec{\xi}' \cdot \vec{T}^d da \quad (2.34)$$

In terms of numerical implementation of Eq. (2.32), consider a cubic simulation box of length  $L = L_x = L_y = L_z$  (volume  $V = L_x L_y L_z$ ) discretized by  $n = n_x = n_y = n_z$  mass points in each direction and a lattice spacing of  $a_0 = L / (n - 1)$  resulting in  $N = n_x n_y n_z$  nodes (mass points) in total. In normalized coordinates, node  $i$  is located at  $\{\tilde{r}_i\} = (\tilde{x}, \tilde{y}, \tilde{z})$

with  $(\tilde{x}, \tilde{y}, \tilde{z}) \in \{0, 1, \dots, n_{x,y,z} - 1\}$  with tilde  $\tilde{\cdot}$  denoting quantities in code units<sup>1</sup>. A one-to-one relationship between an index for node  $i$  and its coordinates can be established:  $i = \tilde{x} + n_x \tilde{y} + n_x n_y \tilde{z}$ . Then, a 6N-vector  $\{\tilde{d}\}$  is defined to stores the 6 degrees of freedom associated with each node, i.e. displacements  $\tilde{\delta}_i$  and rotational  $\tilde{\theta}_i$  degrees of freedom. This is done as follows:  $\tilde{d}_{6i} = \tilde{\delta}_i^x$ ,  $\tilde{d}_{6i+1} = \tilde{\delta}_i^y$ ,  $\tilde{d}_{6i+2} = \tilde{\delta}_i^z$ ,  $\tilde{d}_{6i+3} = \tilde{\theta}_i^x$ ,  $\tilde{d}_{6i+4} = \tilde{\theta}_i^y$ ,  $\tilde{d}_{6i+5} = \tilde{\theta}_i^z$ . Once the energy is minimized, the forces and moments are obtained at each node  $i$  by summing the contribution of its interactions with its nearest neighbors:

$$\vec{F}_i = \sum_{j=1}^{N_i^b} \vec{F}_i^j \quad (2.35)$$

$$\vec{M}_i = \sum_{j=1}^{N_i^b} \vec{M}_i^j \quad (2.36)$$

$N_i^b$  is the number of node  $i$ 's nearest neighbors and  $\vec{F}_i^j$  and  $\vec{M}_i^j$  are given by Eq. (2.7). Forces and moments are also sorted in a 6N-vector  $\{\tilde{f}\}$  such that  $\tilde{f}_{6i} = \tilde{F}_i^x$ ,  $\tilde{f}_{6i+1} = \tilde{F}_i^y$ ,  $\tilde{f}_{6i+2} = \tilde{F}_i^z$ ,  $\tilde{f}_{6i+3} = \tilde{M}_i^x$ ,  $\tilde{f}_{6i+4} = \tilde{M}_i^y$  and  $\tilde{f}_{6i+5} = \tilde{M}_i^z$ . In order to enforce imposed displacement and/or traction boundary condition, those boundary nodes are stored in sets  $N_{\tilde{f}^d} = \left\{ (j, \tilde{f}^d) \mid \tilde{f}_j = \tilde{f}^d \right\}$  for nodes where a force is imposed and  $N_{\tilde{\delta}^d} = \left\{ (j, \tilde{\delta}^d) \mid \tilde{d}_j = \tilde{\delta}^d \right\}$  for nodes where a displacement is imposed ( $\forall j \in \{0, \dots, 6N - 1\}$ ). The potential energy in LEM can be obtained from:

$$E_{\text{pot}}^s = \frac{1}{2} \sum_{i=1}^N \sum_{j=1}^{N_j^b} \tilde{U}_{ij}(\vec{\tilde{d}}) - \sum_{(i, \tilde{f}^d) \in N_{\tilde{f}^d}} \tilde{d}_i \tilde{f}^d \quad (2.37)$$

The factor 1/2 accounts for counting the contribution of each bond twice. The first expression in Eq. (2.37) is the Helmholtz free energy of the solid while the second term represents the the work done by external forces. The numerical implementation of Eq. (2.32) in LEM reduces to minimizing  $E_{\text{pot}}^s$  with vector  $\{\tilde{d}\}$  containing the degrees of freedom while satisfying constraints  $\tilde{d}_j = \tilde{\delta}^d$  for  $(j, \tilde{\delta}^d) \in N_{\tilde{\delta}^d}$  to ensure boundary conditions are enforced. The

<sup>1</sup>The relationship between reals units and code units are as follows: For energy  $U = \tilde{U} a_0^3$ , for force  $f = \tilde{f} a_0$ , for length  $l = \tilde{l} a_0$  and for stress,  $\sigma = \tilde{\sigma}$ .

energy minimization is performed numerically, using a the Fletcher-Reeves-Polak-Ribiere non-linear conjugate gradient method. Once the equilibrium position is found, the stress tensor at each node is obtained using the virial definition:

$$\tilde{\sigma}_i = \frac{1}{2} \sum_{j=1}^{N_i^b} \tilde{r}_{ij} \otimes \tilde{F}_i^j \quad (2.38)$$

with  $\tilde{r}_{ij} = l_{ij}^0 \vec{e}_n^{ij}$ . The total stress can be obtained from:

$$\tilde{\sigma} = \frac{1}{\tilde{V}} \sum_i^N \tilde{\sigma}_i \quad (2.39)$$

with  $\tilde{V} = (n_x - 1) (n_y - 1) (n_z - 1)$  the volume of the simulation box. Since both nodal translational and rotational degrees of freedom are subjected to minimization, the force and moment equilibrium is satisfied, ensuring the symmetry of the stress tensor, i.e.  $\tilde{\sigma}_{ij} = \tilde{\sigma}_{ji}$ .

## 2.4 Validation

To validate the formulation presented so far, two approaches are considered. First, the accuracy of the calibration procedure outlined in Section 2.2 is assessed on a homogeneous system. Next, we apply LEM to a heterogeneous system comprised of a centric spherical pore embedded in a solid matrix. The computation results are then compared with existing continuum micromechanics solutions.

### 2.4.1 Continuum Micromechanics Reference Solutions

The second validation approach, i.e. application of LEM to a heterogeneous system employs a number of model structures with a centric spherical pore embedded in a solid matrix. Such microtexture is associated with the Mori-Tanaka effective estimates of continuum micromechanics [93, 10]. Focusing on the (drained) effective stiffness tensor,  $\mathbb{C}$ , linear homogenization methods - assuming scale separability - provide the following expression

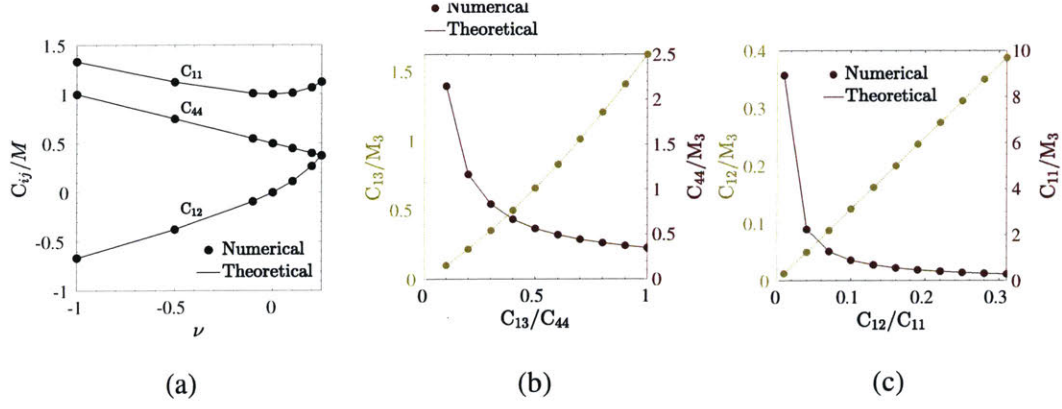


Figure 2-5: Validation of closed form calibration expressions (Theoretical) against numerical implementation from LEM (Numerical) for the isotropic case (2-5a) and transversely isotropic case (2-5b and 2-5c).

(see for e.g. [134]):

$$\mathbb{C} = (1 - \phi_0) \mathbb{C}^s : \langle \mathbb{A} \rangle_{V_s} \quad (2.40)$$

where  $\langle \mathbb{A} \rangle_{V_s}$  is the average strain localization tensor over the solid phase ( $V_s$ ). In continuum micromechanics, the strain localization tensor links the macroscopic strain  $\mathbf{E}$  imposed as a boundary condition:

$$\vec{\xi}^d(\vec{x}) = \mathbf{E} \cdot \vec{x} \quad \forall \vec{x} \in \partial\Omega_{\vec{\xi}^d} \quad (2.41)$$

to the continuous microstrains  $\boldsymbol{\varepsilon}(\vec{x}) = \mathbb{A}(\vec{x}) : \mathbf{E}$  in the solid phase. For the Mori-Tanaka effective estimates, the average strain localization tensor for the inclusion phase  $r$  embedded in matrix with bulk stiffness  $\mathbb{C}^s$ , reads:

$$\langle \mathbb{A} \rangle_r = [\mathbb{I} + \mathbb{P} : (\mathbb{C}^r - \mathbb{C}^s)]^{-1} : \langle [\mathbb{I} + \mathbb{P} : (\mathbb{C}^r - \mathbb{C}^s)^{-1}] \rangle_V^{-1} \quad (2.42)$$

where  $\mathbb{P}$ , the generalized Hill concentration tensor defined as [134]:

$$P_{ijkl} = - \left( \frac{\partial^2}{\partial x_j \partial x_l} \int_{\Omega} G_{ik}(\vec{x} - \vec{x}') d\Omega \right)_{(ij)(kl)} \quad (2.43)$$

$(ij)(kl)$  indicates symmetrization operation and  $G_{ij}(\vec{x} - \vec{x}')$  is the second order Green's tensor for generalized linear elastic anisotropic media (see Appendix C). The extension of such mean-field theory homogenization based method to poromechanics and the importance

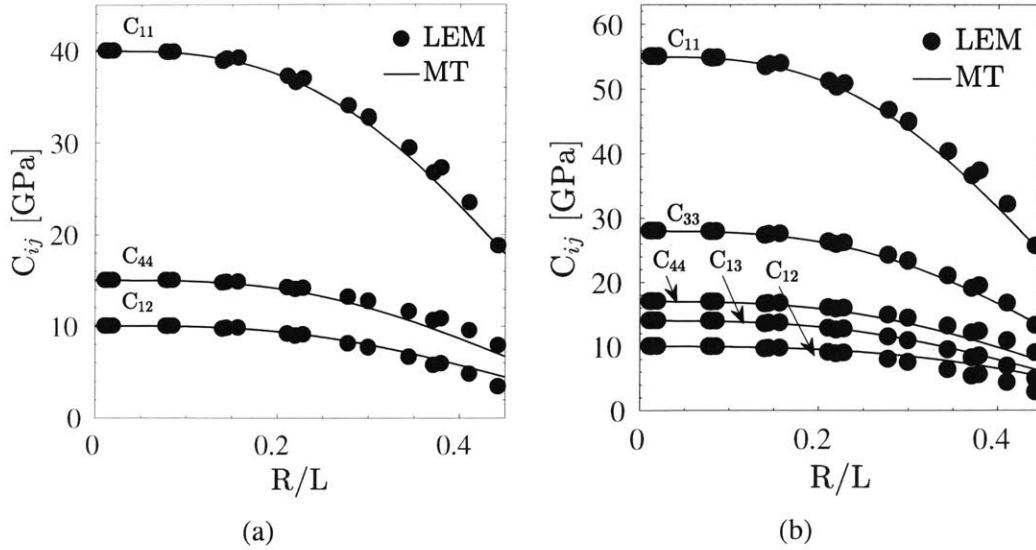


Figure 2-6:  $C_{ij}$  - in Voigt's notations - variations versus  $R/L$  for the isotropic case (2-6a) and transversely isotropic case (2-6b). "MT" refers to Mori-Tanaka continuum solution whereas "LEM" represents discrete simulations.

of scale separability will be further discussed in Chapter 3.

## 2.4.2 Validation Results

### Calibration Procedure

In order to validate the calibration procedure, the accuracy of the analytical expressions linking energy parameters to the desired (effective) elastic behavior (see Table 2.2) is assessed. To do this, the imposed elasticity is compared against the numerically obtained values as shown in Fig. 2-5 for both isotropic and transversely isotropic elastic symmetries. The simulations encompass a variety of simulation box size  $L$  and lattice spacing  $a_0$  using D3Q26 lattice (in 3D). In order to obtain  $C_{ij}$  numerically, the simulation boxes are subjected to deformation in 6 directions (see Eq. (2.17)).

### Spherical pore embedded in a Matrix

The first validation step was designed to assess the theoretical formulation and numerical implementation by examining homogeneous systems. Next, a heterogeneous case - comprised of a spherical pore centered in a cubic simulation box is considered (see Fig. 2-4).

The porosity can be obtained from:

$$\phi_0 = \frac{n_p}{(n-1)^3} \quad (2.44)$$

with  $n_p$  denoting the number of mass points defining the pore space. The pore radius,  $R$ , was gradually increased, with a maximum pore radius - to - box size ratio  $R/L = 0.45$  corresponding to a porosity  $\phi_0 = \frac{4\pi}{3} (R/L)^3 = 0.38$ . Using a D3Q26 lattice (in 3D), the cubic simulation boxes are discretized. Then, for mass points in the solid domain  $V_s$ , the energy parameters  $\epsilon_i^{n,t}$  are calibrated (see Section 2.2) to reproduce the desired (effective) elastic behavior given the finite size of the simulation box (see Fig. 2-3 for an analogous - in 2D -schematics of the discretization process). The focus of the validation examples is to compare the effective elastic properties one obtains using the discrete approach with analytical expressions of continuum micromechanics based on the assumption of scale separability. In this vein, the pore morphology herein considered is akin to a matrix-pore inclusion microtexture often associated with the Mori-Tanaka effective estimates [93, 10]. Such continuum micromechanics solutions are strictly valid only in the case of scale separability between the size of the heterogeneity (pore size  $R/a_0 = \left(\frac{3}{4\pi}n_p\right)^{1/3}$ ) and the size of the representative volume element (r.e.v. size  $L/a_0 = (n-1)$ ); and hence for  $n_p \ll \frac{4\pi}{3} (n-1)^3$ , a condition to be challenged in the LEM simulations. Eq. (2.40) provides the means to assess the continuum-based estimations of  $C_{ijkl}$  against discrete based LEM computations using Eq. (2.17). We first consider an isotropic solid behavior, defined by a bulk modulus  $k^s = 20$  GPa and a Poisson's ratio of  $\nu^s = 0.2$ . The energy parameters  $\epsilon_i^{n,t}$  for the solid were thus calibrated using Eq. (2.18). The effective stiffness tensor  $\mathbb{C}$  was obtained through evaluation of Eq. (2.17) by considering, in the simulations, appropriate displacement boundary conditions as defined in Eq. (2.41). Fig. 2-6a compares the simulation results with the effective stiffness coefficients obtained from the Mori-Tanaka homogenization scheme, Eq. (2.40). The same cubic simulation boxes were considered to validate the transversely isotropic effective elastic properties from simulation vis-à-vis their continuum counterparts. To this end, the energy parameters  $\epsilon_{ij}^{n,t}$  are calibrated using Eq. (2.28) to reproduce the following solid elastic properties,  $C_{11}^s = 55$  GPa,  $C_{12}^s = 10$

GPa,  $C_{13}^s = 14$  GPa,  $C_{33}^s = 28$  GPa, and  $C_{44}^s = 17$  GPa. Fig. 2-6b shows the comparison of the simulated effective elasticity against the continuum values from the matrix-pore inclusion model captured via Mori-Tanaka effective estimates. For the elastic symmetries considered, LEM simulations compare accurately with the continuum micromechanics based predictions.

## 2.5 Chapter Summary

Lattice Element Method provides a powerful platform to study highly heterogeneous solids keeping in mind its limitations. LEM through a discrete description of solid(s) captures the mechanical interactions between material points in space. Although the presented formulation utilizes harmonic interaction potentials for the case of linear elasticity, the framework can be extended to non-linear behaviors. The choice of lattice network constraints the space of accessible mechanical properties as demonstrated via restrictions for Poisson's ratio in the isotropic case as well as restrictions on  $C_{ij}$  for the transversely isotropic case. This solid mechanics framework presented thus far provides the means to explore the mechanical behavior of highly heterogeneous systems beyond what continuum micromechanics offers. Through introduction of an effective pore pressure force field in Chapter 3, LEM will be extended to study poroelastic response of fully saturated highly heterogeneous porous solids. In Chapter 5, through the combination of LEM with discrete fluid description, this framework will be extended to study the mechanical response of unsaturated heterogeneous porous solids utilizing a slightly modified localized pore pressure force field.

THIS PAGE INTENTIONALLY LEFT BLANK

# Chapter 3

## Mesoscale Poroelasticity of Heterogeneous Porous Solids - Fully Saturated Case

Poromechanics is dedicated to modeling and prediction of how porous materials deform in response to various external loadings. These loadings range from fluid-solid interactions by a variety of pressures at the liquid-solid interface to complex physical chemistry phenomena at the pore scale that produce a mechanical deformation (incl. fracture) of the solid. The classical backbone of poromechanics is based on continuum theories, ever since Maurice A. Biot defined the kinematics of deformation of the skeleton within the classical continuum mechanics framework as the reference for the description of flow of liquid phase through the pore space [16], with the state equations for stress,  $\Sigma$ , and porosity change,  $\phi - \phi_0$ , given in the linear poroelastic case by:

$$\Sigma = \frac{1}{V} \frac{\partial E_{pot}}{\partial \mathbf{E}} = \mathbb{C} : \mathbf{E} - \mathbf{b}p \quad (3.1)$$

$$\phi - \phi_0 = -\frac{1}{V} \frac{\partial E_{pot}}{\partial p} = \mathbf{b} : \mathbf{E} + \frac{p}{N} \quad (3.2)$$

where  $E_{pot}$  is the potential energy of the solid phase of the solid-pore composite of volume  $V$ , subjected to an average strain  $\mathbf{E} = \langle \boldsymbol{\varepsilon} \rangle_V$  at the boundary  $\partial V$ , and a pressure  $p$  at the solid-pore interface.  $\mathbb{C}$  is the fourth-order elastic stiffness tensor,  $\mathbf{b}$  is the second-

order tensor of Biot pore pressure coefficients, and  $N$  denotes the solid Biot modulus. This continuum framework also provided the backbone for the development of the close-to-equilibrium thermodynamics framework of irreversible deformation of porous media pioneered by Coussy [36], and its extension to a large range of phase change and adsorption phenomena [38]. In the same vein, microporomechanics theories can be viewed as refined extensions of the continuum framework to the microscale, in that they adapt continuum micromechanics theory [119, 134] to the specific nature of porous materials viewed as solid-pore composite materials [45, 44]. While the continuum poromechanics theory has entered and transformed many engineering fields ranging from Civil- and Environmental Engineering and geophysics applications to biomechanics and the food industry (see for e.g. [58]), the intrinsic limitations of the theory relate to the very foundations of the continuum model, including scale separability and its impact on the relevance of the differential operators defining the momentum balance and displacement–strain operators. This is a serious limitation of the theory in its applicability to highly heterogeneous materials. For instance, such a continuum theory will fail for microstructure resolutions achieved by micro and nano Computed Tomography (CT) imaging techniques of highly heterogeneous materials, in which the characteristic length scale of the heterogeneity is of a similar scale as the sample size, or for multiscale heterogeneous materials for which a single representative elementary volume (rev) cannot be defined. It is for such systems, that we herein propose a discrete form of poromechanics theory, in which physical interactions replace volume descriptors. This approach is much akin to molecular representations of material systems with interaction forces between mass points derived from potentials that define the out-of-equilibrium state of the system w.r.t. a relaxed equilibrium configuration.

Herein, the elements of such a discrete poromechanics approach are developed using statistical mechanics ensemble definitions within the context of the Lattice Element Method [124, 3] using the framework of effective potentials [78]. By way of validation, some pore-solid morphologies are revisited to determine poroelastic constants within and beyond the classical continuum limits of scale separability.

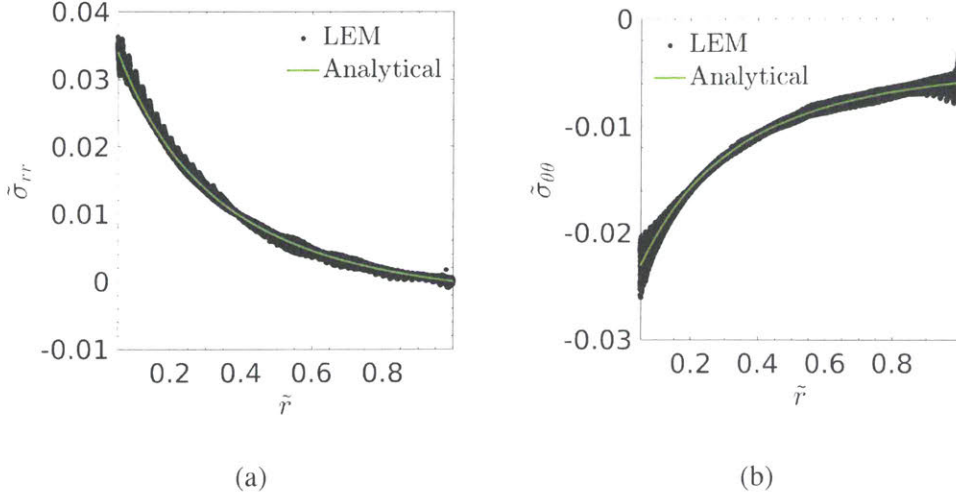


Figure 3-1: Radial -  $\tilde{\sigma}_{rr} = \sigma_{rr}/M_s$  - (3-1a) and tangential -  $\tilde{\sigma}_{\theta\theta} = \sigma_{\theta\theta}/M_s$  - stresses (3-1b) corresponding to Lamé's problem calculated from analytical solutions and numerical simulations.  $M_s$  is the imposed isotropic indention modulus for the solid shell.

### 3.1 Effective Pore-Pressure Force Field Potential

We are interested in the effect of a pressure in the pore space on the deformation behavior of the solid phase. The simplest case is the saturated drained situation, in which the fluid in the pore domain is assumed to communicate with an outside reservoir maintained at a constant pressure  $p$ , so that in the relaxed state, the same pressure will prevail in the pore domain. Such a hydrostatic drained stress state,  $\boldsymbol{\sigma} = -p\mathbf{1}$ , necessarily implies that only central-forces are active on each mass point in the pore domain,  $\vec{F}_i^j = F_i^{j,n} \vec{e}_n$  so that the Virial stress expression for the entire pore domain of volume  $V_p$  and  $N_p$  voxels becomes:

$$\boldsymbol{\sigma} = -p\mathbf{1} = \frac{n_\ell^p}{2V_p} \langle r_{ij} F_i^{j,n} \vec{e}_n \otimes \vec{e}_n \rangle = \frac{1}{2V_p} \sum_{i=1}^{N_p} \sum_{j=1}^{N_i^p} r_{ij} F_i^{j,n} \vec{e}_n^i \otimes \vec{e}_n^j \quad (3.3)$$

where  $n_\ell^p$  denotes number of links in the pore domain. In a zeroth-order description of the microtexture,  $F_i^{j,n}$  and  $r_{ij}$  are considered to be independently distributed and thus not correlated [104, 7] which allows Eq. (3.3) to be expressed as  $\boldsymbol{\sigma} = \frac{n_\ell^p}{2V_p} \langle r F^n \rangle \langle \vec{e}_n \otimes \vec{e}_n \rangle$ , which leads to the equality of traces:

$$3p = \frac{n_\ell^p}{2V_p} \langle r F^n \rangle \quad (3.4)$$

Now, if we consider by analogy with logarithmic equations of state for bulk fluids [100], a logarithmic potential,  $U(r_{ij}) = \omega \ln(l_{ij}^0/r_{ij})$ , and hence  $F_i^{j,n} = -\partial U/\partial r_{ij} = \omega/r_{ij}$ , where  $\omega = \langle rF^n \rangle$  (of dimension of work) can be viewed as a fluid characteristic and should be constant.  $\langle rF^n \rangle$  can be made independent of  $r_{ij}$  (which is dependent on the orientation  $\vec{e}_n$  of the bonds) by simply setting:

$$F_i^{j,n} = -\frac{6p V_p}{r_{ij} n_\ell^p} \quad (3.5)$$

This relation ensures that the mean pressure is  $p$  and the equality Eq. (3.4) is satisfied. This paves the way for imposing a pressure inside a domain discretized by a regular lattice:

$$p = -\frac{\omega n_\ell^p}{6V_p} \quad (3.6)$$

Eq. (5.33) defines the interaction between pore and solid mass points in the form of externally supplied work. This perturbation of the system's equilibrium is resolved through the theory of minimum potential energy as a new equilibrium position is sought through energy minimization (see [78]). Lastly, it is readily recognized that  $\langle \vec{e}_n \otimes \vec{e}_n \rangle$  is the fabric tensor,  $\mathbf{H}^p$ , characterizing the morphology of the pore space. It can be expanded in the following way:

$$\mathbf{H}^p = \frac{1}{n_\ell^p} \sum_{i=1}^{N_p} \sum_{j=1}^{N_i^p} \vec{e}_n \otimes \vec{e}_n \quad (3.7)$$

For Eq. (3.3) to hold, the fabric tensor, Eq. (3.7), should be diagonal,  $\mathbf{H}^p = \frac{1}{3} \text{tr}(\mathbf{H}^p) \mathbf{1}$  with no deviatoric components, i.e.  $\text{dev}(\mathbf{H}^p) = \mathbf{H}^p - 1/3 \text{tr}(\mathbf{H}^p) \mathbf{1} = \mathbf{0}$ , which holds true for any regular lattice. Furthermore,  $\text{tr}(\mathbf{H}^p)=1$  by construction. Note that, if the underlying lattice is not regular and hence not diagonal, then the values of  $F_i^{j,n}$  would have been dependent not only on the average pressure to be imposed, but also the orientations of the bonds.

To validate Eq. (5.33), consider the case of a hollow sphere with inner radius  $a$  and outer radius  $b$  subjected to an internal uniform pressure  $p_i$  and an external uniform pressure  $p_o$ . For this case, there exists an analytical solution due to [75] for the induced radial  $\sigma_{rr}$  and tangential  $\sigma_{\theta\theta}$  stresses:

$$\sigma_{rr} = \frac{p_o b^3 (r^3 - a^3)}{r^3 (a^3 - b^3)} + \frac{p_i a^3 (b^3 - r^3)}{r^3 (a^3 - b^3)} \quad (3.8)$$

$$\sigma_{\theta\theta} = \frac{p_o b^3 (2r^3 + a^3)}{2r^3 (a^3 - b^3)} - \frac{p_i a^3 (2r^3 + b^3)}{2r^3 (a^3 - b^3)} \quad (3.9)$$

where  $r$  denotes the distance from the inner radius. It is important to note that uniform pressures  $p_o$  and  $p_i$  imply full saturation, i.e. a Dirac delta function for probability density function (PDF) of  $p(\vec{x})$  ( $\forall \vec{x} \in V_p$ ). As such, this provides a platform to validate Eq. (5.33) against analytical solutions Eqs. (5.35) and (3.9). The results are shown in Fig. 3-1 with great agreement.

## 3.2 Poroelastic Properties and Ensemble Definitions

The poroelastic properties of materials form much of the backbone of application of the poromechanics theory. This includes the elasticity tensor,  $\mathbb{C}$ , the tensor of Biot coefficients,  $\mathbf{b}$ , and the solid Biot modulus  $N$ . From the composite structure of porous materials, it is readily understood that these macroscopic properties call for averages. Such averages are best defined, in statistical mechanics, within the context of specific statistical ensembles which –at least theoretically– include every possible microscopic state of the system. The advantage of using statistical ensembles for the determination of the poroelastic properties is that each ensemble is associated with a characteristic state function or thermodynamic potential that uniquely define –upon minimization– the equilibrium state of the system in function of a few observable parameters; much akin to the classical minima theorems of elasticity employed in continuum mechanics, e.g. for the derivation of the state equations of poroelasticity Eqs. (3.1) and (3.2) [45, 44]. It is thus shown that making the link between statistical ensembles and such boundary conditions is quite helpful for the determination of the poroelastic constants from discrete simulations.

### 3.2.1 Drained Elasticity Properties in the $NVT$ -Ensemble

The first quantity of interest is the drained elasticity tensor, which is obtained by letting  $p \sim \omega = 0$ . In this drained situation, a regular displacement boundary condition is prescribed at the boundary ( $\partial V$ ) of the simulation box:

$$\vec{\xi} = \mathbf{E} \cdot \vec{x} \quad \forall \vec{x} \in \partial V \quad (3.10)$$

where  $\mathbf{E}$  refers to macroscopic strain tensor. Such a mechanical boundary condition is akin to an  $NVT$ -ensemble (or canonical ensemble) at the *composite* (solid + pore) scale, in that the total number of particles  $N_t$  is constant, the volume (or more generally, the displacement) of the system ( $V$ ) is controlled via the boundary condition Eq. (3.10), and temperature ( $T$ ) is maintained constant. The thermodynamic potential that defines such an ensemble is the Helmholtz free energy  $\Psi$  of the composite system, which realizes a minimum value at equilibrium ( $r \rightarrow r_0$ ). Given the mechanical boundary value problem ( $\mathbf{E}, p = 0$ ), the minimum of the Helmholtz free energy is strictly equivalent to the minimum of the potential energy of the solid phase subjected at its boundary to the (displacement) boundary condition, Eq. (3.10), and a zero pressure in the pore space; and coincides with the free energy of the solid phase(s):

$$E_{pot}^s(\mathbf{E}) = \Psi(N_t, V, T) = \min_{\vec{\delta}_i, \vec{\vartheta}_i} \sum_{links \ ij \in V_0^s} U_{ij}(\vec{\delta}_j - \vec{\delta}_i + \vec{r}_{ij} \times \vec{\vartheta}_i; \vec{\vartheta}_j - \vec{\vartheta}_i) \quad (3.11)$$

The fourth-order stiffness tensor is then obtained by considering the curvature of the potential energy of the system around the relaxed state ( $r \rightarrow r_0$ ):

$$\mathbb{C} = \frac{1}{V} \frac{\partial}{\partial \mathbf{E}} \left( \frac{\partial E_{pot}^s}{\partial \mathbf{E}} \right) \Bigg|_{\omega=0; r \rightarrow r_0} \quad (3.12)$$

### 3.2.2 Biot Pore Pressure Coefficients in the $\mu VT$ -Ensemble

The determination of the tensor of the Biot pore pressure coefficients,  $\mathbf{b}$ , and the solid's Biot modulus,  $N$ , requires some further considerations. From the first macroscopic state equation, Eq. (3.1), it is realized that the tensor of Biot coefficients is obtained from the

average stresses in an experiment where the strain,  $\mathbf{E}$ , is zero, while a constant pressure  $p$  prevails in the pore space; exerting this pressure onto the solid–pore interface. Such conditions are akin to the Grand canonical ensemble or  $\mu VT$  ensemble at the *composite* (solid + pore) scale, in that (1) the porous system is open at a specified chemical potential  $\mu$ ; and (2) the overall volume is conserved with  $\mathbf{E} = \mathbf{0}$ ; and (3) the temperature,  $T$ , is maintained constant. In this  $\mu VT$ -ensemble, the characteristic state function that needs to be minimized is the so called Landau potential (or Grand potential),  $\Omega(\mu, V, T) = \Psi - \mu N_f$ , where  $\Psi$  is the Helmholtz free energy,  $\mu$  the chemical potential and  $N_f$  the number of particles (here fluid particles). For the open system, the free energy is the sum of the free energy of the solid ( $\Psi_s$ ) and of the fluid phase ( $\Psi_f$ ) [see [36] for a detailed derivation of the thermodynamics of the porous continuum as an open system]; and the latter is but the difference between the potential energy of the fluid at constant pressure ( $\mu N_f$ ) and the work by the fluid in the pore space; i.e.  $\Psi_f = \mu N_f - p(V^p - V_0^p)$  (where  $V^p$  and  $V_0^p$  stand for the pore volumes respectively after and before deformation; i.e.  $V^p = V\phi$ ;  $V_0^p = V\phi_0$ , with  $\phi$  the Lagrangian porosity). The Landau potential for the composite system thus reduces to the classical expression of the potential energy of the solid phase for the considered boundary conditions ( $\mathbf{E} = \mathbf{0}, p$ ); that is:

$$E_{pot}^s(\mathbf{E} = \mathbf{0}, p) \equiv \Omega(\mu, V, T) = \min_{\vec{\delta}_i, \vec{\vartheta}_i} \left( \Psi_s^{(\mu VT)} - pV(\phi - \phi_0) \right) \quad (3.13)$$

where  $\Psi_s^{(\mu VT)} = \sum_{links\ ij \in V_0^s} U_{ij}(\vec{\delta}_j - \vec{\delta}_i + \vec{r}_{ij} \times \vec{\vartheta}_i; \vec{\vartheta}_j - \vec{\vartheta}_i)$  is the Helmholtz free energy of the solid phase.

With the characteristic state function thus defined, the inter-particle forces  $\vec{F}_i^j$  in the solid domain are readily determined, permitting the determination of the stress via the virial expression in the composite  $\mu VT$  ensemble:

$$\Sigma^{(\mu VT)} = \frac{1}{2V} \sum_{i \in V} \sum_{j=1}^{N_i^b} \vec{r}_{ij} \otimes \vec{F}_i^j = - \left( \frac{1}{2V} \sum_{i \in V_s} \sum_{j=1}^{N_i^b} \vec{r}_{ij} \otimes \vec{F}_i^j + \phi_0 p \mathbf{1} \right) \quad (3.14)$$

where the first term on the r.h.s. of Eq. (3.14) is the contribution of the solid phase with inter-particle forces  $\vec{F}_i^j = \partial\Psi_s^{(\mu VT)}/\partial\vec{r}_{ij}$ , whereas the second term represents the contribution of the pressure prevailing in the (Lagrangian) porosity,  $\phi_0 = (V_p/V)$ , with pressure  $p$  defined by Eq. (3.6). A straightforward comparison with the classical equation of state of poroelasticity, Eq. (3.1), thus leads to the following definition of the second-order tensor of Biot pore pressure coefficients,  $\mathbf{b}$ :

$$\mathbf{b} = -\frac{\Sigma^{(\mu VT)}}{p} = \frac{1}{p} \left( \frac{1}{2V} \sum_{i \in V_s} \sum_{j=1}^{N_i^b} \vec{r}_{ij} \otimes \vec{F}_i^j \right) + \phi_0 \mathbf{1} \quad (3.15)$$

Hence, all what it takes to obtain the tensor of Biot coefficient is to determine, in the  $\mu VT$  ensemble, the inter-particle forces  $\vec{F}_i^j$  in the solid domain that result from the pore-pressure loading using the Landau potential expression Eq. (3.13).

### 3.2.3 Biot Modulus in the $NPT$ -Ensemble

The classical way of determining the Biot modulus is by means of the so-calledunjacketed test, originally proposed by Biot and Willis [17]. The test consists of placing a sample into a pressure vessel maintained at the same pressure  $p$  as the fluid in the pore space. Such test conditions are akin to the isothermal–isobaric,  $NPT$ -ensemble of the *solid* phase (i.e. at the constituent scale, in contrast to the composite scale), in that (1) the number of solid particles  $N_s$  are maintained constant, (2) the solid is subjected at its (entire) boundary  $\partial V_s$  to a pressure  $p$ , while (3) the temperature,  $T$ , is maintained constant. The thermodynamic potential that characterizes the  $NPT$ -ensemble is the Gibbs free energy of the solid phase,  $G(N_s, p, T)$ , which strictly coincides for the pressure boundary condition to which the solid is subjected to the solid’s potential energy:

$$E_{pot}^s \equiv G(N_s, p, T) = \min_{\vec{\delta}_i, \vec{\theta}_i} (\Psi_s^{(NPT)} - W_p) \quad (3.16)$$

where  $\Psi_s^{(NPT)}$  is the Helmholtz free energy of the solid phase in the considered ensemble:

$$\Psi_s^{(NPT)} = \sum_{\text{links } ij \in V_0^s} U_{ij} \left( \vec{\delta}_j - \vec{\delta}_i + \vec{r}_{ij} \times \vec{\vartheta}_i; \vec{\vartheta}_j - \vec{\vartheta}_i \right) \quad (3.17)$$

while  $W_p = -p (V^s - V_0^s)$  is the external work realized by the prescribed pressure  $p$  on the solids boundary, with  $V^s - V_0^s = V_0 (E_v - (\phi - \phi_0))$  the volume change of the solid phase; that is:

$$W_p = -pV_0 (E_v - (\phi - \phi_0)) \quad (3.18)$$

Herein,  $E_v = (V - V_0) / V_0 = \mathbf{1} : \mathbf{E}$  is the relative volume variation of the simulation box and  $\phi - \phi_0$  represents the change of the (Lagrangian) porosity, compared to the reference porosity  $\phi_0$ . Evaluation of Eq. (3.16) thus requires measurements of the volume strain ( $E_v$ ) and the porosity change ( $\phi - \phi_0$ ) in the simulations (as classically done in laboratory tests using the unjacketed test). Around the equilibrium state, defined by harmonic interactions, such determination can be circumvented, when evoking Clapeyron's formula which permits a direct determination of the free energy of the solid, in the  $NPT$  ensemble, from the external work; i.e.,  $W_p = 2\Psi_s^{(NPT)}$ . This in turn provides a direct means to assess the porosity change from both Eqs. (3.2) and (3.18):

$$(\phi - \phi_0) = \mathbf{b} : \mathbf{E} + \frac{p}{N} = \mathbf{1} : \mathbf{E} + \frac{2\Psi_s^{(NPT)}}{pV_0} \quad (3.19)$$

Finally, we remind ourselves that under the considered boundary conditions in the isothermal-isobaric ensemble (relative to the solid), the effective stress obtained from the Virial expression is zero:

$$\boldsymbol{\Sigma}^{(NPT)} + p\mathbf{1} = \frac{1}{2V} \sum_{i \in V_s} \sum_{j=1}^{N_i^b} \vec{r}_{ij} \otimes \vec{F}_i^j + (1 - \phi_0) p\mathbf{1} = \mathbf{0} \quad (3.20)$$

where the interaction forces,  $\vec{F}_i^j$ , are obtained by minimizing the potential energy in this isothermal-isobaric ensemble (i.e., Eq. (3.16)). If we thus substitute in Eq. (3.19) for the strain tensor  $\mathbf{E} = -\mathbb{S} : (\mathbf{1} - \mathbf{b}) p$ , with  $\mathbb{S} = \mathbb{C}^{-1}$  the drained compliance tensor of the

composite, as predicted by Eq. (3.1) for  $\Sigma^{(NPT)} + p\mathbf{1} = \mathbf{0}$ , the solid Biot modulus is obtained:

$$\frac{1}{N} = \frac{2\Psi_s^{(NPT)}}{p^2 V_0} - (\mathbf{1} - \mathbf{b}) : \mathbb{S} : (\mathbf{1} - \mathbf{b}) \quad (3.21)$$

It should be emphasized that this determination of the Biot modulus is strictly valid only when the behavior of the solid phase is defined by harmonic potentials, for which Clapeyron's formula applies. This still holds for non-harmonic potentials around the equilibrium state,  $r \rightarrow r_0$ , for which most non-harmonic potential expressions (e.g. Lennard-Jones) degenerate to harmonic expressions. The Biot modulus is thus confirmed as a measure of the solid's elasticity around the equilibrium state, much akin to the drained elasticity tensor, as defined by Eq. (3.12).

### 3.3 Application

The proposed discrete model for poroelasticity of heterogeneous porous media is applied to the same set of idealized structures employed to validate LEM - its formulation and numerical implementation (see Section 2.4.2 and Fig. 2-4). The energy parameters  $\epsilon_i^{(n,t)}$  pertaining to the solid phase are calibrated following the method outlined in Chapter 2 and [78].

#### 3.3.1 Solid Potential Parameter Calibration

With a focus on linear poroelasticity, the interactions between mass points of the solid phase(s) (volume  $V_s$ ) are defined by harmonic potentials, requiring the calibration of the energy parameters  $\epsilon_{ij}^{(n,t)}$  for mass points  $i$  belonging to a specific solid phase and link  $j = 1, 26$ , with the understanding that links in same directions have same energy parameters. To this end, the potential energy parameters  $\epsilon_{ij}^{(n,t)}$  are calibrated by inverse application of Eq. (2.18) while satisfying Eq. (2.26) for the isotropic case and Eq. (2.28) while respecting Eq. (2.31) for the transversely isotropic case.

### 3.3.2 Continuum Microporomechanics Reference Solutions

The focus of the validation examples is to compare the poroelastic properties one obtains using the statistical mechanics based discrete approach with analytical expressions of microporomechanics based on the assumption of scale separability. In this vein, the pore morphology herein considered is akin to a matrix-pore inclusion microtexture often associated with the Mori-Tanaka effective estimates [93, 10]. Due to [45, 44] it is possible through linear homogenization methods to evaluate the tensor of Biot pore pressure coefficients, with  $\phi_0 \mathbf{1}$  and  $\mathbf{1}$  as its lower and upper bounds, respectively:

$$\mathbf{b} = \mathbf{1} : (\mathbb{I} - \mathbb{S}^s : \mathbb{C}) \quad (3.22)$$

as well as the solid Biot modulus:

$$\frac{1}{\mathbf{N}} = \mathbf{1} : \mathbb{S}^s : (\mathbf{b} - \phi_0 \mathbf{1}) \quad (3.23)$$

where  $\mathbb{C}$  is defined in Eq. (2.40). For a pore-solid composite exhibiting micro- and macro-isotropic behavior, i.e.  $\mathbb{C} = 3K\mathbb{J} + 2G\mathbb{K}$  and  $\mathbf{b} = b\mathbf{1}$ , Eqs. (2.40), (3.22) and (3.23) simplify as follows [44]:

$$\frac{K}{k^s} = \frac{4g^s (1 - \phi_0)}{3k^s \phi_0 + 4g^s} \quad (3.24)$$

$$\frac{G}{g^s} = \frac{(9k^s + 8g^s) (1 - \phi_0)}{(6\phi_0 + 9) k^s + (12\phi_0 + 8) g^s} \quad (3.25)$$

$$b = 1 - \frac{K}{k^s} \quad (3.26)$$

$$\frac{1}{\mathbf{N}} = \frac{b - \phi_0}{k^s} \quad (3.27)$$

For the transversely isotropic case, Eqs. (3.22) and (3.23) in this case, i.e.  $\mathbf{b} = b_1 (\mathbf{1} - \vec{e}_3 \otimes \vec{e}_3) + b_3 \vec{e}_3 \otimes \vec{e}_3$ , read:

$$b_1 (= b_2) = 1 - (S_{11}^s + S_{12}^s) (C_{11} + C_{12}) - S_{13}^s (C_{11} + C_{12} + 2C_{13}) - S_{33}^s C_{13} \quad (3.28)$$

$$b_3 = 1 - 2S_{11}^s C_{13} - 2S_{12}^s C_{13} - 2S_{13}^s (C_{13} + C_{33}) - S_{33}^s C_{33} \quad (3.29)$$

$$\frac{1}{N} = 2 (b_1 - \phi_0) (S_{11}^s + S_{12}^s + S_{13}^s) + (b_3 - \phi_0) (2S_{13}^s + S_{33}^s) \quad (3.30)$$

Furthermore, we utilize the indentation moduli expressions for transversely isotropic materials, which nicely condense the different macro- and micro-stiffness parameters into two single elasticity parameters that can be probed in contact experiments, in and normal to the axis of rotational symmetry [41]:

$$\frac{M_3(x_3)}{m_3^s} = \frac{2}{m_3^s} \sqrt{\frac{C_{11}C_{33} - C_{13}^2}{C_{11}} \left( \frac{1}{C_{44}} + \frac{2}{\sqrt{C_{11}C_{33} + C_{13}}} \right)^{-1}} \quad (3.31a)$$

$$\frac{M_1(x_1)}{m_1^s} \simeq \frac{1}{m_1^s} \sqrt{\sqrt{\frac{C_{11}}{C_{33}} \frac{C_{11}^2 - C_{12}^2}{C_{11}}} M_3} \quad (3.31b)$$

where  $m_3^s$  and  $m_1^s$  are the indentation moduli of the solid phase. As discussed before, these continuum micromechanics solutions are strictly valid only in the case of scale separability between the size of the heterogeneity (pore size  $R/a_0 = \left(\frac{3}{4\pi}n_p\right)^{1/3}$ ) and the size of the representative volume element (r.e.v. size  $L/a_0 = (n-1)$ ). The continuum relations are thus an ideal target to compare with the discrete solutions, using Eq. (3.12) for the elasticity, and the ensemble definitions of the tensor of Biot coefficients Eq. (3.15) and of the solid Biot modulus Eq. (3.21), respectively.

### 3.3.3 Validation Results

The same cubic simulation boxes as those in Section 2.4.2 and with same elastic solid behaviors are considered. For the isotropic solid case, the effective moduli,  $K$  and  $G(=C_{44})$ , are displayed in Figs. 3-2a and 3-2b, respectively. With regards to the poroelastic properties, we first consider the  $\mu VT$  ensemble and the discrete definition of Biot pore pressure coefficient,  $b$ . We impose a pressure  $p/k^s = 0.05$  inside the pore space employing

Eq. (3.6) in the  $\mu VT$  ensemble. Utilizing the theorem of minimum potential energy as stated in Eq. (3.16), inter-particle forces  $\vec{F}_i^j$  induced from the pore-pressure loading are obtained. This paves the way to evaluate  $b$  from Eq. (3.15). Fig. 3-3a compares the simulation results with the reference solution (see Eq. (3.26)), using either the previously determined effective bulk moduli,  $K$  (labeled "Direct" in Fig. 3-2a) or the Mori-Tanaka estimate (labeled "MT" in Fig. 3-2a) via Eq. (3.24). Lastly, we obtain Biot solid modulus,  $N$ , by considering its  $NPT$  ensemble definition, Eq. (3.19), which in the isotropic case reads:

$$\frac{1}{N^{(NPT)}} = \frac{2U^{(NPT)}}{p^2 V_0} - \frac{3(b-1)^2}{C_{11} + 2C_{12}} \quad (3.32)$$

The evaluation is achieved here by prescribing, in the simulations, a pressure  $p/k^s = 0.05$  both inside the pore space utilizing Eq. (3.6) and on the boundaries of the simulation box. Thus, all it takes for obtaining  $N$  from Eq. (3.32) is the computation of the free energy of the solid,  $U^{(NPT)}$ , once the structure finds its new equilibrium through Eq. (3.16), and the previously determined Biot coefficient. Fig. 3-3b displays the comparison between the  $NPT$ -simulation results, using  $b$  from discrete theory in the  $\mu VT$  ensemble labeled as " $LEM(NPT)^*$ " and  $b$  determined directly from simulated effective elasticity in LEM, labeled as " $LEM(NPT)^{**}$ " against its continuum reference solution, Eq. (3.27), labeled in Fig. 3-3b as "Direct".

For the transversely isotropic solid case, the condensed elasticity content via the normalized indentation moduli - Eq. (3.31) - from both simulations and continuum based estimates (see Eq.(2.40) and Fig. 2-6b) is displayed in Figs. 3-2b and 3-2d. Using the same  $\mu VT$  simulation strategy as in the isotropic case, a pore pressure loading normalized by the average Voigt-Reuss-Hill (VRH) bulk modulus for materials with hexagonal symmetry (see e.g. [13]),  $p/k_{VRH}^s = 0.05$  is imposed. Figs. 3-4a and 3-4b display a comparison of the  $\mu VT$  simulation results of the Biot coefficients of the considered transversely isotropic medium,  $\mathbf{b} = b_1(\mathbf{1} - \vec{e}_3 \otimes \vec{e}_3) + b_3 \vec{e}_3 \otimes \vec{e}_3$ , with the analytical solutions Eqs. (3.28) and (3.29) using as inputs either the simulated effective elasticity obtained by LEM, labeled as "Direct" or the analytical homogenized elasticity as obtained from Eq. (2.40), labeled

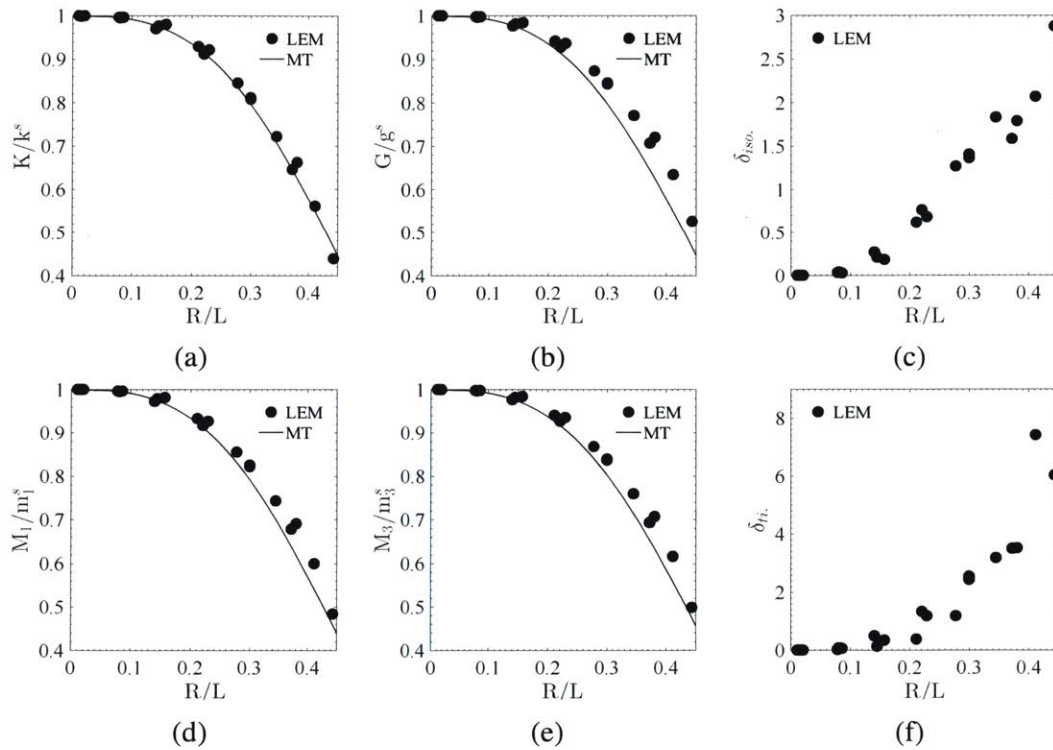


Figure 3-2: Normalized bulk (3-2a) and shear (3-2b) moduli, normalized indentation moduli (3-2c and 3-2d);  $\delta_{iso}$  (3-2e) and  $\delta_{ti}$  (3-2f) versus  $R/L$  for isotropic and transversely isotropic cases, respectively. "MT" refers to Mori-Tanaka continuum solution whereas "LEM" represents discrete simulations.

"MT". Finally, a comparison of the  $NPT$  simulation results with the analytical expression, Eq. (3.30), is shown in Fig. 3-4c, displaying the evolution of the solid Biot modulus  $N$  with  $R/L$ . In the evaluation of  $N$  from the  $NPT$  simulation results (i.e. same pressure  $p/k_{VRH}^s = 0.05$  imposed on the pore wall and on the simulation box), a specification of Eq. (3.19) for the transversely isotropic case reads:

$$\frac{1}{N^{(NPT)}} = \frac{2U^{(NPT)}}{p^2 V_0} - \frac{2C_{11} (b_1 - 1)^2}{(C_{11} - C_{12})(C_{11} + 2C_{12})} + \frac{(b_3 - 1)((b_3 - 1)(C_{11} + C_{12}) - 4C_{13}(b_1 - 1))}{C_{33}(C_{11} + C_{12}) - 2C_{13}^2} \quad (3.33)$$

where  $U^{(NPT)}$  is the free energy of the solid links in the  $NPT$  ensemble, while the effective elasticity  $C_{ij}$  and Biot coefficients  $b_1$  and  $b_3$  are previously determined by simulations (see Figs. 2-6b, 3-4a and 3-4b).

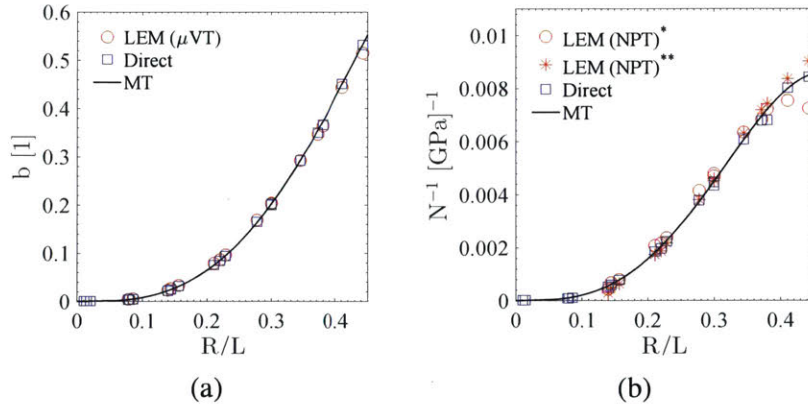


Figure 3-3: These plots correspond to the isotropic solid case. 3-3a: Simulated  $b$  labeled as "LEM ( $\mu VT$ )", continuum based  $b$  calculated from effective elasticity obtained from simulations in LEM, labeled as "Direct" and  $b$  estimated from Mori-Tanaka labeled as "MT". 3-3b:  $N$  with simulated  $b$  labeled as "LEM ( $NPT^*$ )", with calculated  $b$  determined directly from simulations in LEM, labeled as "LEM ( $NPT^{**}$ )".  $N$  from Mori-Tanaka estimation is labeled as "MT".

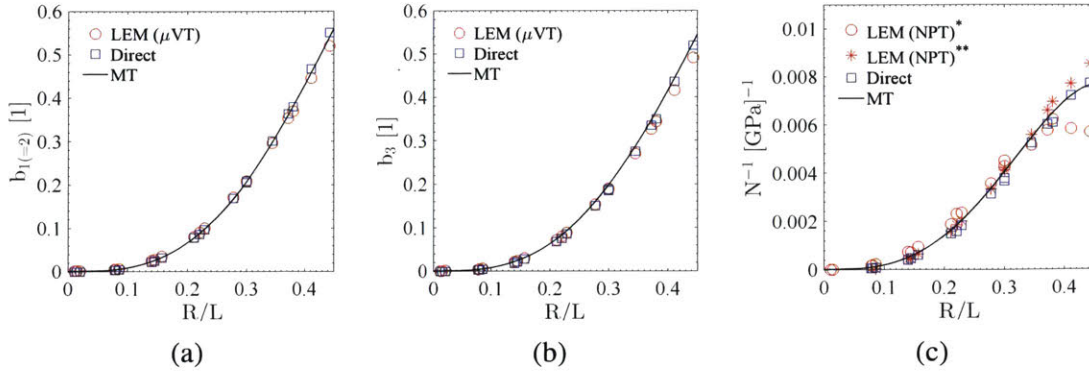


Figure 3-4: These plots correspond to the transversely isotropic solid case. 3-4a and 3-4b: Simulated  $b_1$  and  $b_3$  labeled as "LEM ( $\mu VT$ )", continuum based  $b_1$  and  $b_3$  using effective elasticity obtained from direct simulations, labeled as "Direct" and the Mori-Tanaka estimations labeled as "MT". 3-4c:  $N$  using  $b$  from simulations labeled as "LEM (NPT\*)" and from  $b$  obtained through direct effective elasticity simulations labeled as "LEM (NPT\*\*)". The Mori-Tanaka estimation for  $N$  is labeled as "MT".

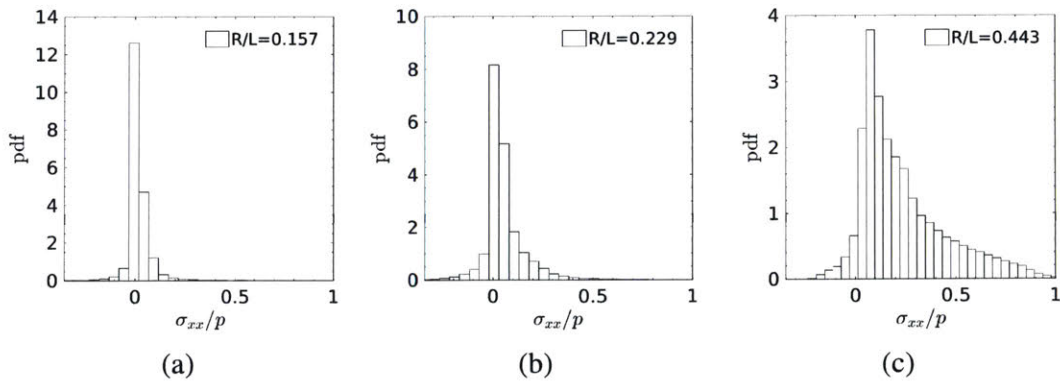


Figure 3-5: Probability density functions of  $\sigma_{xx}/p$  in the  $\mu VT$  ensemble for the considered matrix-pore structures for a transversely isotropic solid. Among the three  $R/L$  ratios plotted, one can observe the long distribution tails for  $R/L = 0.443$ , indicative of high stress concentration between the pore wall and simulation boundary box.

### 3.4 Discussions

The idealized structures considered in this study represent a microtexture best captured by the Mori-Tanaka homogenization scheme. The Mori-Tanaka scheme is often associated with a matrix-inclusion microtexture where the matrix phase overshadows the mechanical response of the inclusion phase(s), while considering interactions between inclusions and it corresponds to (in contrast to the dilute scheme; see, for instance, [44]). Furthermore, for a two-phase composite with spherical inclusions, the Mori-Tanaka scheme corresponds to the Hashin-Shtrikman bounds [132] and specifically for spherical voids, the upper Hashin-Shtrikman bound. However, it is worth noting that the presented methodology to estimate poroelastic properties of heterogeneous media is independent of microtextures being considered.

While the discrete simulation results compare well against their continuum poroelastic counterparts for both the isotropic and the transversely isotropic cases, a deviation is observed at higher porosity values that merit further discussion. Specifically, for small porosities,  $\phi_0 < 5 \times 10^{-3}$  (or  $R/L \leq 0.1$ ), the two approaches provide similar results. This is not surprising since – within this limit – scale separability, delineating the domain of application of the continuum models (here the Mori-Tanaka model) strictly applies. Beyond that limit, however, the results obtained from the discrete and the continuum approach begin to differ. One possible reason for the observed deviations is related to finite size effects associated with the finite size of the simulation box, noting that the elementary voxel size ( $a_0$ ) remains much smaller than the size of the elementary heterogeneity at high porosities. To explore this further, we define two quantities,  $\delta_{iso.}$  and  $\delta_{ti.}$ , that capture a possible deviation from the imposed elastic solid symmetry for the isotropic and transversely isotropic cases; that is, for the isotropic case:

$$\delta_{iso.} = \frac{|C_{44} - \frac{1}{2}(C_{11} - C_{12})|}{C_{44}} \times 100 \quad (3.34)$$

and for the transversely isotropic case:

$$\delta_{ti.} = \frac{|C_{66} - \frac{1}{2}(C_{11} - C_{12})|}{C_{66}} \times 100 \quad (3.35)$$

Using the elasticity constants  $C_{ij}$  obtained from the simulations, Figs. 3-2e and 3-2f plot  $\delta_{iso.}$  and  $\delta_{ti.}$  vs.  $R/L$ , showing that for  $R/L > 0.1$  the effective (i.e. composite) elasticity content captured by the simulations departs from the material symmetries of the solid phase. Within the range of considered values,  $\delta_{iso.} \leq 4$  in the isotropic case and  $\delta_{ti.} \leq 8$  in the transversely isotropic case. On the other hand, we also note the deviation of the simulation results from the continuum counterparts for the poroelastic constants (see Figs. 3-2e, 3-2f), for which the continuum solutions (i.e. Eqs. (3.26), and (3.27)) in the isotropic case, and Eqs. (3.28) through (3.30) for the transversely isotropic case) hold irrespective of elastic homogenization scheme. Thus, the observed deviation between discrete simulations and continuum calculations in the high porosity limit for elastic and poroelastic properties seem to be rooted in the finite size of the system as it challenges both the application of Eshelby's solution for an ellipsoidal inclusion in an infinite medium [48] and Mori-Tanaka homogenization scheme's subsection of inclusions to the first moment (mean) of matrix stresses [93, 10]. The same deviation is observed for highly disordered systems [77] but attributed to the high stress concentrations between pore walls. In this vein, the histograms of normalized solid stresses of our idealized pore-matrix structures in the  $\mu VT$  ensemble are plotted in Fig. 3-5 for three different  $R/L$  ratios. In violation of scale separability, for  $R/L = 0.157$  and  $R/L = 0.229$  normalized stresses follow Gaussian distributions. However, the long tails for  $R/L = 0.443$  indicate areas of high stress concentration, a feature not captured by mean-field based theories of micromechanics. This is intimately related to the requirement of scale separability in homogenization theory. A key property of scale separability exploited in the theory of homogenization is that the local problem cannot see the boundaries [97] which clearly is violated in cases of high  $R/L$  ratios studied here.

Surface energy effects are incorporated in poromechanics by making a distinction between the free energy stored elastically into the solid matrix,  $\psi_s$ , and energy  $u$  stored at the solid-fluid interface; such that  $\Psi_s = \psi_s(\mathbf{E}, p) + u(\mathbf{E}, p)$ , with the energy balance for the interface at equilibrium expressed as [127, 25]:

$$du = \tilde{\sigma}^s ds \quad (3.36)$$

where  $\tilde{\sigma}^s$  denotes surface stress and  $s$  represents the actual area of the pore walls per unit volume of porous material in its reference configuration. Furthermore, for example in the case of adsorption in a linearly elastic isotropic porous material, one can obtain material parameters  $\alpha_\epsilon$  and  $\alpha_\varphi$ , to quantify strain and porosity changes due to surface stresses, respectively [127]. In this vein, the proposed method can be extended to capture adsorption-induced structural phase transitions in a porous material employing an osmotic ensemble [116, 87, 35]:

$$\Omega_{os.}(T, P) = \Psi_s + PV - \int_0^P N_{ads.}(T, p) V_m(T, p) dp \quad (3.37)$$

where  $T, P, \Psi_s, V, N_{ads.}$  and  $V_m$  are temperature, pressure, the free energy of the solid in the absence of adsorbed molecules, the volume of the porous host, the number of adsorbed molecules inside the host, and the molar volume of the adsorbing species in its bulk state, respectively. Then, one seeks for the structure that minimizes  $\Omega_{os.}$ . Once this structure is obtained,  $N_{ads.}(T, P)$  can be predicted with standard Grand Canonical Monte Carlo (GCMC) simulations. Classically, the main challenge of using Eq. (3.37) is access to  $\Psi_s$ , which would be readily available via LEM.

### 3.5 Chapter Summary

As the resolution of microtexture and heterogeneity of porous materials is progressing rapidly thanks to advancements in e.g. CT-imaging techniques [63], there is a need to adapt the tools of poromechanics to model and to predict the deformation of porous materials in response to various external loadings. The discrete poromechanics approach proposed and implemented in the Lattice Element Method (LEM) aims at contributing to this effort, well beyond the classical mean-field based theories of continuum microporomechanics which do not capture microtextural information beyond one-point correlation functions and confined in its application by the scale separability condition. Specifically, the discrete nature of the approach provides access to local stresses and displacements as well as force flow in a heterogeneous system, which can enrich our understanding of stress and strain localization

in a multiphase porous composite, and form a basis for subsequent refinements to include irreversible deformation (incl. fracture), deformation during flow, and so on. The following points of observation deserve attention:

1. The discrete approach herein proposed considers a porous materials as an ensemble of mass points that interact via forces and moments that derive from effective potentials. Illustrated here for harmonic potentials for both 2-body and 3-body interactions, it is thus readily understood that both the solid and the composite responses are relevant for linear poroelastic theory only. However, this linear discrete poromechanics model can, in a straightforward manner, be extended to the nonlinear case through the consideration of non-harmonic effective potentials (such as Lennard-Jones, Morse potential, and so on), whose Taylor expansion around the (undeformed) equilibrium configuration is the harmonic case. Otherwise said, the calibration procedure herein suggested for the interaction energies ('well-depth') remain valid and just need to be refined to calibrate the nonlinear potential parameters. As such, LEM can be contrasted with finite-element based approaches, as it provides a consistent framework to coarse grain interaction potentials validated at a lower scale.
2. Re-formulated within the context of statistical physics, the discrete approach thus derived provides access to the classical poroelastic properties of highly heterogeneous porous materials as macroscopic properties relevant to specific statistical ensemble definitions. It was thus shown, that the results from an  $\mu VT$ -ensemble provide access to the tensor of Biot pore pressure coefficients,  $\mathbf{b}$ , while the results from an  $NPT$ -ensemble permit determination of the Biot solid modulus,  $\mathbf{N}$ . To achieve this goal, an original reformulation of drained pressure conditions was proposed to translate pressure in the pore space into interaction forces. While the approach was here derived for a constant pressure prevailing in the pore space, it could equally be applied to varying pressures prevailing in the pore space. The approach as such could thus possibly be used for coupled flow-deformation problems, and via some minor adaptation for partially saturated situations, which will be reported in future work.
3. The discrete approach herein proposed removes by its very nature the assumption of

scale separability that delineates continuum microporomechanics approaches. This opens new insights into the intimate interplay between constituent behavior and composite behavior of porous materials. We view the proposed approach as a powerful tool to link micro- to macro-behavior of porous materials; specifically for porous materials exhibiting a large size range of heterogeneities that does not permit scale separation.

**THIS PAGE INTENTIONALLY LEFT BLANK**

## **Chapter 4**

# **Application to Real Heterogeneous Porous Media from Imported Computed Tomography Scans**

It is well known that the effective mechanical and poromechanical properties of heterogeneous media depend on the chemical composition, mechanical properties of the constituents, as well as their spatial distributions. In recent years, the combination of multi-scale micromechanics based models and grid nanoindentation [34, 126], later coupled with wave dispersive spectroscopy [40], have played a significant role in providing insights into the mechanics of heterogeneous porous solids. However, classical continuum micromechanics [119, 134] and continuum microporomechanics [45, 44] based homogenization methods, primarily built on Eshelby's inclusion problem [48] and scale separations, reduce the spatial distribution of the constituents and their mechanical interactions to effective textures, namely matrix/inclusion [93, 10] and granular [60, 74, 26, 61]. The failure of continuum based approaches to explicitly incorporate mesoscale texture effects by accounting for spatial distribution of constituents and the local variations of mechanical properties limit their ability to provide insights into the mechanics of highly heterogeneous media. In addition, perturbation based solutions in statistical continuum mechanics are limited to small fluctuations in mechanical properties [11] and thus unable to capture heavy-tailed distributions characteristics of highly heterogeneous media. Moreover, challenges involved with

defining a representative elementary volume that satisfies scale separability delineate the intrinsic limitations of the continuum model in dealing with highly heterogeneous media. Meanwhile, emerging modeling and simulation techniques propelled by high-performance computing has paved the way for multi-scale, multi-physics material modeling, providing a link between micro-scale mechanisms and functional behavior at the macro-scale. More recently, high resolution imaging techniques such as computed tomography (CT) scans on porous heterogeneous solids (see for e.g.[63, 112] ) have provided access to spatial distribution of pore and solid phases, paving the way to isolate mesoscale textural contribution to the effective elasticity via direct importation of such scans into a computational framework. Subsequently, the calibration of elastic energy content of a heterogeneous porous solid for a finite-sized simulation box against lab measured mechanical data can serve as a departure point for simulating other phenomena such as wave propagation, plastic deformation, fracture and so on. To address the limitations of continuum based approaches in dealing with highly heterogeneous materials while utilizing advancements in high-performance computing and imaging techniques, we present a methodology to calibrate and to validate effective solid potentials of heterogeneous porous solids from experimentally measured nanoindentation data and imported CT scans. In addition to providing insights into the interplay of effective poroelastic behavior and microtextural features, such a framework can be utilized to design new sustainable and durable materials with imposed effective mechanical behavior, with applications ranging from car manufacturing, aerospace industry to biological tissue engineering given the advancements in additive manufacturing and machine learning algorithms.

In this study, CT scans and lab measured distributions of grid-nanoindentation moduli on two organic-rich shales are employed. First two cumulants of experimentally measured distributions are used for calibration of effective interaction potentials of the solids. To this end, sub-volumes of characteristic length similar to that of a volume activated when probed by a nanoindenter are first extracted and grouped into calibration and validation structure sets. Utilizing Lattice Element Method [59, 124, 3] and the framework of effective interaction potentials [78] (see Chapter 2), elasticity of the solid phases, with spatial

fluctuations within a phase, are calibrated using the calibration structure set. Then, the validation structure set is utilized as independent means for validation. With the elastic energy contents calibrated, Biot poroelastic coefficients are simulated using ensemble-based definitions for highly heterogeneous media [91] (see Chapter 3). Lastly, analyses of stress transmissions through larger sub-volumes extracted from the scans highlight the distinct underlying microtextural features and load-bearing phases in each case.

## 4.1 Materials

Computed tomography (CT) scans on samples from two different organic-rich shale formations (see [63] for details) are employed in this work. These CT scans are taken on samples of dimensions  $64 \mu\text{m} \times 64 \mu\text{m} \times 100 \mu\text{m}$  with a 5.4 keV energy source and a resolution of approximately 64 nm. Such recently developed advanced imaging techniques provide the spatial distribution of different constituents of real materials. The same group of samples have been characterized extensively using instrumented nanoindentation, Energy-Dispersive X-ray spectroscopy (EDX) and X-Ray Diffraction (XRD) [1]. In addition, the organic contents have been modeled from reconstructed kerogen structures utilizing a Hybrid Reverse Monte-Carlo Simulation (HRMC) method [24]. Herein, scan A refers to segmented CT data taken from Antrim formation with its organic content considered to be immature while scan B represents the segmented CT data associated with the Haynesville formation with its organic content considered to be mature [63, 1]. Maturity refers to the process of physical, chemical and structural evolution of organic content with geologic time due to exposure to high pressure and high temperature environments [123, 111]. Such evolution results in microtextural changes that impact the effective poroelastic behavior of organic-rich shales as a geocomposite [92]. Utilizing an informed Otsu's method, Hubler et al. [63] segmented the CT scans by grouping all their constituents into four phases - three solid phases (clay, inclusions, organics) and a pore phase. The organics phase is considered to be kerogen. The inclusions phase encompasses all inorganic solids other than clay. A cross-section from scan B is displayed in Fig. 4-1, highlighting the well-preserved features of the raw data in the segmented image.

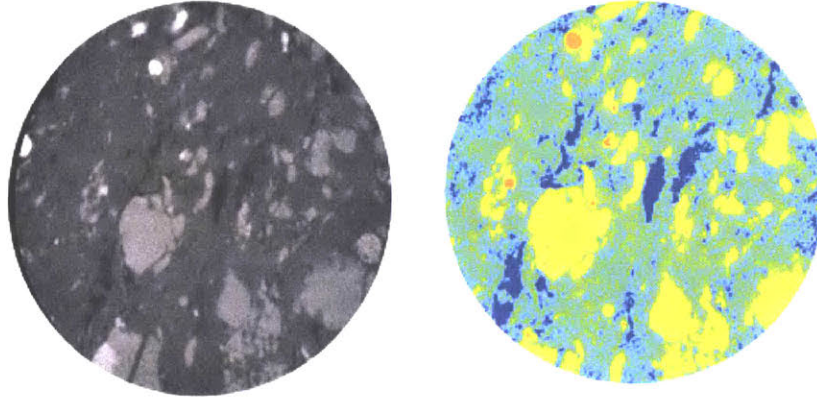


Figure 4-1: A cross-section of scan B displaying raw CT data (left) and the segmented image (right).

#### 4.1.1 Calibration & Validation Structure Sets

Instrumented grid-nanoindentation experiments have been shown to be an effective tool for characterizing the mechanical response of highly heterogeneous media [34, 126]. Hence, the proposed methodology to calibrate effective elastic potential of constituents of a highly heterogeneous, multi-solid phase, porous medium utilizes instrumented nanoindentation data. This is done by extracting sub-volumes from the stack of CT scans, i.e. 3D volume, that correspond to the volume activated by a nanoindenter. Considering an average indentation depth of  $900\text{ nm}$  results in an activated volume with a characteristic length of about  $3 \times 900\text{ nm}$  [76]. This translates into cubic sub-volumes of  $42 \times 42 \times 42$  voxels, given the  $64\text{ nm}$  resolution of the CT scans. From each scan, 1,000 spatially random sub-volumes are extracted. This forms the calibration structure sets (CSS). The remaining 1,300 sub-volume from scan A and 2,886 sub-volumes from scan B make up the validation structure sets (VSS). The probability density function (PDF) of volume fractions for clay, inclusions, kerogen and pore phases  $(f^{clay}, f^{inc}, f^{ker}, \phi)$  are plotted in Figs. 4-2 and 4-3 for scan A and B respectively and as a function different coarse-graining length scale,  $\lambda$ , which characterizes the length of the extracted cubic sub-volumes and will be explored more later in this paper.

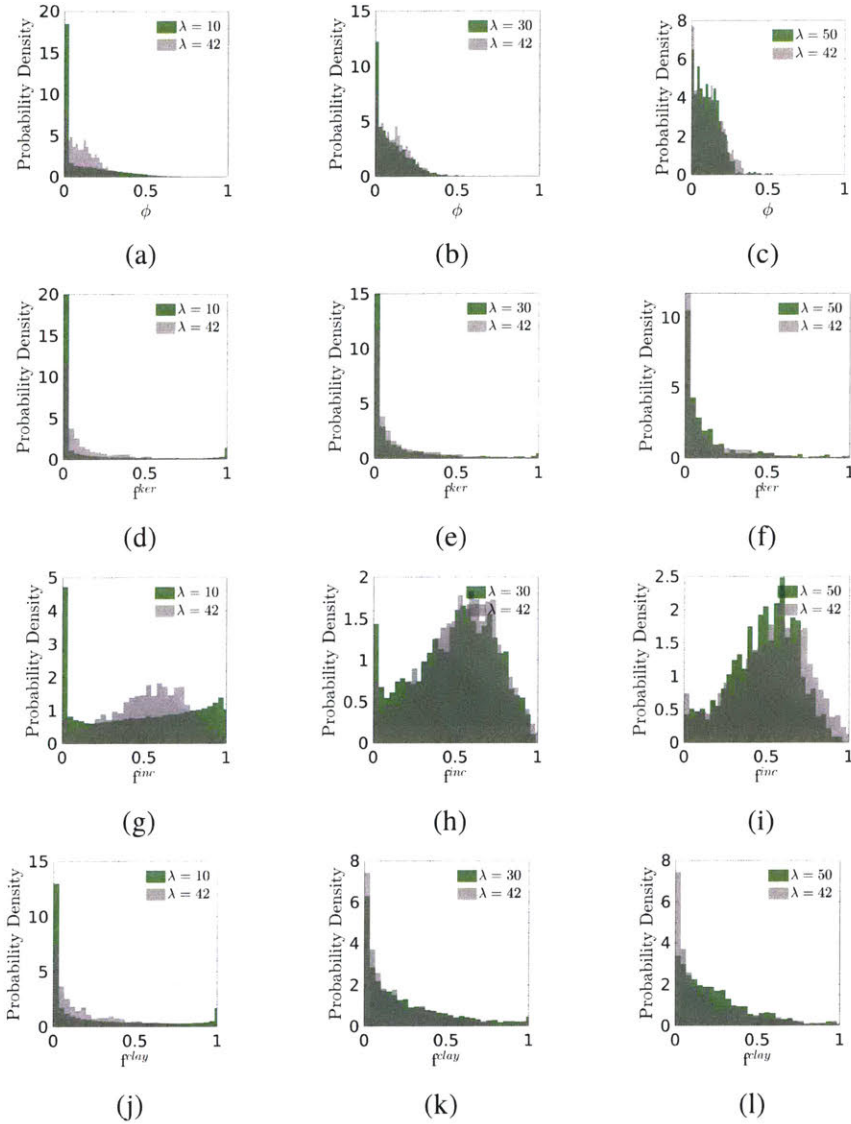


Figure 4-2: Probability density functions for the volume fraction of the considered four phases as a function of coarse-graining length-scale  $\lambda$  in scan A.

## 4.2 Methodology for Calibrations of Energy Parameters

Organic-rich shales are considered to exhibit a transversely isotropic elastic behavior at the length scale relevant to nanoindentation experiment. Lab measured instrumented nanoindentation moduli, characterizing this anisotropic behavior, are employed as means for calibration of the effective potentials of the solid constituents. The experimental data represent a material's response to a nanoindenter as it probes the sample on a pre-determined grid. For a transversely isotropic media, for which the non-zero components of the stiff-

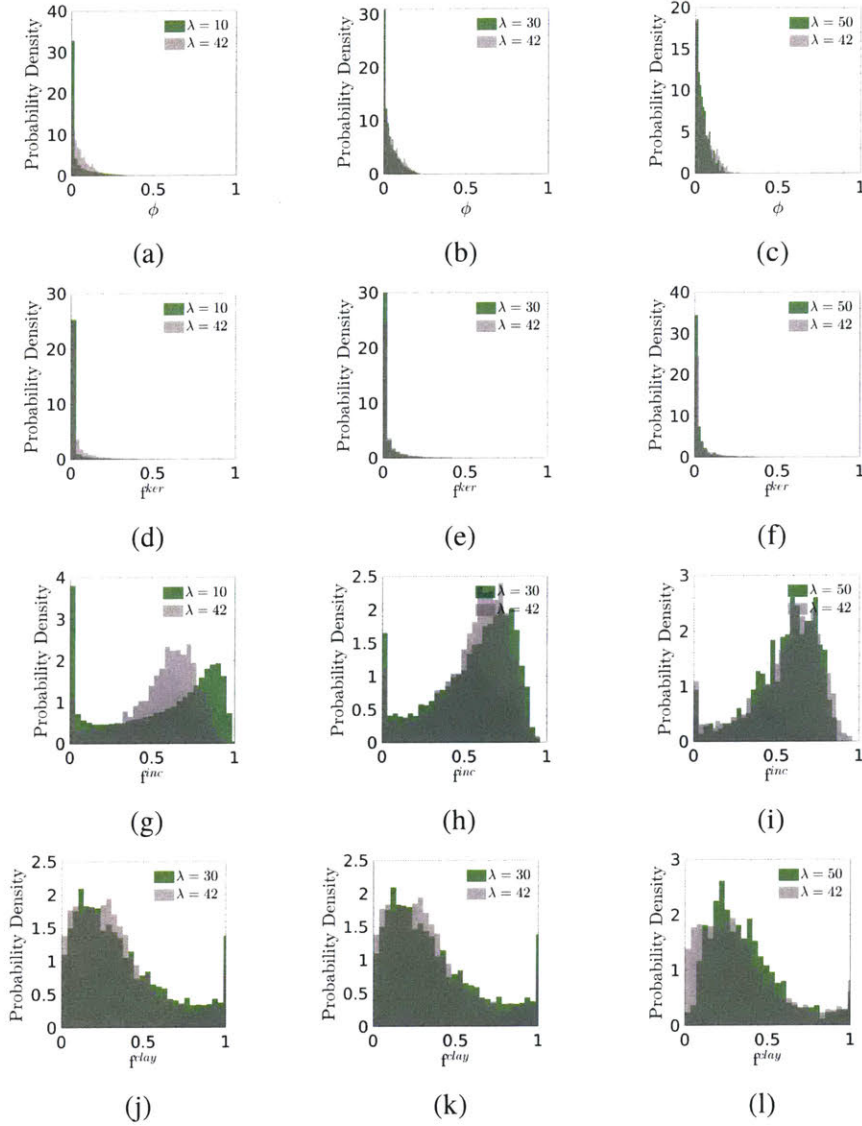


Figure 4-3: Probability density functions for the volume fraction of the considered four phases as a function of coarse-graining length-scale  $\lambda$  in scan B.

ness tensor – in Voigt notation – are  $C_{11} = C_{22}$ ,  $C_{12}$ ,  $C_{13} = C_{23}$ ,  $C_{33}$ ,  $C_{44} = C_{55}$ , while  $C_{11} - C_{12} = 2C_{66}$ ; the indentation moduli are expressed in Eqs. (3.31). The calibration procedure involves simulating the full stiffness tensor associated with each sub-volume in the calibration structure sets and utilizing Eqs. (3.31) to calculate the associated indentation moduli. Then, by the means of first two cumulants of the distributions of both simulated and experimental measured moduli, the effective potentials of the constituents are calibrated. The distributions of experimentally measured indentation moduli for scan A and scan B are plotted in Figs. 4-4 and 4-5, respectively. The first and second cumulants of a distribution,

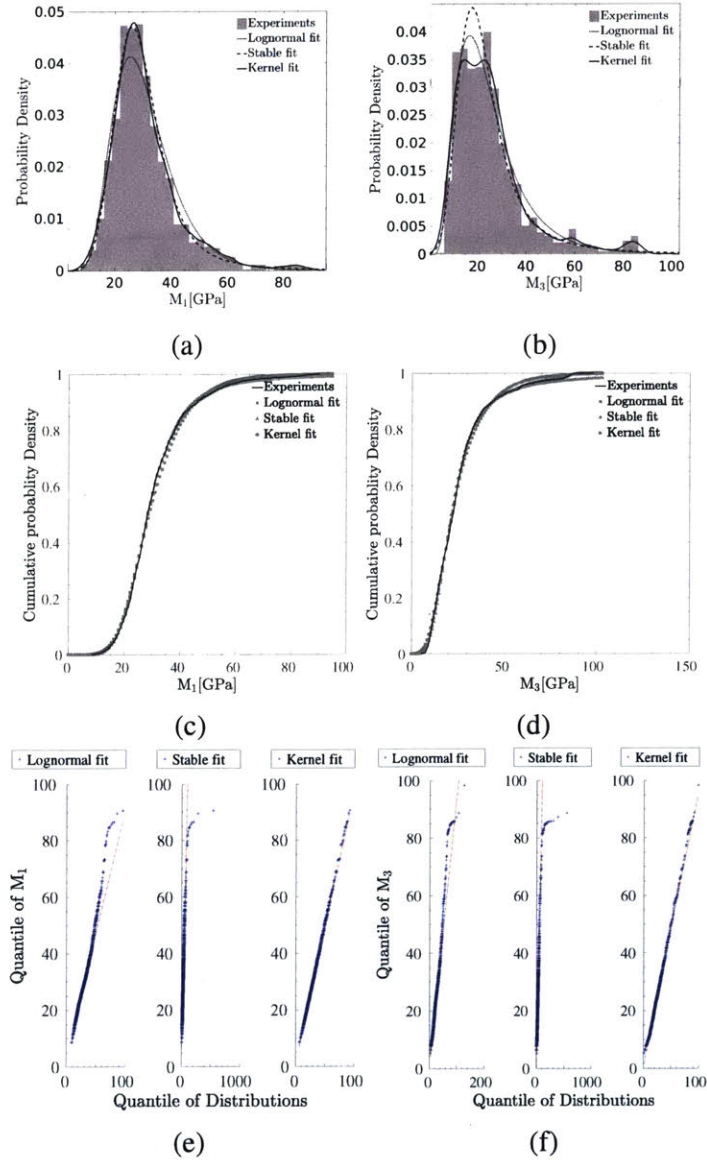


Figure 4-4: Probability density (4-4a and 4-4b), cumulative probability density (4-4c and 4-4d) and quantile-quantile plots (4-4e and 4-4f) for experimentally measured nanoindentation moduli for scan A with fitted Lognormal, Stable and non-parametric normal kernel distributions.

also known as the mean and the variance of a distribution respectively, are defined as:

$$\langle x \rangle_c = \langle x \rangle \quad (4.1)$$

$$\langle x^2 \rangle_c = \langle x^2 \rangle - \langle x \rangle^2 \quad (4.2)$$

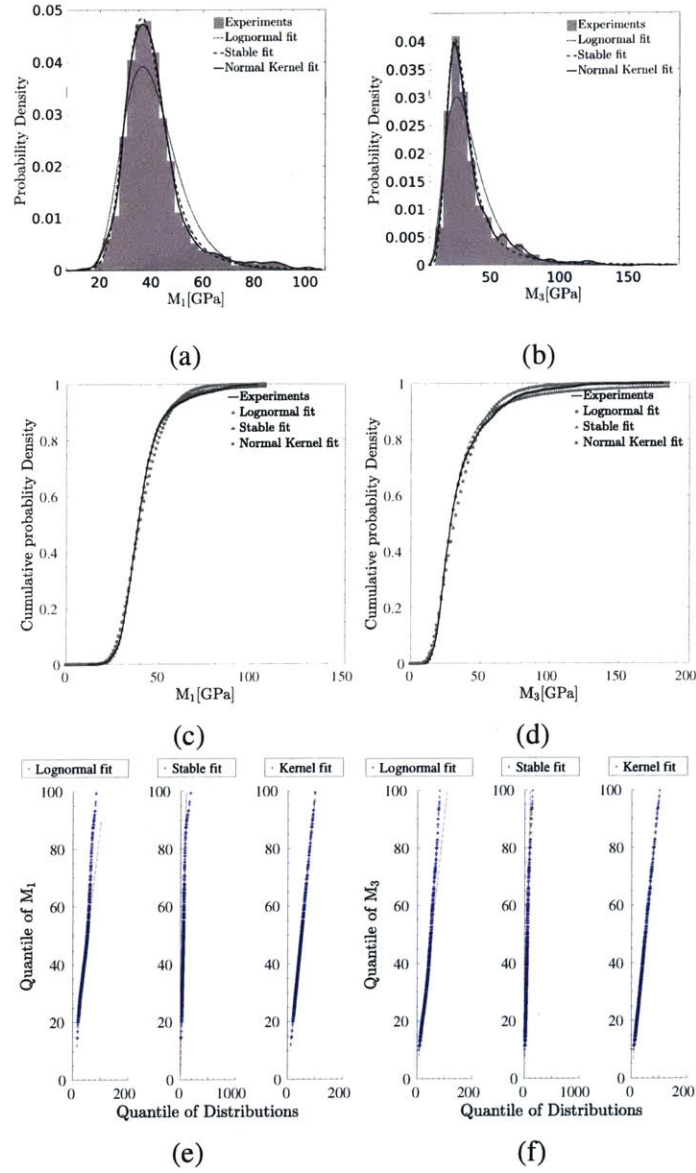


Figure 4-5: Probability density (4-5a and 4-5b), cumulative probability density (4-5c and 4-5d) and quantile-quantile plots (4-5e and 4-5f) for experimentally measured nanoindentation moduli for scan B with fitted Lognormal, Stable and non-parametric normal kernel distributions.

where  $\langle x \rangle$  and  $\langle x^2 \rangle$  represent the first two moments of a distribution, respectively. In general, the  $n^{th}$ -moment of a distribution can be defined as:

$$\langle x^n \rangle = \int p(x) x^n dx \quad (4.3)$$

with  $p(x)$  representing the probability density function (PDF) of random variable  $x$ .

As previously discussed, the segmentation of CT scans reduce all the solid constituents to three solid phases, including an organic phase. Due to abundance of interfaces in these organic/inorganic porous media and in order to account for the interfaces (and discontinuities) not captured given the resolution of the imaging instrument, all voxels are modeled as springs in series, similar to colloidal models for cement [84, 85]. For example in a simple one-dimensional case, this implies that for voxels  $i$  and  $j$  in phase  $a$ , the effective spring constant  $k_{eff}^a$  is defined as:

$$k_{eff}^a = \left( \frac{1}{k_i^a} + \frac{1}{k_j^a} \right)^{-1} \quad (4.4)$$

For simulations in LEM, the elasticity of each solid constituents are calibrated through the framework of effective interaction potentials [78], given a finite sized simulation box. At the interface of different phases, the mechanical interaction for node  $i$  in phase  $a$  and neighboring node  $j$  in phase  $b$  (and vice-versa), are modeled as follows:

$$int.\epsilon_{ij}^{(n,t)} = int.\epsilon_{ji}^{(n,t)} = 2 \left( \frac{1}{bulk\epsilon_{ij}^{(n,t)}} + \frac{1}{bulk\epsilon_{ji}^{(n,t)}} \right)^{-1} \quad (4.5)$$

where  $bulk\epsilon_{ij}^{(n,t)}$  and  $bulk\epsilon_{ji}^{(n,t)}$  denote the potential parameters calibrated to produce the desired elasticity of phases  $a$  and  $b$ , respectively while  $int.\epsilon_{ij}^{(n,t)} = int.\epsilon_{ji}^{(n,t)}$  quantify mechanical interaction at the interface of the two phases. The sensitivity of the results to this definition for the interfaces will be discussed later.

### 4.2.1 Input Elasticity of the Organic Phase

The organic phase is considered to be kerogen and to exhibit isotropic elastic behavior, fully characterized by two elastic moduli. Based on the molecular simulations of Bousige et al. [24] on reconstructed organic structures and multi-scale molecular informed micromechanics model of Monfared and Ulm [92],  $\nu_{ker.}^A = 0.25$  and  $M_{ker.}^A = 10.27$  GPa for scan A and  $\nu_{ker.}^B = 0.25$  and  $M_{ker.}^B = 2.24$  GPa for scan B are chosen as inputs.  $M$  refers to isotropic indentation modulus, defined as  $M = E / (1 - \nu^2)$ ,  $\nu$  denotes Poisson's ratio and  $E$  represents Young's modulus. The distinct elasticity of the kerogen phase for these two

samples is a consequence of their maturity level and their initial compositions.

## 4.2.2 Degrees of Freedom: Clay and Inclusion Effective Potentials

Since the CT data is oblivious to pore space below 64 nm, resolution of the CT data per voxel, and represent a length scale too coarse to account for the variations of clay mineral platelets and their orientations (see for e.g. [47]), the clay phase is modeled as a porous aggregate of clay particles effectively exhibiting a transversely isotropic elastic behavior. To fully capture this behavior, five elastic constants are needed. To this end, the values obtained through the inversion of ultra-sonic pulse velocity data through the multi-scale molecular informed micromechanics model of Monfared and Ulm [92] are considered, i.e.  $C_{11} = 103.0$  GPa,  $C_{12} = 41.6$  GPa,  $C_{13} = 34.1$  GPa,  $C_{33} = 43.3$  GPa and  $C_{44} = 7.7$  GPa. However, such transversely isotropic behavior can not be reproduced in LEM, in its current formulation, since it violates conditions outlined in Eqs. (2.31). Thus, clay is modeled as a quasi-transversely isotropic material in a reduced stiffness space. Specifically, only four elastic moduli, instead of five, are used for calibration of  $\epsilon_{ij}^{(n,t)}$  for the clay phase. The four elastic moduli are  $M_1$  and  $M_3$  as defined in Eqs. (3.31); as well as Voigt-Reuss-Hill averages for bulk,  $K_{VRH}$ , and shear,  $G_{VRH}$ , moduli [13] for a material exhibiting a hexagonal elastic symmetry which includes the transversely isotropic case. Thus, the following elastic constants describe the quasi-transversely isotropic behavior of the clay phase in this work:  $M_1 = 62.35$  GPa,  $M_3 = 29.25$  GPa,  $K_{VRH} = 46.81$  GPa, and  $G_{VRH} = 17.63$  GPa. Since voxels belonging to each phase are modeled as springs in series, the calibration of energy parameters are based on  $(M_1^*, M_3^*, G^*, K^*)$  where  $M_1^* = M_1/2$ ,  $M_3^* = M_3/2$ ,  $K^* = E^*/(3(1 - 2\nu))$  and  $G^* = E^*/(2(1 + \nu))$  where  $E^* = 0.5(M_1^* + M_3^*)(1 - \nu)$  and  $\nu = (3K_{VRH} - 2G_{VRH}) / (6K_{VRH} + 2G_{VRH})$ . It is well known that clay exhibits a range of elastic behaviors based on its type [4, 128, 69, 113, 69, 56]. Additionally, experimental observations of [14] using Transmission electron microscopy coupled with energy dispersive X-ray spectroscopy (TEM-EDX) hint at the spatial heterogeneity of clay particles even at nanometer length scales. To capture this, small fluctuations around the mean values of  $\epsilon_{ij}^{(n,t)}$  in the clay phase are introduced for all 1,000 sub-volumes during calibration. Specifically,

for the links in the plane of symmetry  $\vec{e}_1 \times \vec{e}_2$  [ $(\epsilon_1^n, \epsilon_1^t)$  for the 4 box-links of rest length  $l^0 = a_0$  oriented in the  $\vec{e}_1$ - and  $\vec{e}_2$ - directions, and  $(\epsilon_4^n, \epsilon_4^t)$  for the 4 in-plane diagonals of length  $\sqrt{2}a_0$ ; see Fig. 2-1 ] fluctuations around a mean value are modeled as a Gaussian distribution:

$$\epsilon_i^{(n,t)} \sim N(\bar{\epsilon}_i^{(n,t)}, S_1^2) \quad \forall i \in \{1, 4\} \quad (4.6)$$

where  $\bar{\epsilon}_i^{(n,t)}$  denotes the average value, calibrated based on the effective potential framework of Laubie et al. [78] and  $S_1^2$  represents the directionally-dependent variance, i.e. in  $\vec{e}_1$ , introduced as a degree of freedom to quantify spatial fluctuations in clay elasticity. Additionally, for the 2 box-links oriented in the  $\vec{e}_3$ -direction, i.e.  $\epsilon_3^n$ , spatial fluctuations are introduced similar to Eq. (4.6):

$$\epsilon_3^n \sim N(\bar{\epsilon}_3^n, S_3^2) \quad (4.7)$$

with  $S_3^2$  representing the directionally-dependent variance in  $\vec{e}_3$  while assuming distributions outlined in Eqs. (4.6) and (4.7) are independently distributed. In summary, two degrees of freedom,  $S_1^2$  and  $S_3^2$  are introduced to quantify the spatial heterogeneity of clay elasticity. Furthermore, the inclusions phase encompasses a variety of minerals with a range of elasticity. Fig. 4-6 displays pie-charts for the components of what is considered to be the inclusions phase based on XRD data [92]. Similar to the clay phase, the inclusions phase is modeled as a porous (sub-CT resolution) aggregate of polycrystals effectively exhibiting an isotropic elastic behavior. In order to capture the range of elasticity represented by this diverse group of minerals while maintaining the degrees of freedom at a minimum,  $\epsilon_{ij}^{(n,t)}$  for the inclusions phase can be written as:

$$\epsilon_{ij}^{(n,t)} = k_{ij}^{(n,t)} (l_{ij}^0)^2 = k \Gamma_{ij}^{(n,t)} (l_{ij}^0)^2 \quad (4.8)$$

where  $k$  is a directionally independent force constant and  $\Gamma_{ij}^{(n,t)}$  is a directionally dependent force constant pre-factor. Since  $\epsilon_{ij}^{(n,t)} \geq 0$  for instability reasons, a two-parameter univariate Weibull distribution [130, 131] characterized by a shape factor,  $\alpha \in \mathbb{R}_{>0}$ , and a scale factor,  $\beta \in \mathbb{R}_{>0}$ , is chosen to model the distribution of force constant  $k$  for sub-volume

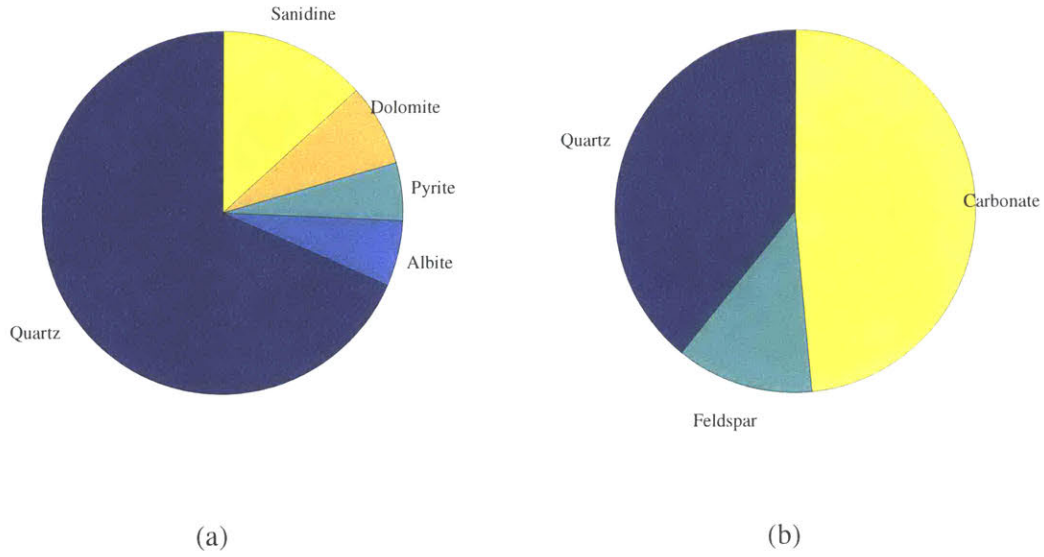


Figure 4-6: Mineralogical composition of the inclusions phase from XRD data as reported in [92] for scan A (4-6a) and scan B(4-6b).

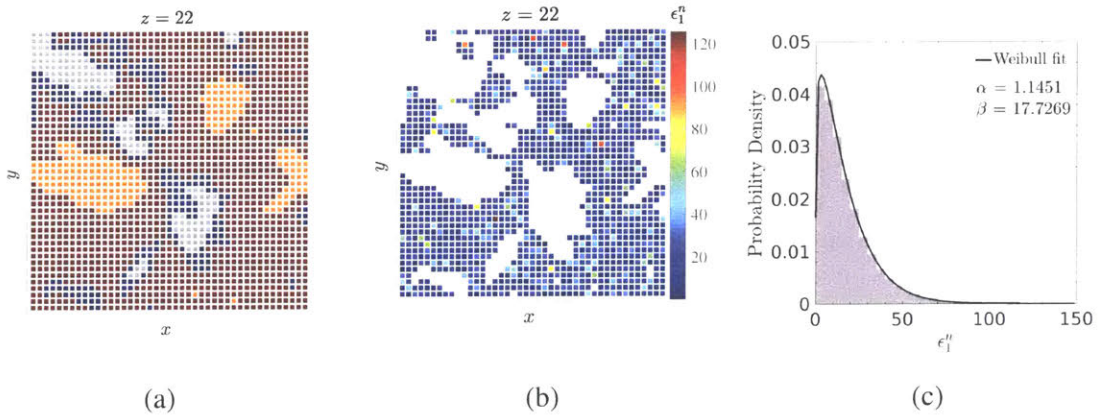


Figure 4-7: 4-7a: Cross-section of a discretized sub-volume extracted from CT scans. Colors Red, Orange, Blue and Gray correspond to inclusions, clay, pore and kerogen phases respectively.; 4-7b: Color map for  $\epsilon_1^n$  variations in the inclusions phase as shown in 4-7a ; 4-7c: Weibull distribution of  $\epsilon_1^n$  energy parameter, as an example, shown spatially in 4-7b.

$m$ :

$${}^m k \sim W(\alpha_m, \beta_m) \quad (4.9)$$

As an example, Fig. 4-7 illustrates the spatial distribution of  $\epsilon_1^n$  in a cross-section of one of the sub-volumes. In summary, each sub-volume used for calibration has two degrees of

freedom associated with the inclusions phase, while  $S_1^2$  and  $S_3^2$  degrees of freedom belong to the whole set of sub-volumes. Hence, with a calibration structure set of 1,000 sub-volumes, there are  $1,000 \times 2 + 2 = 2,002$  total degrees of freedom for each scan. For initial values and based on Fig. 4-6, scan A seems to be dominated by Quartz. Thus as initial guesses for its isotropic elasticity,  $K_{inc}^A = 37.90$  GPa and  $G_{inc}^A = 44.30$  GPa are chosen [86]. XRD data, as shown in Fig 4-6, suggests that the inclusions phase for scan B is dominated by Quartz and Calcite. As an initial guess, a Voigt-Reuss-Hill (VRH) average assuming each phase contributes with equal weights is employed. This translates into  $K_{inc}^B = 46.98$  GPa and shear modulus  $G_{inc}^B = 35.42$  GPa using elastic properties as reported in [86].

### 4.2.3 Numerical Optimization

The optimization was performed using NLOPT library [66] with Constrained Optimization By Linear Approximation (COBYLA) algorithm [101, 102] while utilizing Message Passing Interface (MPI) to simulate 1,000 sub-volumes at a time for calibration of each scan and for each iteration step of the optimization process. The objective function is defined as:

$$\min_d (1 - r) \quad (4.10)$$

where  $r$ , the correlation coefficient reads:

$$r = \frac{\sum_i^n (x_i - \langle x \rangle) (y_i - \langle y \rangle)}{\sqrt{\sum_i^n (x_i - \langle x \rangle)^2 \sum_i^n (y_i - \langle y \rangle)^2}} \quad (4.11)$$

where:

$$x = \{ \langle \text{sim. } M_1 \rangle_c, \langle \text{sim. } M_1^2 \rangle_c^{0.5}, \langle \text{sim. } M_3 \rangle_c, \langle \text{sim. } M_3^2 \rangle_c^{0.5} \} \quad (4.12)$$

$$y = \{ \langle \text{exp. } M_1 \rangle_c, \langle \text{exp. } M_1^2 \rangle_c^{0.5}, \langle \text{exp. } M_3 \rangle_c, \langle \text{exp. } M_3^2 \rangle_c^{0.5} \} \quad (4.13)$$

with  $d$  denoting the set containing degrees of freedom,  $d = \{ S_1^2, S_3^2, \{ \alpha_i \}, \{ \beta_i \} \}$  with  $|d| = 2,002$  given 1,000 sub-volumes from each scan employed for calibration.

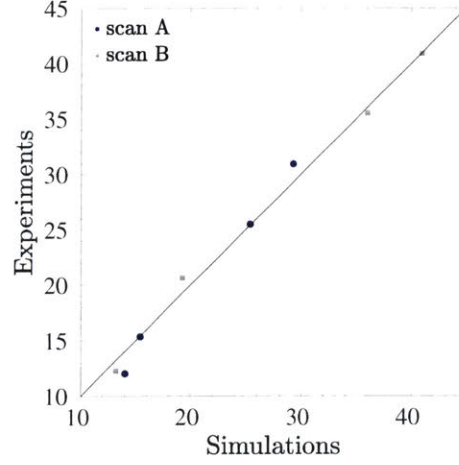


Figure 4-8: Optimized and experimentally measured  $\langle M_1 \rangle_c$ ,  $\langle M_1^2 \rangle_c^{0.5}$ ,  $\langle M_3 \rangle_c$  and  $\langle M_3^2 \rangle_c^{0.5}$  for scans A and B.

## 4.3 Results

### 4.3.1 Calibration & Validation Results

The first two cumulants of the distributions for calibrated indentation moduli for both scans as well as the corresponding cumulants based on experimentally measured distributions are summarized in Tab. 4.1. In addition, these values are plotted in Fig. 4-8 as a representation of the calibration quality with  $r = 0.991$  for scan A and  $r = 0.994$  for scan B. The probability density and cumulative probability density functions for the optimized shape factors,  $\{\alpha_i\}$ , and scale factors  $\{\beta_i\}$  for both scans A and B are displayed in Fig. 4-9. These parameters characterize the Weibull distributions for the energy parameters of the inclusions phase. Furthermore, for the clay phase in scan A,  ${}^A S_1^2 = 52.91 \text{ GPa}^2$  and  ${}^A S_3^2 = 50.48 \text{ GPa}^2$  and for scan B,  ${}^B S_1^2 = 15.16 \text{ GPa}^2$  and  ${}^B S_3^2 = 15.79 \text{ GPa}^2$  were obtained. In terms of elastic moduli, Fig. 4-10 displays the distributions for inclusions elasticity for both scans while the

Table 4.1: First and second cumulants of the distributions of indentation moduli of calibration structure set and experimentally measured.

	$\langle \text{exp. } M_1 \rangle_c$	$\langle \text{exp. } M_1^2 \rangle_c$	$\langle \text{exp. } M_3 \rangle_c$	$\langle \text{exp. } M_3^2 \rangle_c$	$\langle \text{sim. } M_1 \rangle_c$	$\langle \text{sim. } M_1^2 \rangle_c$	$\langle \text{sim. } M_3 \rangle_c$	$\langle \text{sim. } M_3^2 \rangle_c$
Scan A	30.933	144.816	25.483	235.540	29.271	197.354	36.020	372.159
Scan B	40.892	151.057	35.528	426.536	40.923	175.110	35.167	68.531

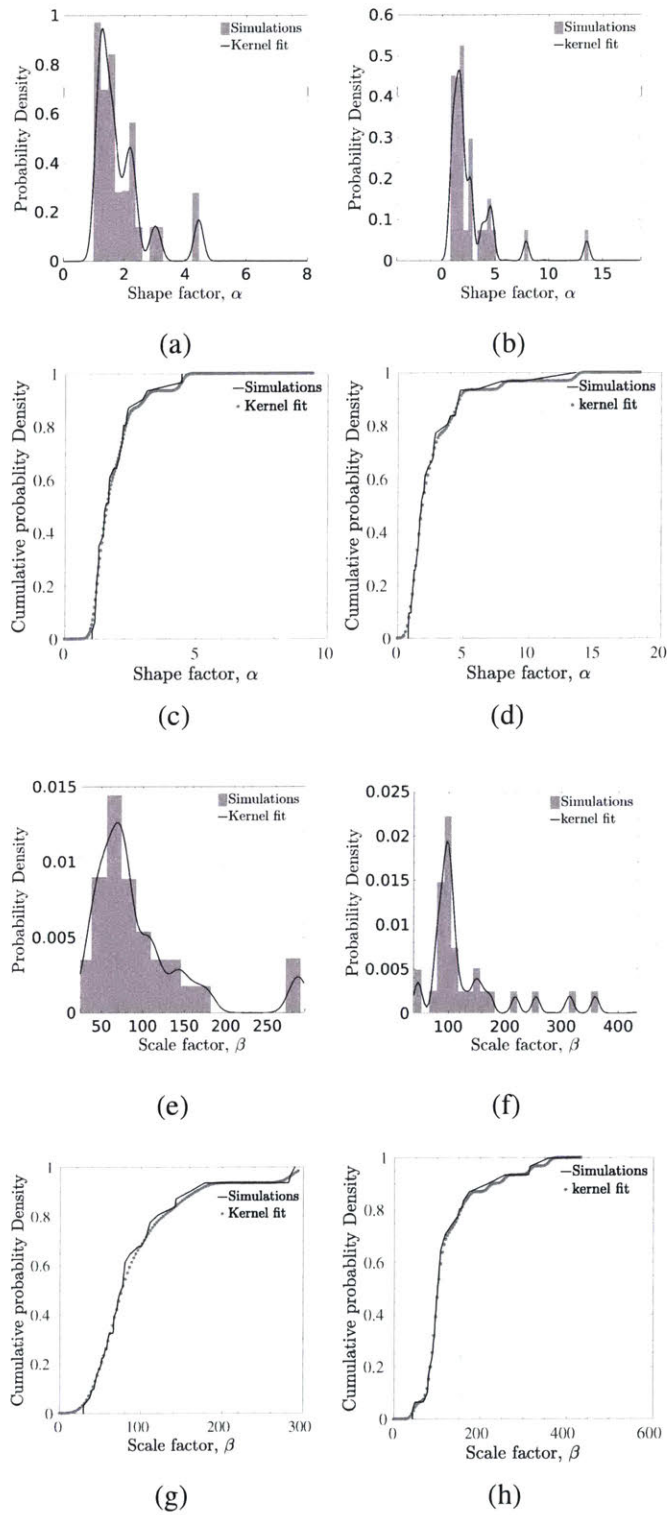


Figure 4-9: Probability density and cumulative probability density functions for optimized shape factors,  $\{\alpha_i\}$ , and scale factors,  $\{\beta_i\}$ , characterizing the Weibull distributions for the inclusions phase for scan A (4-9a,4-9c,4-9e and 4-9g) and scan B (4-9b,4-9d,4-9f and 4-9h).

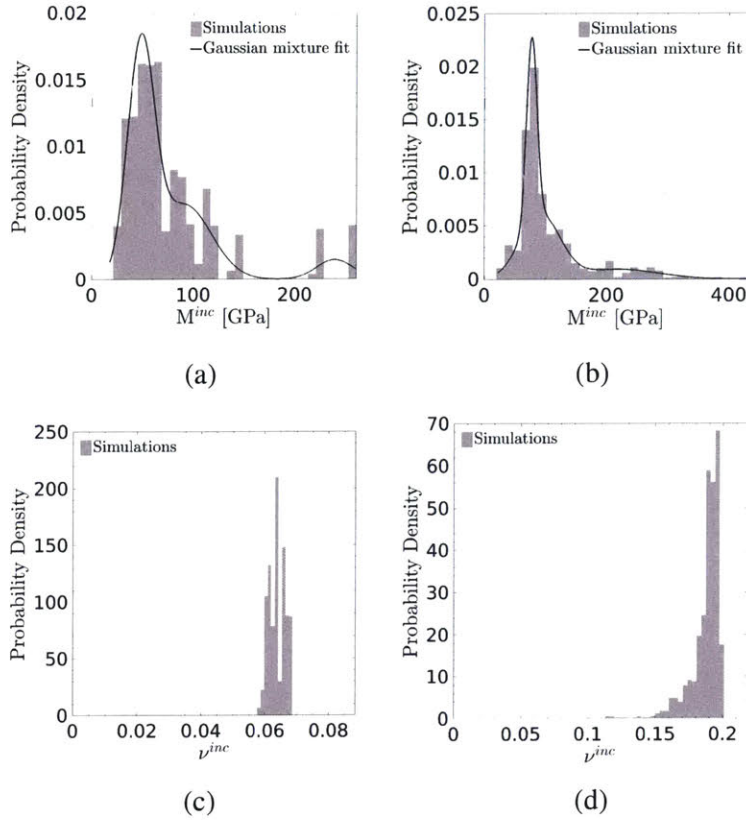


Figure 4-10: Distributions of calibrated isotropic elasticity ( $M^{inc}$ ,  $\nu^{inc}$ ) of the inclusions phase with three-components Gaussian-mixture model fits for  $M^{inc}$  for scan A (4-10a and 4-10c) and scan B (4-10b and 4-10d). See Tab. 4.2 for three-component Gaussian-mixture model fitting parameters.

three components Gaussian-mixture fit parameters for both cases are summarized in Tab. 4.2. Similarly, the small variations in elasticity of clay phase is shown in Fig. 4-11. To validate the results, the VSS is employed for each scan. The obtained distributions for  $\{\alpha_i\}$  and  $\{\beta_i\}$  (see Fig. 4-9) are employed to generate random numbers in a forward applications for simulating sub-volumes belonging to VSS of each scan. The resulting distributions are plotted in Fig 4-12 for scan A and Fig 4-13 for scan B and summarized in Tab. 4.3 in terms of first two cumulants. This provides independent means to validate the calibrated effective interaction potentials.

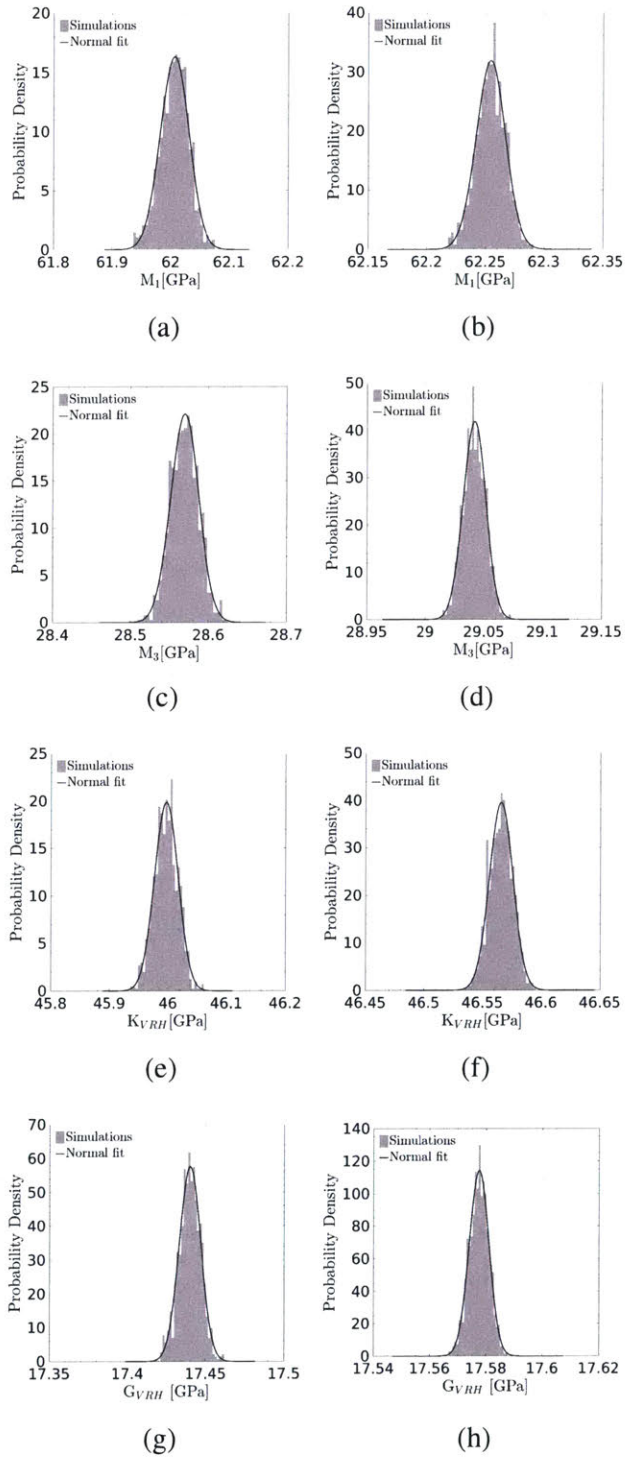


Figure 4-11: Distributions of calibrated quasi-transversely isotropic ( $M_1, M_3, K_{VRH}, G_{VRH}$ ) for the clay phase with normal fits for scan A (4-11a, 4-11c, 4-11e and 4-11g) and scan B (4-11b, 4-11d, 4-11f and 4-11h).

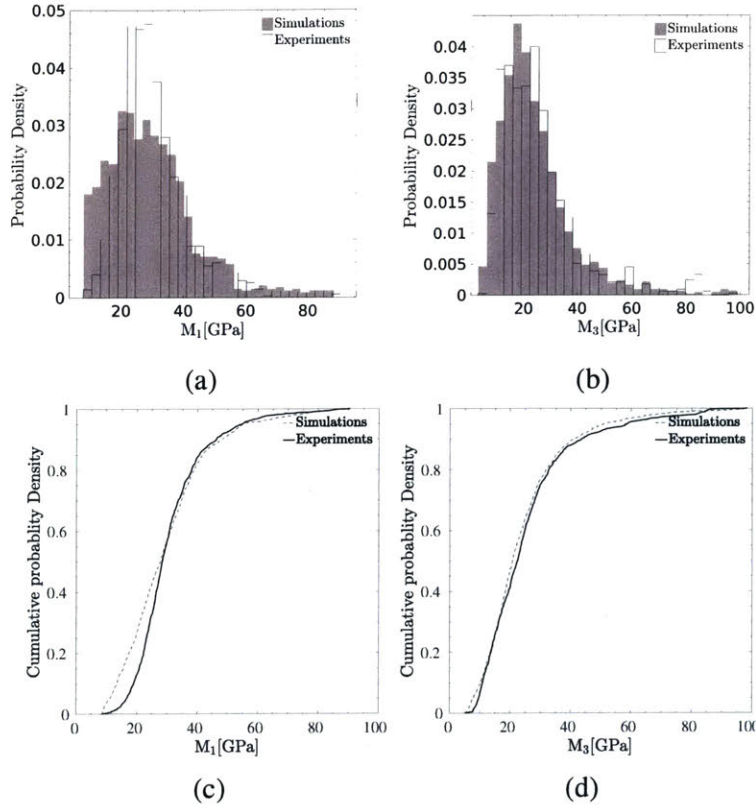


Figure 4-12: Probability density (4-12a and 4-12b) and cumulative probability density (4-12c and 4-12d) of scan A for simulated indentation moduli and experimentally measured nanoindentation moduli using validation structure set in a forward application for validation.

### 4.3.2 Biot Poroelastic Coefficients

Ensemble-based definitions for Biot poroelastic coefficients (see Chapter 2) are employed to simulate poroelastic response of these highly heterogeneous, porous solids given the calibrated effective interaction potentials of its solid constituents. To model the effect of pressure in the pore domain on the deformation behavior of the solid phase(s), the saturated drained case is considered. This case implies a hydrostatic stress state,  $\boldsymbol{\sigma} = -p\mathbf{1}$ , which can be simulated in the pore domain by imposing a central force ( $\vec{F}_i^j = F_i^{j,n}\vec{e}_n$ ) on each link associated with a node inside the pore domain through the Eq. (5.33). The interaction between pore fluid and solid mass points in the form of externally supplied work perturbs system's equilibrium which is resolved through the theory of minimum potential energy as a new equilibrium position is sought through energy minimization (see Chapters 2 and 3). The second-order tensor of Biot pore pressure coefficients,  $\mathbf{b}$ , is determined in the

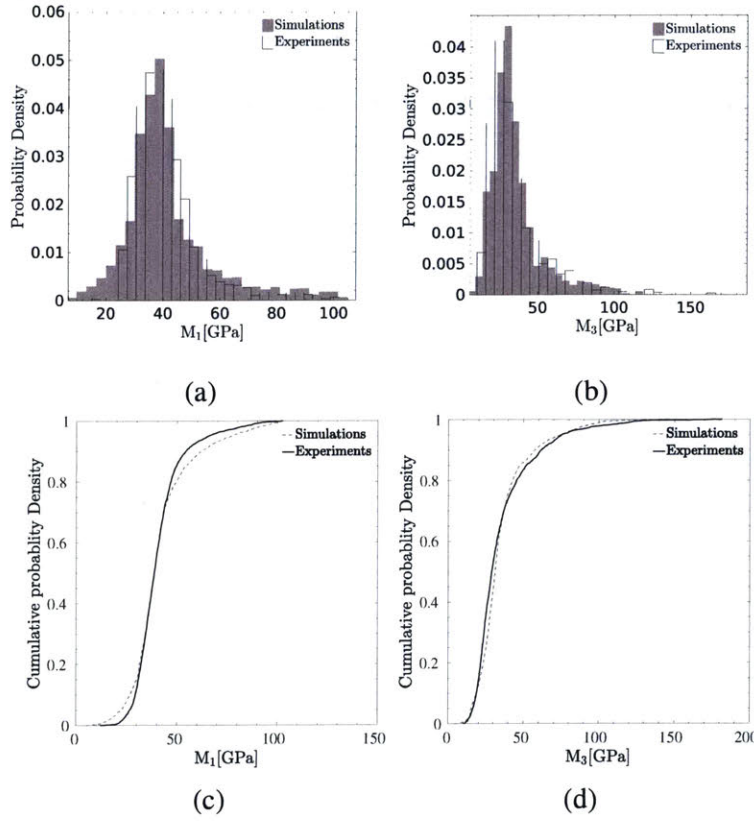


Figure 4-13: Probability density (4-13a and 4-13b) and cumulative probability density (4-13c and 4-13d) of scan B for simulated indentation moduli and experimentally measured nanoindentation moduli using validation structure set in a forward application for validation.

$\mu VT$ -ensemble at the composite scale (solid(s)+pore) utilizing Eq. (3.15). Furthermore, the The Biot solid modulus,  $N$ , can be simulated in the  $NPT$ -ensemble applied to the solid phase(s) while pressure  $p$  is applied to the entire solid boundary ( $\partial V_s$ ) utilizing Eq. (3.21). Since clay is modeled in the reduced stiffness space, application of Eq. 3.34 is challenged given its dependence on effective compliance tensor,  $\mathbb{S}$ . To circumvent this, for the case of small displacement and infinitesimal strains, the discrete mass points can be meshed into volumetric finite elements of known relative nodal displacements,  $\vec{\delta}_i = \vec{x}_i - \vec{X}_i$ , where  $\vec{x}_i$  and  $\vec{X}_i$  denote position vectors of mass point  $i$  in the reference and deformed configurations, respectively. For such an element the strains can be calculated using the classical linear finite element approach (see, for instance [8]):

$$\varepsilon_i = [B_{ij}] \left\{ \xi_j \right\} \quad (4.14)$$

where  $[B_{ij}]$  is the element's strain-displacement matrix,  $\{\xi_j\}$  is the vector of nodal displacements of the element, and  $\boldsymbol{\varepsilon}_i = \{\varepsilon_{11}, \varepsilon_{22}, \varepsilon_{33}, 2\varepsilon_{12}, 2\varepsilon_{23}, 2\varepsilon_{31}\}^T$  is a vector representation of the linearized strain tensor representative of the strain state in the solid element. The advantage of this approach is its focus on solid bulk deformation; which is required for the determination of the poroelastic properties using the strain compatibility condition, i.e.  $\text{tr}(\mathbf{E}) = (1 - \phi_0) \langle \text{tr}(\boldsymbol{\varepsilon}) \rangle_{V_s} + (\phi - \phi_0)$ . Thus, in the  $\mu VT$ -ensemble, an alternative access to the Biot modulus is obtained from:

$$(\phi - \phi_0)^{(\mu VT)} = - (1 - \phi_0) \langle \text{tr}(\boldsymbol{\varepsilon}) \rangle_{V_s} \quad (4.15)$$

$$\frac{1}{N} = \frac{1}{p} (\phi - \phi_0)^{(\mu VT)} \quad (4.16)$$

The simulated Biot pore-pressure coefficients for scan A is plotted in Fig. 4-14 and for scan B in Fig. 4-15. Biot solid moduli for both scans are plotted in Fig 4-16. Lastly, the first two cumulants for the distribution of Biot poroelastic coefficients are summarized in Tab. 4.4.

### 4.3.3 Interface Behavior Sensitivity Analysis

The sensitivity of effective behavior, specifically simulated indentation moduli, on interface behavior is assessed by varying the interface behavior, i.e. energy parameters for the bond element connecting nodes  $i$  and  $j$  that belong to two different phases. To this end, interface properties are varied from  $\min(\epsilon_{ij}^{(n,t)}, \epsilon_{ji}^{(n,t)})$  to  $\max(\epsilon_{ij}^{(n,t)}, \epsilon_{ji}^{(n,t)})$  with results for CSS of scan B shown in Fig. 4-17, along with simulation results for interface behavior as defined

Table 4.2: Three component Gaussian-mixture model fitting parameters for the isotropic indentation modulus,  $M$ , of the inclusion phase for scans A and B as shown in Fig. 4-10.  $\mu_i$  [GPa] denotes the mean of the  $i^{\text{th}}$ -component and  $w_i$  the associated weight.

	$w_1$	$\mu_1$	$w_2$	$\mu_2$	$w_3$	$\mu_3$
Scan A	0.56	48.17	0.06	239.77	0.38	91.15
Scan B	0.48	91.40	0.16	217.21	0.36	77.91

by Eq. (4.5). The results highlight the low sensitivity of the computed outcome in this paper to the defined interface behavior in Eq. (4.5).

### 4.3.4 Stress Transmission

Force flow and stress transmission through heterogeneous materials can provide a wealth of information regarding their microtexture (see for instance [103, 77, 80]). To explore this, first stress percolation in both scans due to an imposed uniaxial displacement (tension test) is studied. Then, for each scan, the local stresses are coarse-grained and their distributions plotted. Examining the response of coarse-grained stresses can be instrumental in determining the scale at which a representative elementary volume (rev) can be defined and thus continuum mechanics treatment can be applied. To achieve this, extracted sub-volumes are subjected to a uniaxial displacement while the simulation inputs are those obtained during calibration of effective interaction potentials of clay and inclusions phases. In addition, extracted sub-volumes of  $150 \times 150 \times 150$  voxels from each scan are characterized using the radial distribution function. The radial distribution function (only dependent on  $r = \|\vec{r}_1 - \vec{r}_2\|$ ) is used as an additional descriptor that carries information about position correlations in the system. It can be defined as:

$$g(r) = \frac{\rho(r)}{\rho^2} \quad (4.17)$$

where,  $\rho(r)$  is the local density while  $\rho$  is the average number density. The deviation of  $g(r)$  from unity provides information with regards to spatial correlation between the particles, with unity corresponding to no spatial correlation [125]. The radial distribution functions for each phase are displayed in Fig. 4-18. The radial distribution functions

Table 4.3: First and second cumulants of the distributions of indentation moduli of validation structure set and experimentally measured.

	$\langle^{exp.} M_1 \rangle_c$	$\langle^{exp.} M_1^2 \rangle_c$	$\langle^{exp.} M_3 \rangle_c$	$\langle^{exp.} M_3^2 \rangle_c$	$\langle^{sim.} M_1 \rangle_c$	$\langle^{sim.} M_1^2 \rangle_c$	$\langle^{sim.} M_3 \rangle_c$	$\langle^{sim.} M_3^2 \rangle_c$
Scan A	30.933	144.816	25.483	235.540	29.591	207.437	24.130	204.381
Scan B	40.892	151.057	35.528	426.536	41.761	246.700	35.317	311.076

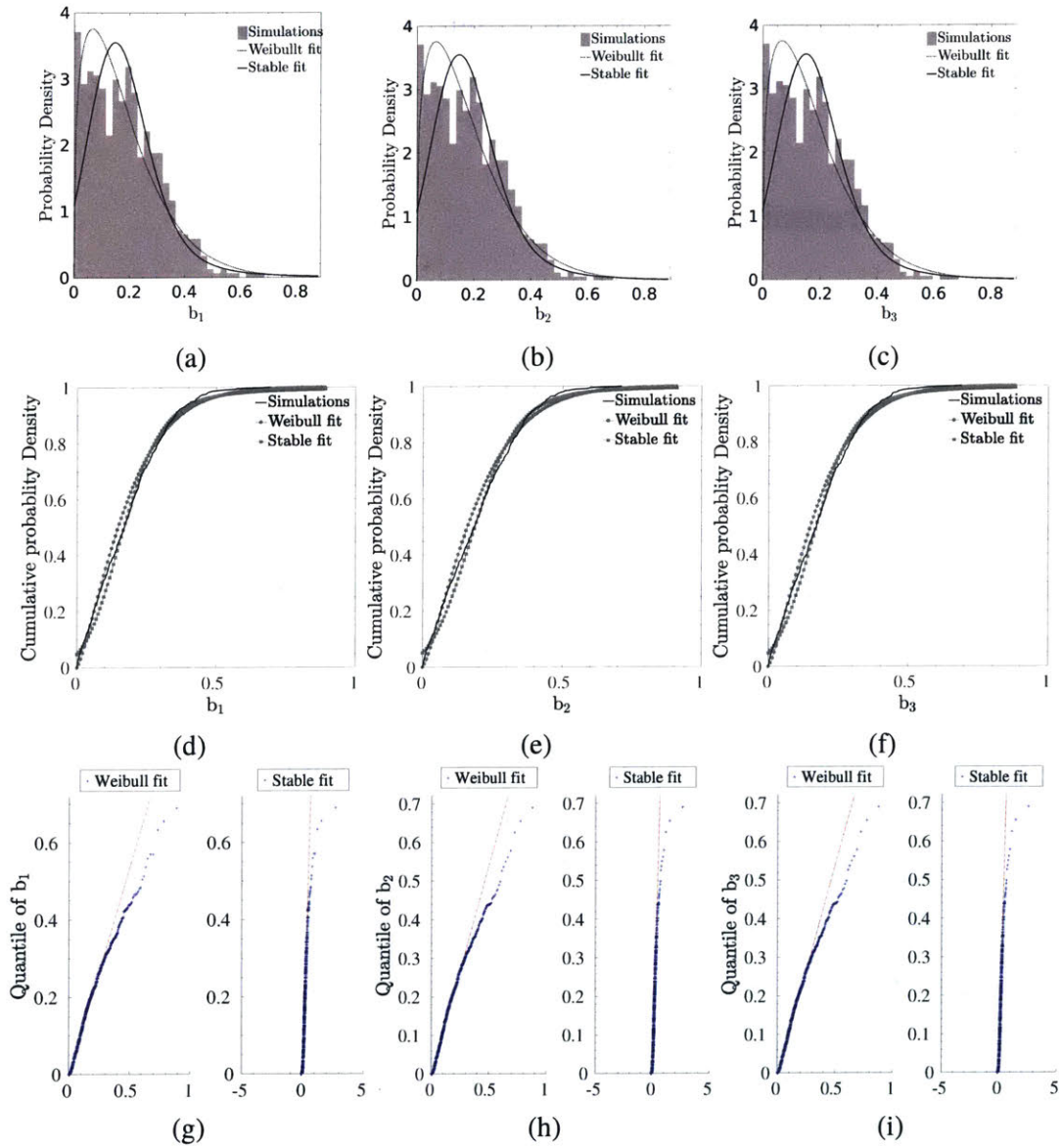


Figure 4-14: Probability density (4-14a, 4-14b and 4-14c), cumulative probability density (4-14d, 4-14e and 4-14f) and quantile-quantile plots (4-14g, 4-14h and 4-14i) for simulated Biot pore-pressure coefficients  $b_1$ ,  $b_2$ ,  $b_3$  for scan A with fitted Weibull and Stable distributions.

show a strong correlation between the clay and pore phases in scan A while for scan B, a strong correlation is observed between the inclusion and clay phases. Moreover, spatial distribution of clay phase in both scans are most correlated while spatial distribution of the inclusions and kerogen phases in both scans are least correlated.

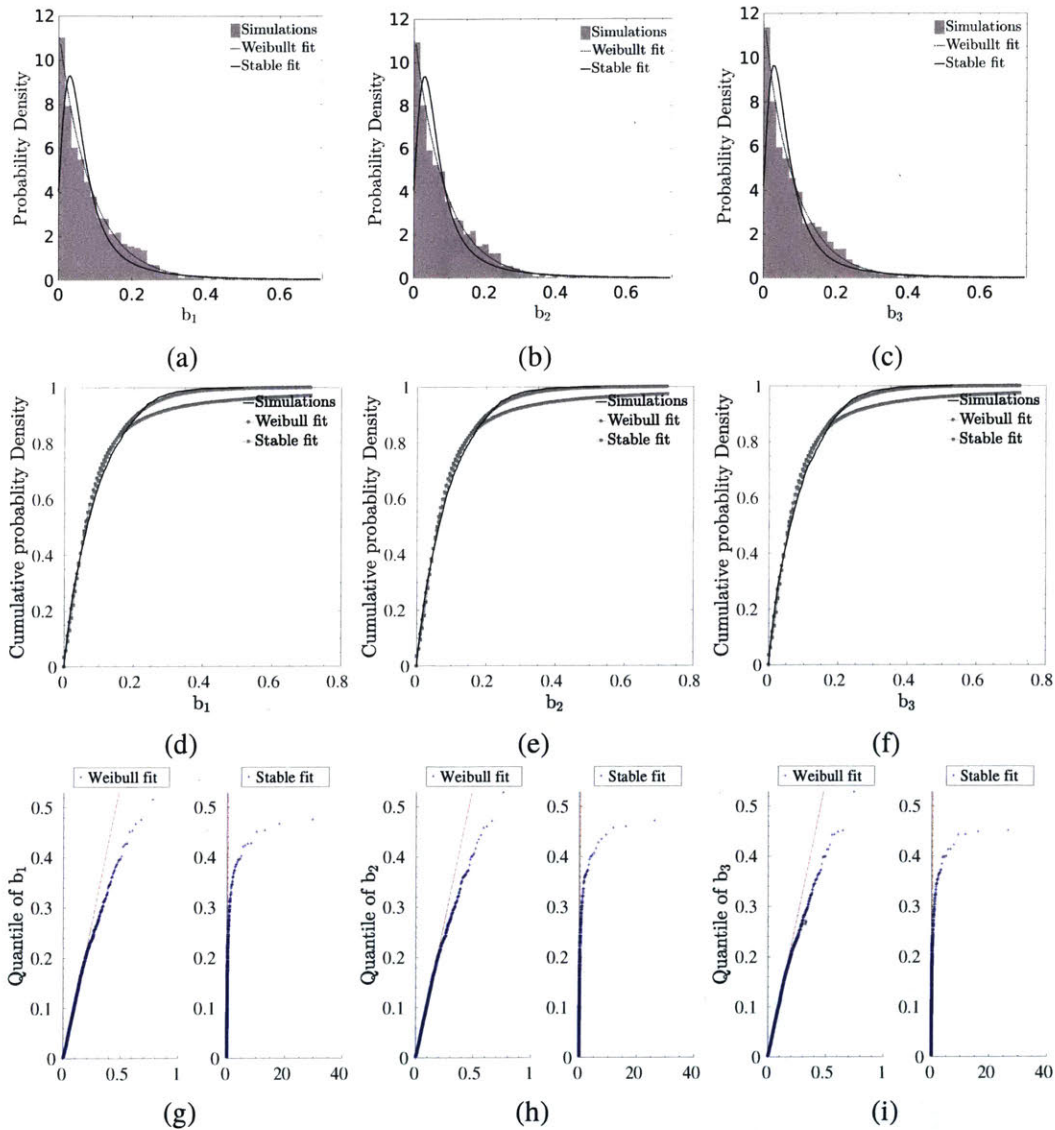


Figure 4-15: Probability density (4-15a, 4-15b and 4-15c), cumulative probability density (4-15d, 4-15e and 4-15f) and quantile-quantile plots (4-15g, 4-15h and 4-15i) for simulated Biot pore-pressure coefficients  $b_1$ ,  $b_2$ ,  $b_3$  for scan B with fitted Weibull and Stable distributions.

### Stress Percolation and Localization

The percolating stress is defined as the stress threshold at which stresses form a continuous path through the sample in the direction of the loading (displacement or traction). This can be found by thresholding the stress, starting from highest stress in the sample and continuously monitoring the localization of the stresses until a continuous path of stresses greater than or equal to the threshold is formed in the direction of the imposed loading. A

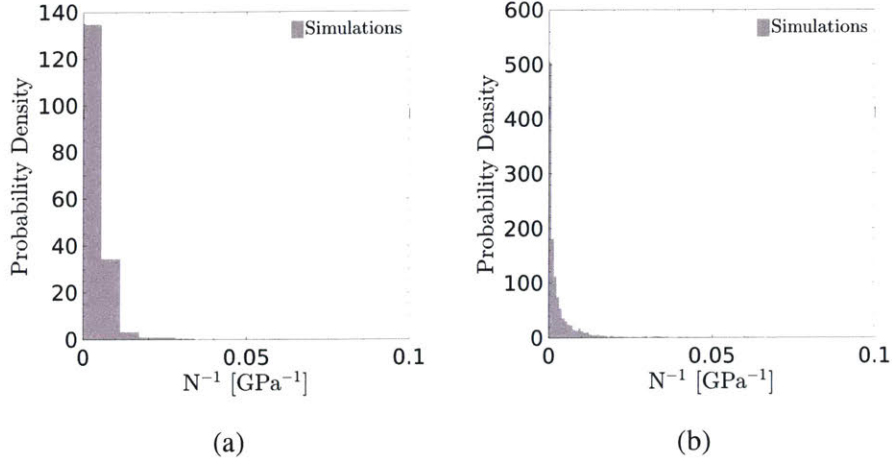


Figure 4-16: The distributions for Biot solid modulus for scan A (4-16a) and scan B (4-16b).

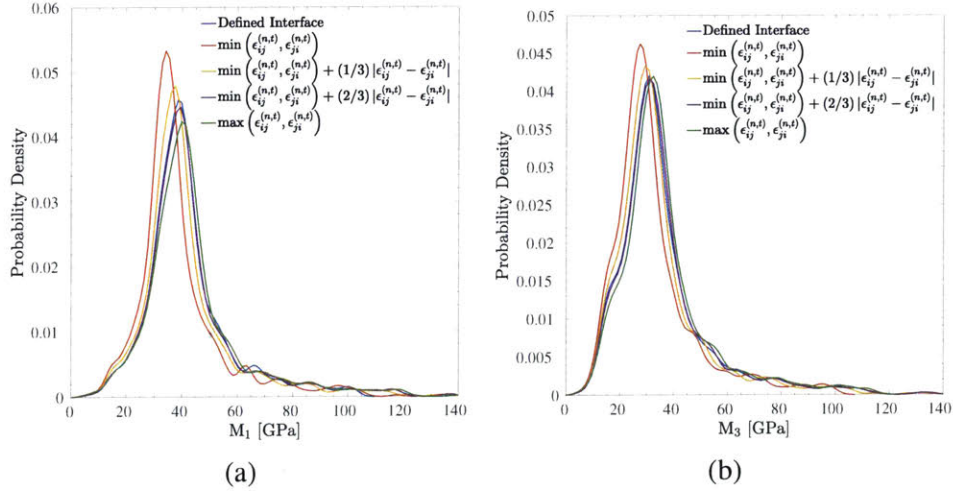


Figure 4-17: Distributions for simulated indentation moduli,  $M_1$  as shown in 4-17a and  $M_3$  as shown in 4-17b, for different interface models.

continuous path is defined as such that each voxel satisfying the stress thresholding criteria has a neighboring voxel, based on 26-connectivity, that also meets the stress threshold,  $\sigma^{th}$ . Sub-volumes of  $150 \times 150 \times 150$  voxels are extracted from each scan. A uniaxial

Table 4.4: First and second cumulants of the distributions for Biot poroelastic coefficients.

	$\langle b_1 \rangle_c$	$\langle b_1^2 \rangle_c$	$\langle b_2 \rangle_c$	$\langle b_2^2 \rangle_c$	$\langle b_3 \rangle_c$	$\langle b_3^2 \rangle_c$	$\langle N^{-1} \rangle_c$	$\langle (N^{-1})^2 \rangle_c$
Scan A	0.182	0.016	0.198	0.019	0.182	0.016	0.0062	0.0019
Scan B	0.089	0.007	0.087	0.007	0.085	0.006	0.0043	$8.9659 \times 10^{-5}$

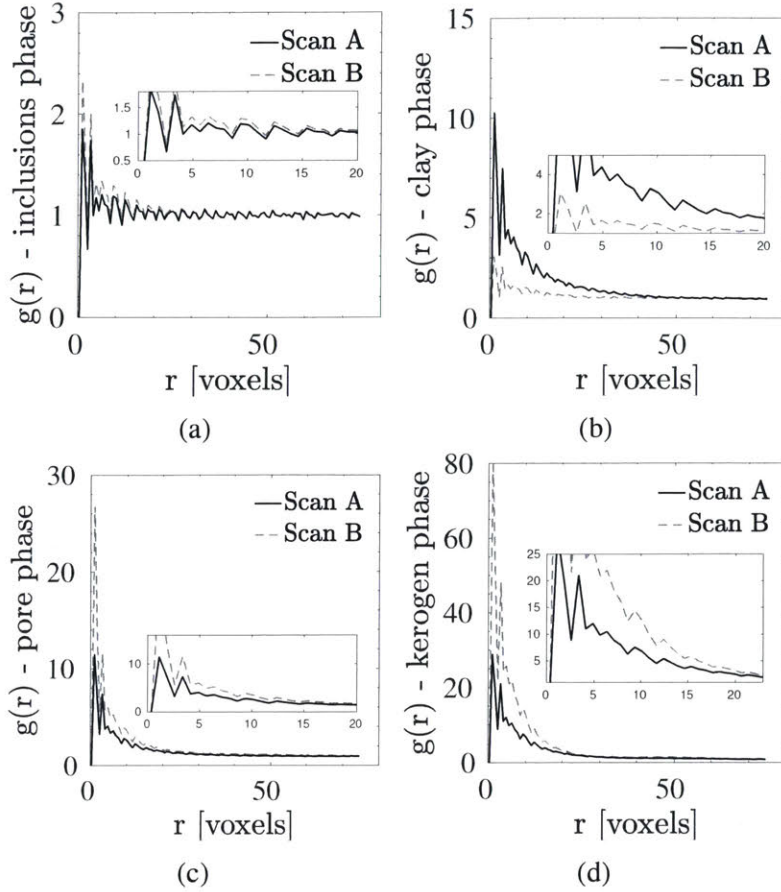


Figure 4-18: Pair-correlation function for clay, pore, kerogen and inclusions phases corresponding to sub-volumes of size  $150 \times 150 \times 150$  voxels.

displacement in the form of  $\vec{\xi}^d = \xi^d \vec{e}_i$  for  $i \in \{1, 2, 3\}$  is imposed on the extracted sub-volumes and for five realizations of the obtained Weibull distributions for the inclusions effective interaction potentials. As an example, percolation path for one of the realizations is shown in Fig. 4-19. A quantity of interest, highlighting the underlying microtextural features of a highly heterogeneous media, is the ratio of average stresses in the direction of imposed load to the stress threshold. For the cases examined, this ratio is summarized in Tab. 4.5. In addition, the radial distribution function for stresses greater than the percolating stress, for all five realizations for clay and inclusions phases' elasticity, are shown in Fig. 4-20. The results highlight the important role of local stiffness variations on percolating stress paths with the  $\vec{e}_1$  direction (parallel to the bedding planes) in scan A least affected and the  $\vec{e}_3$  direction (perpendicular to the bedding planes) in scan B most affected by such variations.

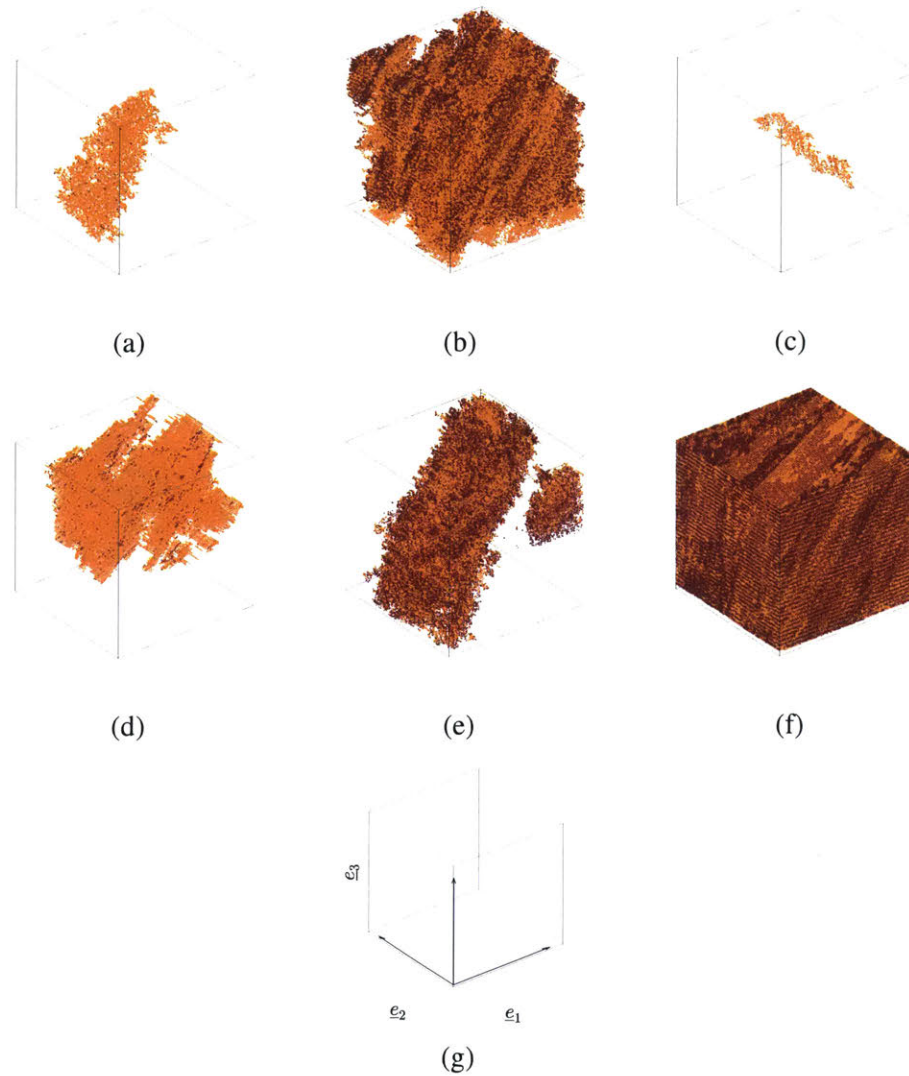


Figure 4-19: Percolating stress path in  $\vec{e}_1$  and for scan A (4-19a), for scan B (4-19b), in  $\vec{e}_2$  and for scan A (4-19c) and scan B (4-19d), in  $\vec{e}_3$  and for scan A (4-19e) and scan B (4-19f). Colors Red and Orange indicate inclusions and clay phases, respectively. 4-19g defines the coordinate system.

### Stress Coarse-Graining

Sub-volumes of size  $300 \times 300 \times 300$  voxels are extracted for both scans and subjected to a uniaxial displacement of the form  $\vec{\xi}^d = \xi^d \vec{e}_i$  for  $i \in \{1, 2, 3\}$  and for five realizations of the obtained Weibull distributions for the inclusions effective interaction potentials. The local stresses are coarse-grained by averaging them over sub-volumes of increasing length,  $\lambda/a_0 (= 1)$  while applying a periodic boundary condition. The resulting distributions plotted for different coarse-graining length scale,  $\lambda/a_0 (= 1)$  are shown in Figs. 4-21 and 4-22,

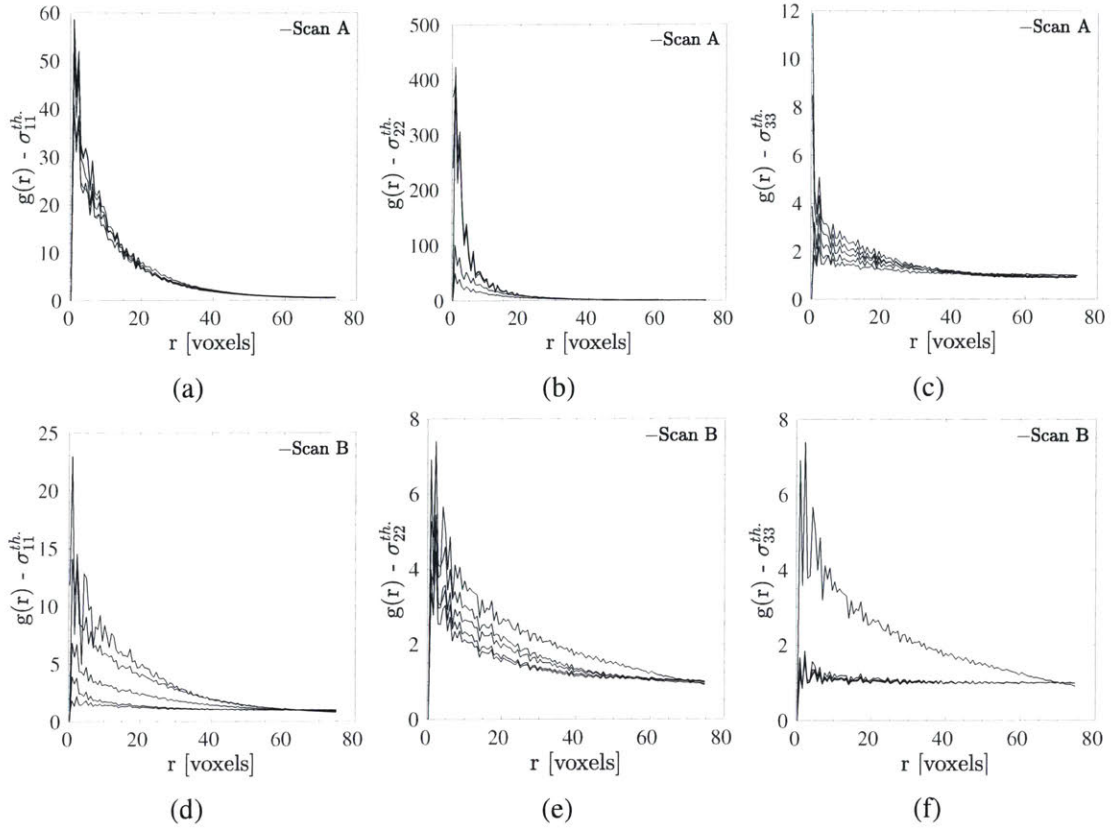


Figure 4-20: Radial distribution function for the percolated stress path due to imposed uniaxial displacement in different directions for scan A (4-20a, 4-20b, 4-20c) and scan B (4-20d, 4-20e, 4-20f).

for scans A and B respectively. The length scale dependency of these PDFs provides the means to identify the scale at which a representative elementary volume (rev) for these highly heterogeneous media can be defined. For  $\lambda > 50$ , the number of coarse-grained samples falls below 200 and thus excluded for statistical analysis. For  $\lambda = 50$ , representing 216 samples, both scans display multi-modal behaviors though with significantly less noise compared to the cases for  $\lambda < 50$ . Such multi-modal behavior is a reflection of existence of competing load bearing phases at this coarse-graining length scale. Additionally, the

Table 4.5: Ratio of mean stresses to stress threshold for a given direction of applied load.

	$\langle \sigma_{11} \rangle / \sigma_{11}^{th.}$	$\langle \sigma_{22} \rangle / \sigma_{22}^{th.}$	$\langle \sigma_{33} \rangle / \sigma_{33}^{th.}$
Scan A	2.88-3.87	3.54-4.51	2.78-3.13
Scan B	1.28-1.69	1.34-1.53	0.93-1.16

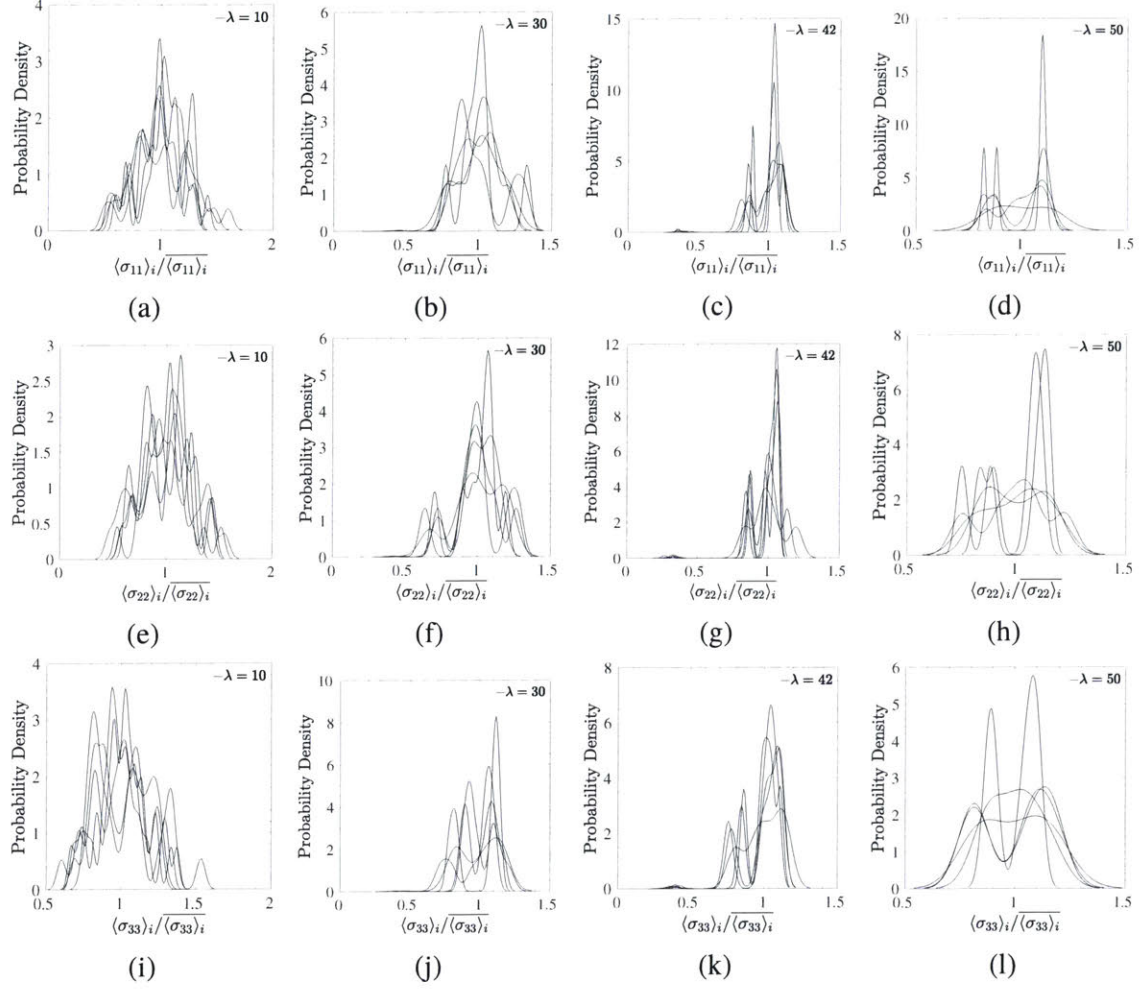


Figure 4-21: Coarse-grained stresses for different  $\lambda$  for scan A with five realizations for inclusions stiffness, labeled as cases A – E. 4-21a, 4-21b, 4-21c, 4-21d correspond to coarse-grained stresses,  $\sigma_{11}$  due to  $\vec{\xi}^d = \xi^d \vec{e}_1$ ; 4-21e, 4-21f, 4-21g, 4-21h correspond to coarse-grained stresses,  $\sigma_{22}$  due to  $\vec{\xi}^d = \xi^d \vec{e}_2$  and 4-21i, 4-21j, 4-21k, 4-21l correspond to coarse-grained stresses,  $\sigma_{33}$  due to  $\vec{\xi}^d = \xi^d \vec{e}_3$ .

dependency of the results on different stiffness realizations should be noted. For example for  $\lambda = 50$ , both multi-modal and bi-modal behaviors can be observed.

## 4.4 Discussions

It is shown that capturing the heavy-tailed distributions of experimentally measured indentation moduli requires introducing spatial fluctuations in the effective interaction potential of the inclusions and clay phases. For the inclusions phase, this is achieved by modeling these

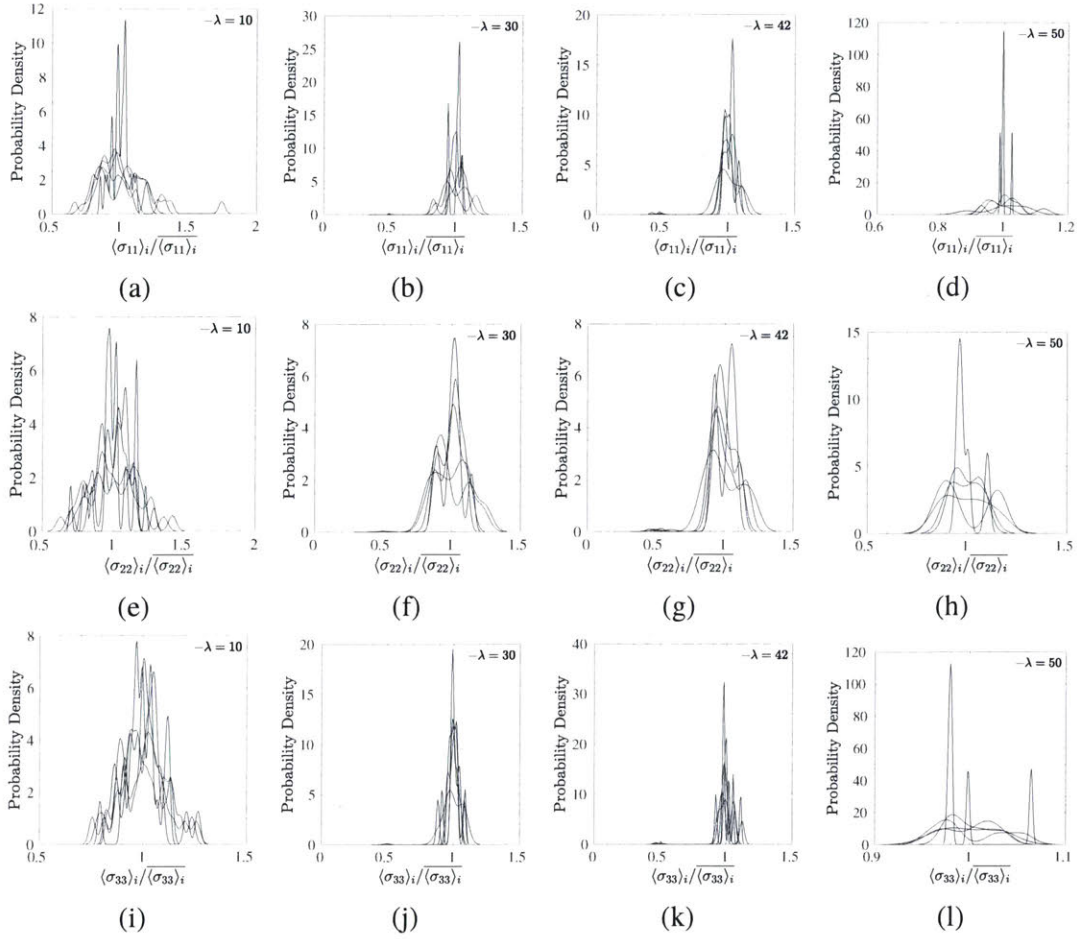


Figure 4-22: Coarse-grained stresses for different  $\lambda$  for scan B with five realizations for inclusions stiffness, label as cases A – E. 4-22a, 4-22b, 4-22c, 4-22d correspond to coarse-grained stresses,  $\sigma_{11}$  due to  $\vec{\xi}^d = \xi^d \vec{e}_1$ ; 4-22e, 4-22f, 4-22g, 4-22h correspond to coarse-grained stresses,  $\sigma_{22}$  due to  $\vec{\xi}^d = \xi^d \vec{e}_2$  and 4-22i, 4-22j, 4-22k, 4-22l correspond to coarse-grained stresses,  $\sigma_{33}$  due to  $\vec{\xi}^d = \xi^d \vec{e}_3$ .

spatial variations with a continuous univariate Weibull distribution while for the clay phase, small spatially-dependent fluctuations are introduced following Gaussian distributions. The PDFs for calibrated elasticity of the inclusions phases for each scan, as shown in Fig. 4-10, reflect the range of elasticity represented by the diverse group of the inorganic minerals (see Fig. 4-6 for compositional pie-charts) considered to be part of the inclusions phase. This is evident by the multi-modal nature of these PDFs. The fitted three-component Gaussian mixture model parameters, as outlined in Tab. 4.2, reflect the composition of the inclusions phase as displayed in Fig. 4-6. With a focus on isotropic indentation modulus, the typical elasticity values reported in literature (see for e.g. [86]) are  $M^{Quartz} = 95.28$  GPa,  $M^{Albite} \approx$

$M^{Feldspar} = 78.51$  GPa,  $M^{Pyrite} = 313.30$  GPa,  $M^{Calcite} = 93.91$  GPa and  $M^{Dolomite} = 127.71$  GPa which are very comparable to values reported in Tab. 4.2. This convergence of XRD data and calibrated effective interaction potential of inclusions phase from lab measured nanoindentation moduli highlights the utility of modeling spatial fluctuations of inclusion elasticity using a two parameter Weibull model. The small range of obtained Poisson's ratio can be attributed to maintain a constant ratio between  $\epsilon_i^{(n,t)}$  in different directions, as outlined in Eq. (4.8). Relaxing this condition would result into higher spatial fluctuations in Poisson's ratio while increasing the degrees of freedom associated with the calibration procedure. Furthermore, additional refinements can be considered in the future by introducing multi-variate continuous random variables with spatial correlations (see for e.g. [129]). The local variations of mechanical properties, spatially and within a phase, is observed experimentally in a range of materials with some studies attributing enhanced mechanical behavior to such spatial variations [121, 133, 43] while more recently highlighting the role of stiffness heterogeneity in cell mechanics [12].

The experimentally measured indentation moduli can be modeled by both Lognormal and Stable distributions as shown in Figs. 4-4 and 4-5. The quantile-quantile plots suggest Stable distribution to be a slightly better model to fit the data given the deviations at the distribution tails from the models. In fact, it is well-known that Stable distributions arise from interaction of very wide-PDFs [68], in this case a manifestation of the highly heterogeneous nature of organic-rich shales even at very small length scales (see for e.g. [2] ) from the generalized central limit theorem [53]. This observation can also be extended to the simulated effective Biot pore-pressure coefficients, as shown in Figs. 4-14 and 4-15, with the simulated data captured well with Weibull and Stable distributions, except for the heavy-tails. The simulated Biot solid moduli do not follow any parameteric distributions and thus only the simulated results are shown as PDFs in Fig. 4-16 for both scans. Notable from these PDFs, simulated Biot solid moduli for scan B cover a wider range compared to scan A. The first two cumulants of the simulated Biot poroelastic coefficients are summarized in Tab. 4.4. The first cumulants suggest no significant anisotropy given the length scale associated with simulated sub-volumes. It should be noted that, on average, the Biot

poroelastic coefficients of scan A are two times greater than that of scan B. This is partly due to scan A having a higher porosity, on average, compared to scan B as shown in Figs. 4-2 and 4-3.

The distribution of stresses as a result of an imposed uniaxial displacement was also studied. It was shown that stresses percolated at a higher threshold in scan A compared to scan B as summarized in Tab. 4.5. The percolation path as shown in Fig. 4-19 points at the underlying microtextural differences in transmitting the load. For scan A, the percolating path consists of what seems to be elongated grains, mostly in the clay phase, while for scan B, the load bearing path seems more granular, spatially dispersed and consisted of both inclusions and clay phases. This is further quantified using  $g(r)$  of the percolating path as shown in Fig. 4-20. One general observation consistent with Fig. 4-20 indicates short-range nature of percolating stresses in scan A compared to long-ranged one for scan B. However, the results vary based on different realizations of spatial stiffness. These results are also consistent with earlier continuum mechanics-based homogenization approaches, and indeed the backbone of the molecular informed microporoelastic model of [92] where a self-consistent homogenization scheme is used to model mature systems, for e.g. scan B, implying an effective granular texture while for immature systems, for e.g. scan A, a Mori-Tanaka homogenization scheme, implying a matrix-inclusion effective texture is employed. Furthermore, coarse-grained stresses, as shown in Figs. 4-21 and 4-22, suggest that at a coarse-graining length scale of  $\lambda = 50$  less noisy, multi-modal response emerges highlighting the competition between different load bearing phases.

In the future, calibration based on higher order cumulants can be considered for refinement of the results while relaxing conditions on for e.g. constant ratio of  $\epsilon_{ij}^{(n,t)}$  as discussed before. This would also require overcoming limitations of LEM in its current formulation in capturing the range of transversely isotropic behavior (see Eq. (2.31)) and isotropic behavior beyond  $\nu = 0.25$  by examining comparable methods that have addressed such restrictions such as peridynamics [114] and elastic networks [95].

## 4.5 Chapter Summary

Utilizing advancements in high-performance computing and imaging techniques, a methodology to calibrate and to validate effective interaction potentials of the solid constituents of a highly heterogeneous porous solid is presented. The spatial variations of elasticity are shown to be necessary ingredients for capturing heavy-tails of measured indentation data. The measured indentation data and simulated effective poroelastic pore-pressure coefficients generally seem to follow a Stable distribution, a manifestation of interactions of wide underlying PDFs. Stress transmission highlights the distinct percolation paths in each scan due to underlying microtextural features while stress coarse-graining delineates the highly heterogeneous nature of the materials examined and the challenges involved in defining a representative elementary volume for continuum based analysis. The proposed framework provides new insights into the interplay of texture and effective behavior of real materials while paving the way for designing durable and sustainable materials with imposed effective mechanical behavior.

# Chapter 5

## Temperature Dependent Capillary Pressure Fields in Disordered Confinement

### 5.1 Introduction

The behavior of a bulk fluid contrasts significantly with that of a confined fluid. This is a consequence of pore topology (pore connectivity in space), pore morphology (pore shape) and the strength of fluid-solid interactions that alter the energy landscape of a fluid. The temperature dependent confined fluid behavior interests many in physics and mechanics communities. The role of confinement on fluid criticality and the nature of capillary condensation as a phase transition is yet to be fully resolved. Gaining insights into phase transition and fluid criticality can contribute to a range of applications including heterogeneous catalysis, adsorption, chromatography, energy, environment, earth and materials sciences [31, 32, 98, 33]. The behavior of wet granular materials is an active area of research (see for e.g. [19, 50, 9]). Part of the challenge for investigating the behavior of wet granular materials lies in the complex texturing of liquid in a disordered porous structure. This includes the formation, growth and coalescence of liquid clusters in granular systems [108, 42, 88]. A fortified understanding of wet granular media will significantly

affect a range of applications from slope stability by vegetation to industrial wet mixing in powder agglomeration [42]. In the context of unsaturated poromechanics (see for e.g. [36, 29, 37, 22]), one needs to resolve fluid-solid interactions at the pore scale and to translate that information into mechanical work with pressure-volume as (thermodynamic) conjugate coordinates [16, 106] and/or surface tension-area in case of a thin-film formation for e.g. during adsorption [127, 25] or chemical work with chemical potential-particle concentration as its conjugate coordinates [36, 5]. Thus, approaching unsaturated poromechanics requires bringing together a description for solid(s) that can account for heterogeneities and anisotropy as well as a fluid description that honors the effects of confinement, temperature and the strength of fluid-solid interactions.

With these questions in mind, we study capillary condensation in disordered granular packings. This is done through implementation of coarse-grained lattice gas density functional theory [70, 71] that accounts for topological confinement, temperature dependent fluid behavior as well as the strength of fluid-fluid and fluid-solid interactions. In this statistical mechanics approach, the fluid is modeled in the grand canonical ensemble by imposing chemical potential  $\mu$ , volume  $V$  and temperature  $T$ . Furthermore, Zhou et al. [137] have shown that in the continuum limit and with correct parametrization, the coarse-grained lattice gas model approaches the Cahn-Hilliard model [27]. This paves the way to model the gas-liquid interface diffusively while providing access to capillary stresses  $\sigma_f(\vec{x})$  as a tensorial field in the pore domain via Kortweg stress definition [72, 6]. In turn, this enables us to study the effects of confinement (disordered particle packing) and temperature on the capillary pressure field. At the same time, access to a normalized fluid density scalar field, i.e.  $\rho(\vec{x})$  during condensation provides a pathway to study the formation and coalescence of liquid clusters for such disordered packings. With regards to mechanics, a local pore pressure force formulation slightly modified from [91] (see Chapter 3) is proposed to capture local pressure values in the pore space. This provides the means to study unsaturated poromechanics of heterogeneous porous continua utilizing a discrete heterogeneous solid description in Lattice Element Method [78] (see Chapter 2).

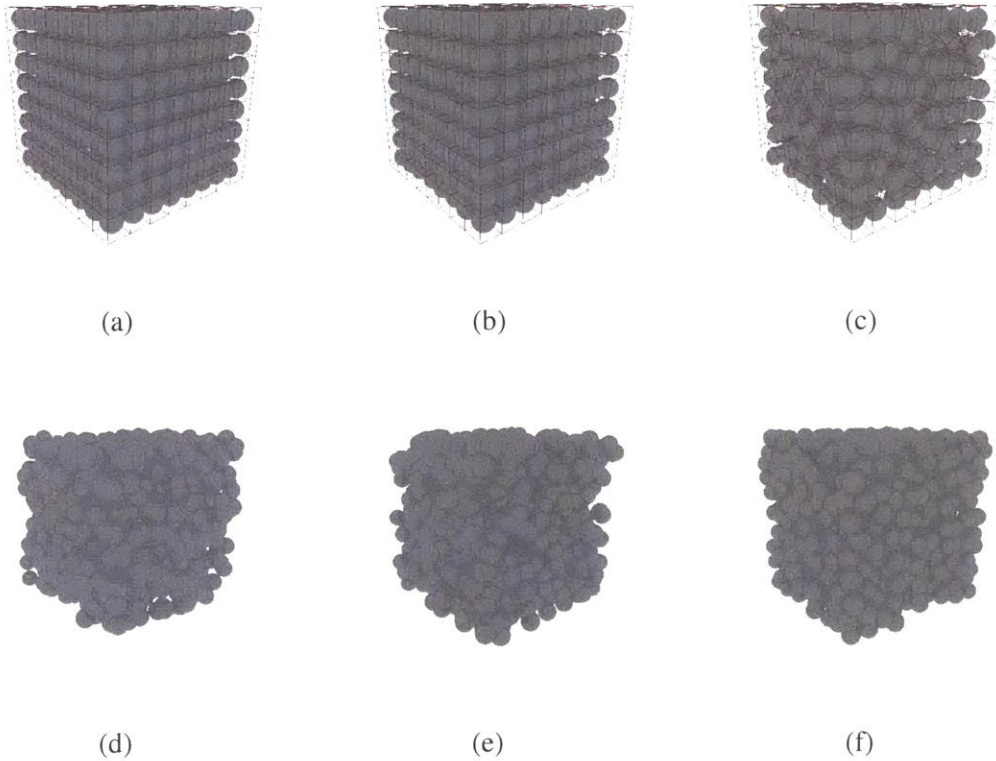


Figure 5-1: Type A structures -  $\lambda^A = 1.064$  (5-1a),  $\lambda^A = 1.021$  (5-1b),  $\lambda^A = 1.0$  (5-1c) and Type B structures -  $\lambda^B = 0.2$  (5-1d),  $\lambda^B = 0.5$  (5-1e) and  $\lambda^B = 1.0$  (5-1f). The voronoi cell tessellations were created using Voropp [107].

## 5.2 Materials & Methods

To explore the effects of confinement on capillary pressure field, pore fluid criticality and liquid-gas phase transition, a number of porous structures are created. More specifically, overlapping and non-overlapping monodisperse granular packings in three-dimensional space (3D) are considered with the intent of creating locally varying confinement through introducing spatial disorder in particle positions.

### 5.2.1 Monodisperse Particle Packings

There are two types of monodisperse granular packings that are utilized for this investigation:

Type A - Non-overlapping (hard) monodisperse particles: The reference configuration con-

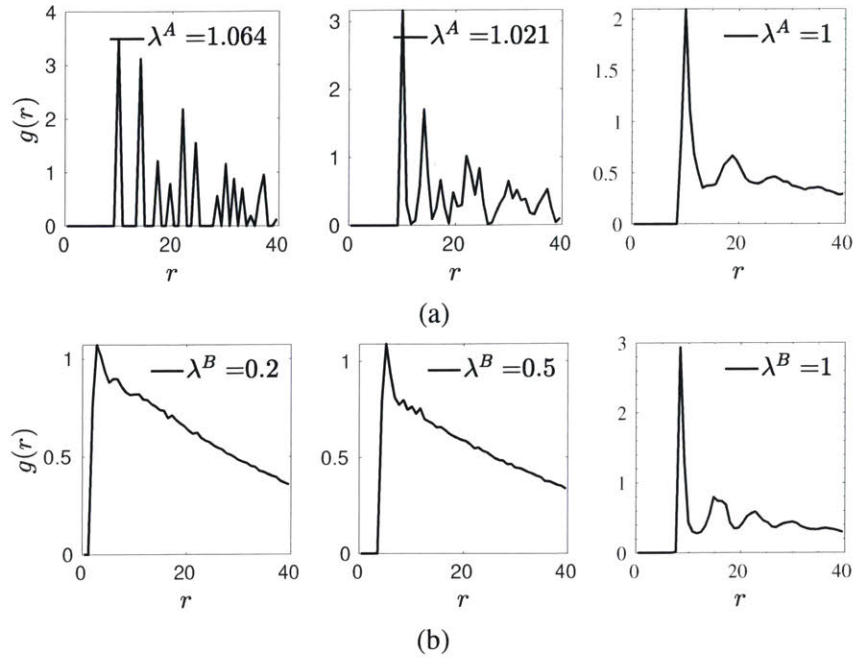


Figure 5-2: Radial distribution function  $g(r)$  for Type A (5-2a) and Type B (5-2b) structures.

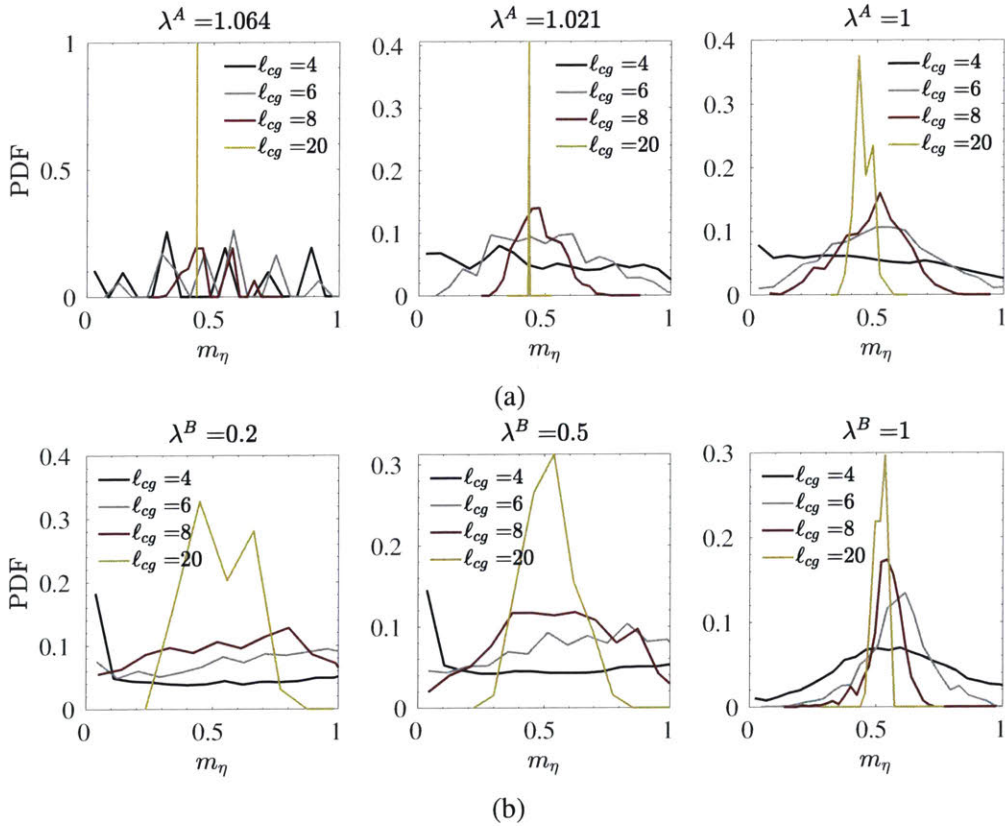


Figure 5-3: Distributions for  $m_\eta$  computed at different coarse graining length scale for Type A (5-3a) and Type B (5-3b) structures.

tains a periodic arrangement of  $N_p$  monodisperse particles of radius  $R$  in a cubic box of size  $L_x = L_y = L_z = L$  arranged with periodicity  $l = L/\sqrt[3]{N_p}$  (see Fig. 5-1a). Disorder is introduced through random Monte-Carlo moves of each particle with an apparent pore radius  $R_{app} = \lambda R$  with  $\lambda \in [1, l/(2R)]$ . The  $\lambda$  parameter reflects the degree of spatial disorder of the particles varying from a quasi-ordered state  $\lambda = l/(2R)$  to a disordered one  $\lambda = 1$  (see Fig. 5-1b). Three samples of Type A are created with  $\lambda^A \in \{1.064, 1.021, 1.0\}$ ,  $N_p = 512$ ,  $L = 80$ ,  $R = 4.7$  and overall packing density  $\eta = 0.43$ . This method of generating porous structures has been employed before to study the effective elasticity [77] and the failure of disordered porous media [80].

Type B - Overlapping monodisperse particles: A hybrid Grand Canonical Monte Carlo and Molecular Dynamics (GCMC-MD) method was used to generate structures using LAMMPS [99] with overlapping particles leading to structures exhibiting  $\lambda \in [0, 1]$  with  $\lambda = 0$  corresponding to total overlap (fully penetrable particles) while  $\lambda = 1$  represents the non-overlapping case (see [125]). In this method,  $N_p$  is adjusted to achieve the desired packing density while  $R_{app}$  is imposed through a short-ranged generalized Lennard-Jones interaction potential,  $V(r)$ :

$$V(r) = 6\epsilon \left[ \left( \frac{\sigma}{r} \right)^{2\gamma} - \left( \frac{\sigma}{r} \right)^\gamma \right] \quad (5.1)$$

with  $r$  denoting the inter-particle distance,  $\epsilon$  is the well depth between two particles of diameter  $\sigma$ . The cut-off radius is chosen to be  $r_{cr} = 2^{1/\gamma}\sigma$  corresponding to the distance at which the potential  $V(r)$  is a minimum and  $\gamma = 12$ . The apparent particle radius,  $R_{app}$  is imposed via  $\sigma = 2R_{app}$ . This method of generating porous structures is used for a number of investigations in the literature including the formation of cement hydrates [64]. Three samples of Type B are created with  $\lambda^B \in \{0.2, 0.5, 1.0\}$ ,  $L = 80$ ,  $N_p \in \{1510, 1195, 955\}$ ,  $R = 4$  and an overall packing density  $\eta = 0.50$ . To avoid any confusion, superscript  $A$  and  $B$  are added to  $\lambda$  to denote Type A and Type B structures, respectively. Two of these structures with the same spatial disorder and no particle overlaps, i.e.  $\lambda^A = 1$  and  $\lambda^B = 1$ , provide a platform to study the effect of packing density,  $\eta$ .

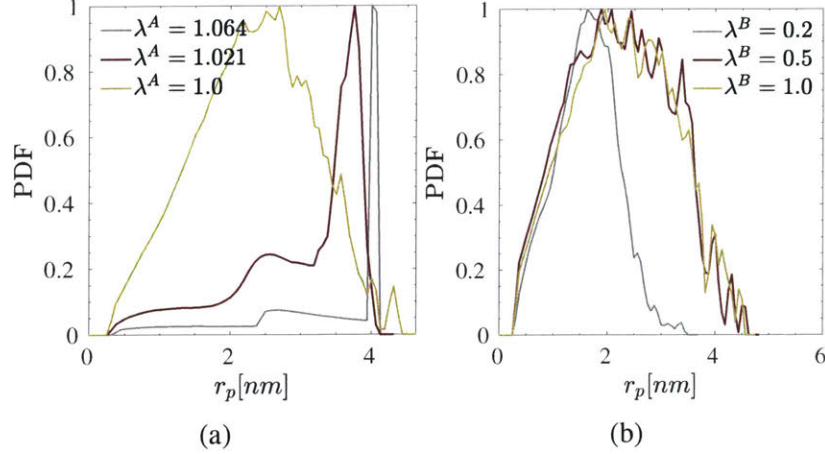


Figure 5-4: Pore size (radius  $r_p$ ) distributions for Type A (5-4a) and Type B (5-4b) structures.

The pore size distribution (PSD) of these structures are characterized via determining the largest sphere that can pass through a point in the pore space without overlapping with the pore wall. This is achieved utilizing the methodology presented by [51, 15]. The results are shown in Fig. 5-4 for a test particle of radius  $R = 0.25$  which corresponds to the smallest lattice spacing ( $a_0 = 0.25$ ) used for the simulations. The created structures exhibit a wide range of pore size distributions with the shape of the distributions for the ordered and quasi-ordered structures, i.e.  $\lambda^A = 1.064$  and  $\lambda^A = 1.021$ , departing from the rest reflecting the higher density of large pores (see Fig. 4-8).

Furthermore, the structure of these porous media are characterized via computing their radial distribution functions,  $g(r)$ . The  $g(r)$  provides information regarding probability of finding a particle at distance  $r$  from a reference particle relative to the average spatial distribution of the particles. Figs. 5-2a and 5-2b display  $g(r)$  for Type A and Type B structures, respectively. As spatial distribution of particles become more disordered for Type A structures, long-ranged sharp peaks disappear. For Type B structures, there is a sharp peak associated with  $R_{app}$  in overlapped structures, i.e.  $\lambda^B = 0.2$  and  $\lambda^B = 0.5$ , followed by a decreasing  $g(r)$ . For  $\lambda^B = 1.0$  the short ranged sharp peak is followed by two other peaks with decreasing amplitudes.

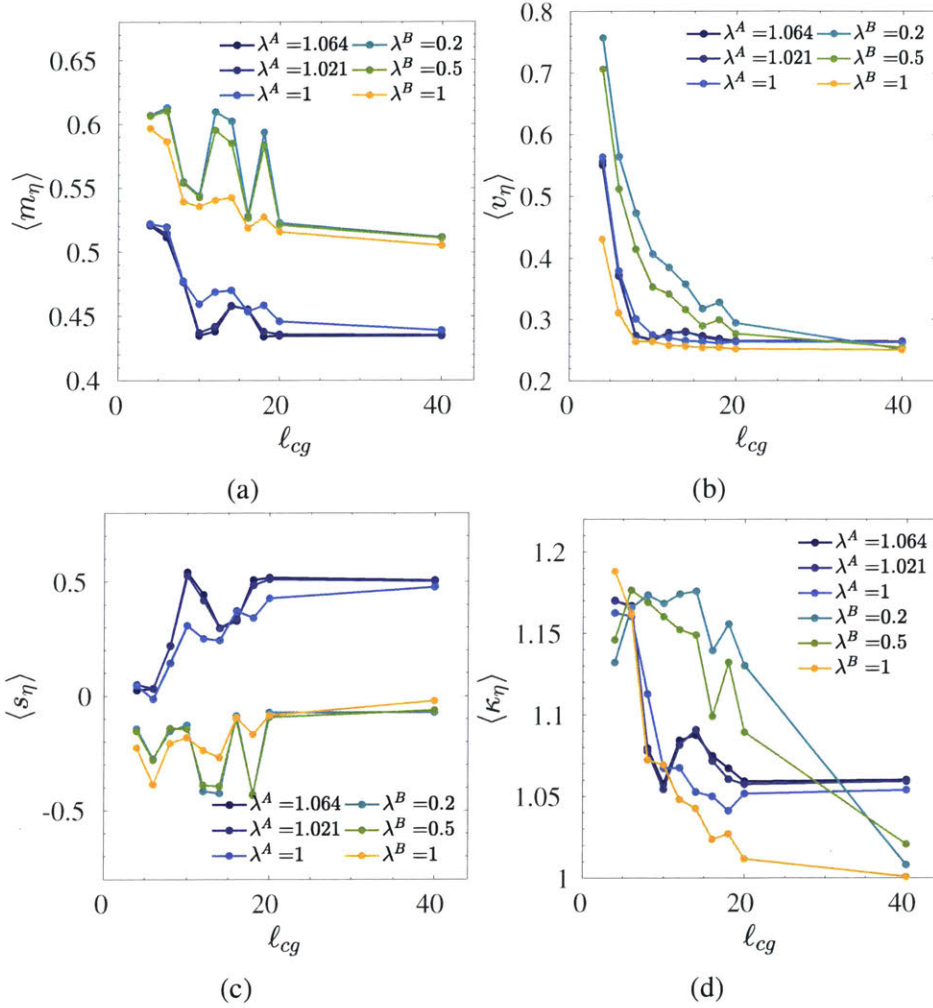


Figure 5-5: Averaged statistical descriptors, mean (5-5a), variance (5-5b), skewness (5-5c) and kurtosis (5-5d) plotted against the corresponding coarse-graining length scale  $\ell_{cg}$  for Type A and B structures.

To further characterize these structures, the probability density function (PDF) of local packing density  $\eta$  is computed. The distributions for local  $\eta$  provide insights into various quantities of interest including microtextural disorder and confinement at a given length scale. In general, the length scale dependent PDFs of a physical quantity of interest  $x$  can be accessed through coarse-graining  $x$  in a number of sub-volumes (in 3D) sufficient to sample the entire volume of the system. Then for each sub-volume, statistical distributions of  $x$  can be characterized. For the presented investigation, cubic sub-volumes of coarse-graining length  $\ell_{cg} \in \{4, 6, 8, 10, 12, 14, 16, 18, 20, 40\}$  are employed to sample the entire structure with periodic boundary conditions in all directions (for cubic sub-volumes probing

the edges). For each extracted sub-volume, the distribution of  $x$  for  $n$  observations is characterized by its first four cumulants, i.e. mean  $m_x$ , variance  $v_x$ , skewness  $s_x$  and kurtosis  $\kappa_x$  defined as follows:

$$m_x = \langle x \rangle = \frac{1}{n} \sum_i^n x_i \quad (5.2)$$

$$v_x = \frac{1}{n-1} \sum_i^n (x_i - m_x)^2 \quad (5.3)$$

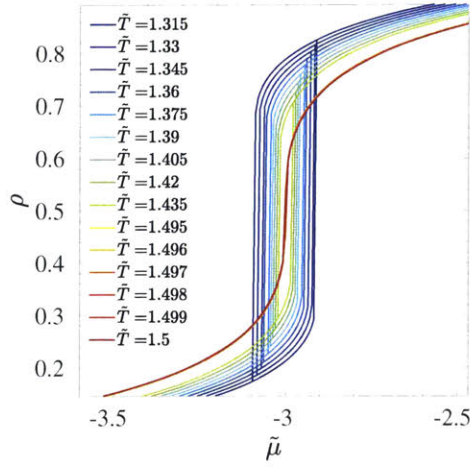
$$s_x = \langle (x - m_x)^3 \rangle / \langle (x - m_x)^2 \rangle^{3/2} \quad (5.4)$$

$$\kappa_x = \langle (x - m_x)^4 \rangle / \langle (x - m_x)^2 \rangle^2 \quad (5.5)$$

Figs. 5-3a and 5-3b display the distributions for  $m_\eta$  for  $\ell_{cg} = \{4, 6, 8, 20\}$  and for both Type A and B structures, respectively. For Type A structures, one observes a Dirac's delta function for  $\lambda^A = 1.064$  and  $\ell_{cg} = 20$  since this is the reference ordered structure with  $\ell_{cg} = 2l$  and  $l$  representing the length associated with a unit cell of the reference configuration. For  $\lambda^A = 1.021$  and  $\ell_{cg} = 20$ , the distribution slightly broadens due to spatial disorder introduced to the particles and eventually for  $\lambda^A = 1.0$  and  $\ell_{cg} = 20$ , the PDF broadens even more with two distinct but adjacent peaks. To further characterize this length scale dependency, the averaged  $m_\eta$ ,  $v_\eta$ ,  $s_\eta$  and  $\kappa_\eta$  for different  $\ell_{cg}$  are shown in Fig. 5-5. The results suggest that generally the four statistical descriptors converge around  $\ell_{cg} = 20$  with the exception for Type B structures and  $\langle \kappa_\eta \rangle$  which seems to converge at a larger length scale,  $\ell_{cg} = 40$ .

## 5.2.2 Discrete Fluid Description

Generally in density functional theory (DFT) approaches the free energy of the system of particles can be uniquely defined as a functional of inhomogeneous density and for a given Hamiltonian  $\mathcal{H}$  and external potential. The equilibrium density distribution  $\rho_{\text{eq}}$  is obtained through minimization of the free energy functional. The coarse-grained lattice gas model is the discrete version of DFT restricted to nearest neighbor interactions. It provides a mean-field approach to study capillary phenomena. In this study, a liquid-gas fluid mixture



(a)

Figure 5-6: Isotherms for bulk fluid for different temperatures. The critical point of bulk fluid for a simple cubic lattice ( $\tilde{T} = 1.5$ ,  $\rho_c = 0.5$ ) is captured.

is considered. The interface between the two fluids is considered to be diffusive (see for e.g. [105]), i.e. non-zero thickness, with physical quantities smoothly varying between the bulk values in each phase [52]. The coarse-grained lattice gas density functional theory [70, 71] is employed to capture this binary fluid mixture. The Hamiltonian for this model reads:

$$\mathcal{H} = -w_{ff} \sum_i^N \sum_j^{N_i^b} \tau_i \eta_i \tau_j \eta_j - w_{sf} \sum_i^N \sum_j^{N_i^b} [\tau_i \eta_i (1 - \eta_j) + \tau_j \eta_j (1 - \eta_i)] \quad (5.6)$$

where  $\tau_i = 0, 1$  and  $(1 - \eta_i) = 0, 1$  denote the fluid and matrix occupancy variables, respectively. Furthermore,  $N$  is the total number of nodes and  $N_i^b$  represents number of neighboring sites for node  $i$ . Additionally,  $w_{ff} > 0$  and  $w_{sf} > 0$  are energy parameters that quantify the strength of liquid-liquid and solid-liquid interactions. These strength parameters can be imposed via  $y = w_{sf}/w_{ff}$  which is the ratio of these interaction parameters. For a given matrix realization  $\{\eta_i\}$ , the fluid's free-energy functional,  $\Psi^f$ , reads:

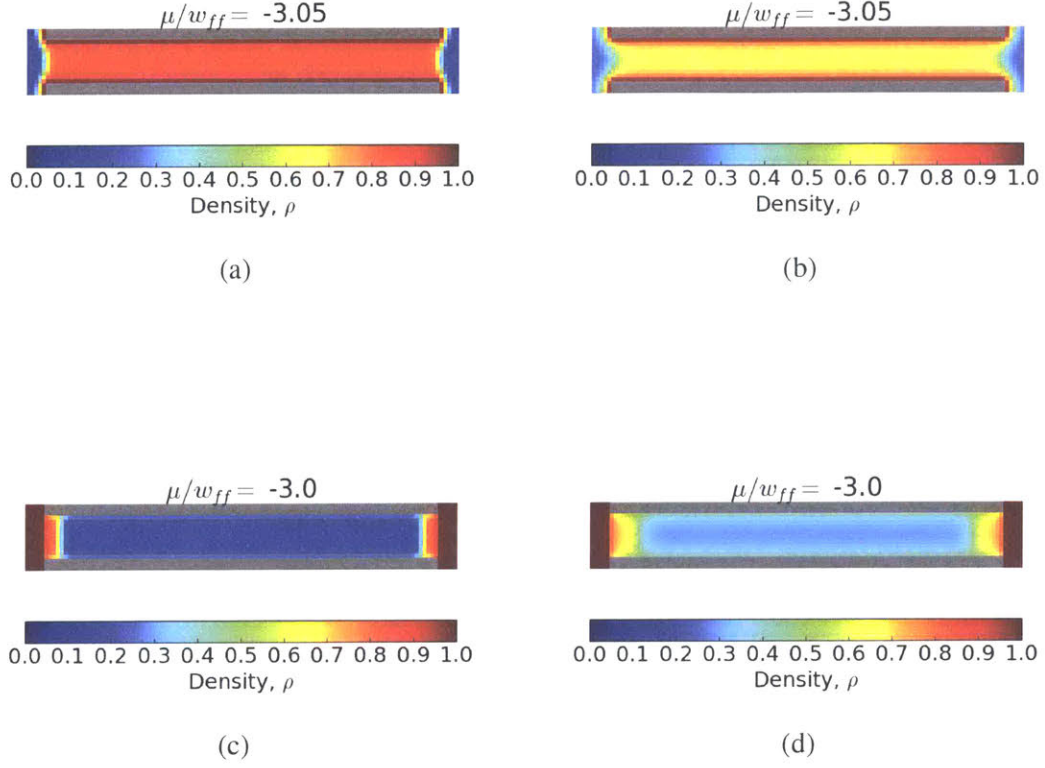


Figure 5-7: Density map for sorption in cylindrical pores (in 3D) with lengths  $L_x = 100$ ,  $L_y = L_z = 8$ , radius  $R = 6$ , lattice-spacing  $a_0 = 1.0$ , and reservoir length  $L_x^{\text{res}} = 4$  added at the ends of the pore. The cross-sections correspond to  $z = L_z/2 = 4$  and  $y = 3.0, \tilde{T} = 1.2$  (5-7a),  $y = 3.0, \tilde{T} = 1.4$  (5-7b),  $y = 0.5, \tilde{T} = 1.2$  (5-7c) and  $y = 0.5, \tilde{T} = 1.4$  (5-7d). The external reservoir is initiated and kept at  $\rho = 1$  for 5-7c and 5-7d while it evolves with the cylindrical pore for 5-7a and 5-7b.

$$\Psi^f(\{\rho_i\}) = \frac{1}{\beta} \sum_i^N [\rho_i \ln \rho_i + (\eta_i - \rho_i) \ln (\eta_i - \rho_i)] - w_{ff} \sum_i^N \sum_j^{N_i^p} \rho_i \rho_j \quad (5.7)$$

$$-w_{sf} \sum_i^N \sum_j^{N_i^p} [\rho_i (1 - \eta_j) + \rho_j (1 - \eta_i)] \quad (5.8)$$

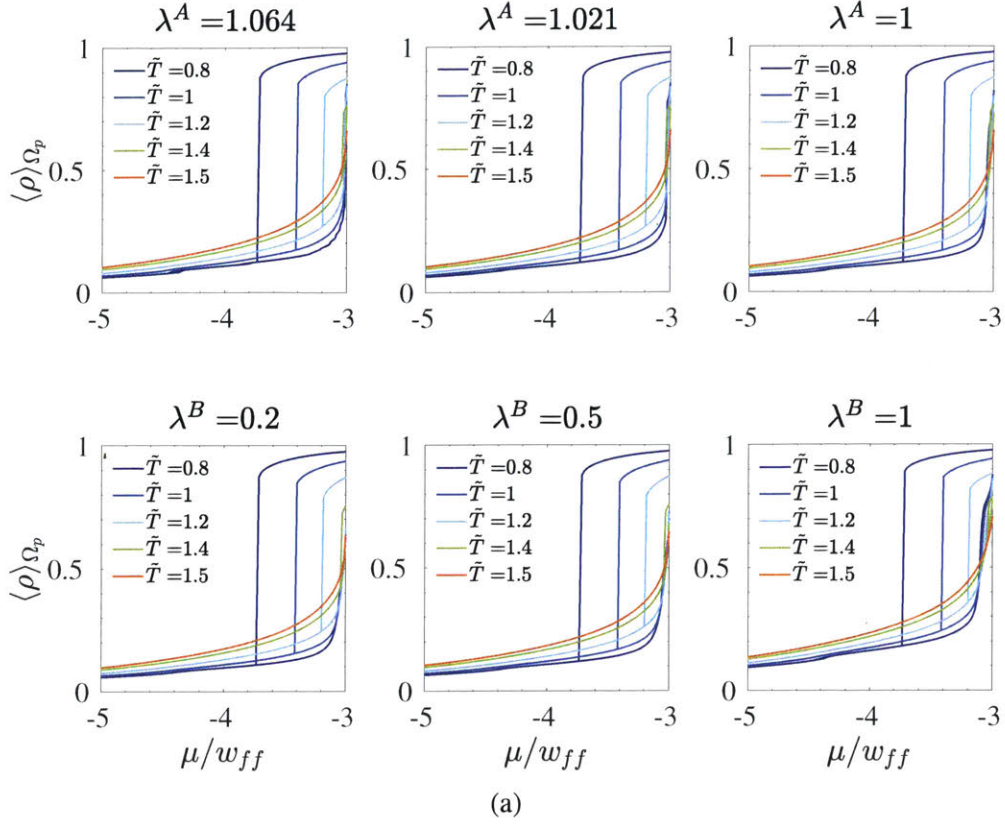


Figure 5-8: Isotherms for different structures and  $\tilde{T}$ .

where  $\beta = 1/k_B T$  with  $k_B$  and  $T$  denoting Boltzmann constant and temperature, respectively. Additionally,  $\rho_i$  denotes normalized fluid density at position  $\vec{x}_i$ :

$$\rho_i \equiv \rho(\vec{x}_i) = \frac{\rho_f(\vec{x}_i)}{\rho_f^b} \quad \rho_i \in [0, 1] \quad (5.9)$$

with  $\rho_f^b$  representing the bulk fluid density. Normalized density field  $\rho(\vec{x})$  serves as the only order-parameter in the model. For a given chemical potential,  $\mu$ , minimization of the fluid grand potential functional,  $\Omega^f(\{\rho_i\}) = \Psi^f(\{\rho_i\}) - \mu \sum_i^N \rho_i$ , provides the equilibrium density distribution in the system. In the continuum limit, the free energy of the lattice model corresponds to the Cahn-Hilliard model [137]. For a cubic crystal or isotropic medium invariant to the symmetry operations of reflection and of rotation, Taylor expansion of specific free energy of a fluid,  $f^f$ , around a homogeneous state,  $f_0^f$ , reads [27]:

$$f^f(\rho, \vec{\nabla}\rho, \vec{\nabla}^2\rho, \dots) = f_0^f(\rho) + \kappa_1 \vec{\nabla}^2\rho + \kappa_2 (\vec{\nabla}\rho)^2 + \dots \quad (5.10)$$

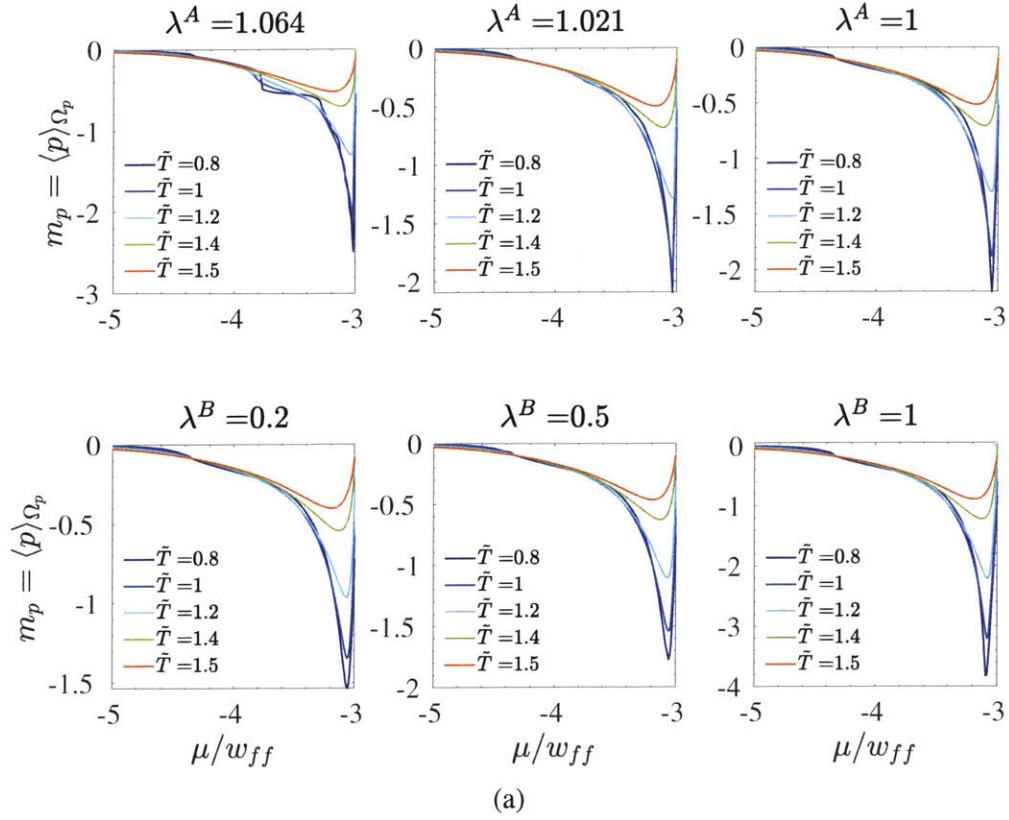


Figure 5-9: First cumulant of capillary pressure field as it evolves with imposed chemical potential  $\mu$  for different structures and temperatures.

The mean-field approximation of Cahn-Hilliard-like phase field energy functional representing total free energy of fluid,  $F^f$  for a volume  $V$  of the solution reads:

$$F^f = \int_V \left( f_0^f(\rho) + \kappa_1 \vec{\nabla}^2 \rho + \kappa_2 (\vec{\nabla} \rho)^2 + \dots \right) dV \quad (5.11)$$

Expanding the second term in Eq.(5.11) by applying the divergence theorem leads to:

$$F^f = \int_V \left( f_0^f(\rho) + \left( \frac{-d\kappa_1}{d\rho} + \kappa_2 \right) (\vec{\nabla} \rho)^2 + \dots \right) dV + \int_{\partial V} (\kappa_1 \vec{\nabla} \rho \cdot \vec{n}) dS \quad (5.12)$$

where  $\vec{n}$  is the normal to boundary surface,  $dS$ . Neglecting terms beyond second-order results in [27]:

$$F^f = \int_V \left( f_0^f(\rho) + \kappa (\vec{\nabla} \rho)^2 \right) dV + \int_{\partial V} (\kappa_1 \vec{\nabla} \rho \cdot \vec{n}) dS \quad (5.13)$$

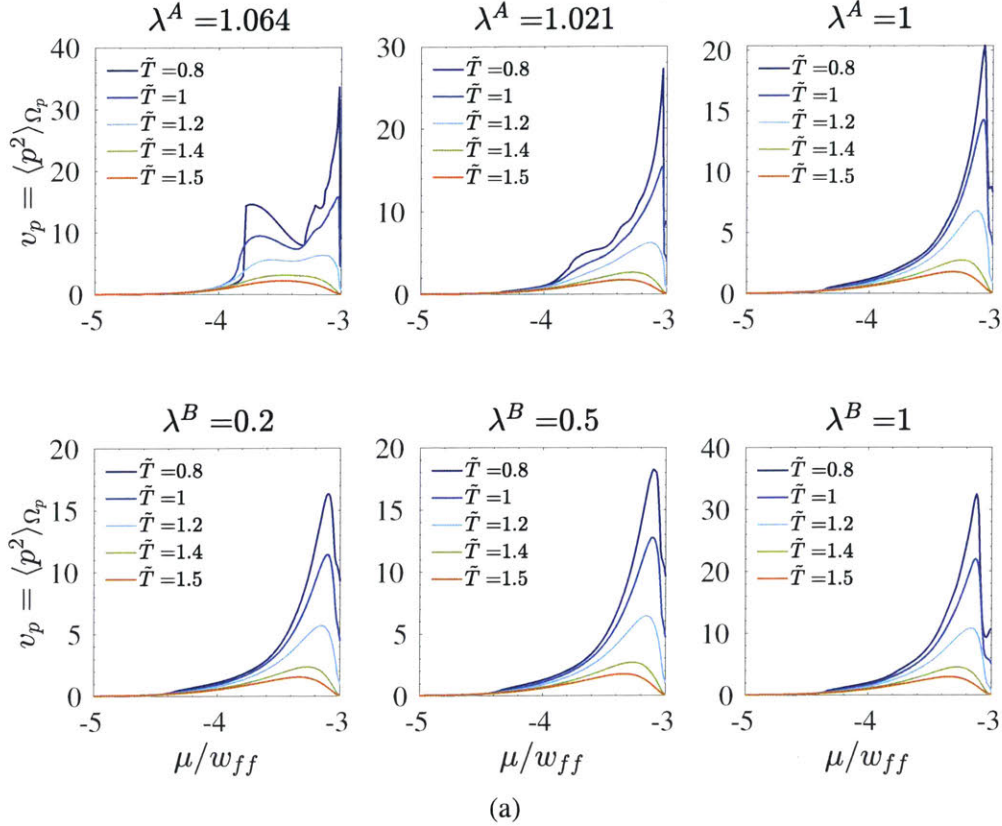


Figure 5-10: Second cumulant of capillary pressure field as it evolves with imposed chemical potential  $\mu$  for different structures and temperatures.

where  $\kappa$  is a gradient energy coefficient that quantifies gradient energy cost of creating inhomogeneity in an otherwise homogeneous system and  $\kappa = -d\kappa_1/d\rho + \kappa_2$ . In general,  $\kappa$  depends on density, temperature and concentration among other field variables and can be related to the pair-correlation functions. The general form of the Ginzburg-Landau free energy - here the grand potential - as a functional of  $\rho(\vec{x})$  and its gradient respecting symmetries read [67]:

$$G^f = \int_V dV (-\mu\rho + f^f(\rho, \vec{\nabla}\rho)) = \int_V \left( f_0^f(\rho) - \mu\rho + \frac{1}{2}\kappa(\vec{\nabla}\rho)^2 \right) dV + \int_{\partial V} (\kappa_1 \vec{\nabla}\rho \cdot \vec{n}) dS \quad (5.14)$$

Eq.(5.14) can be parameterized for the lattice gas model which in the continuum limit reads [137]:

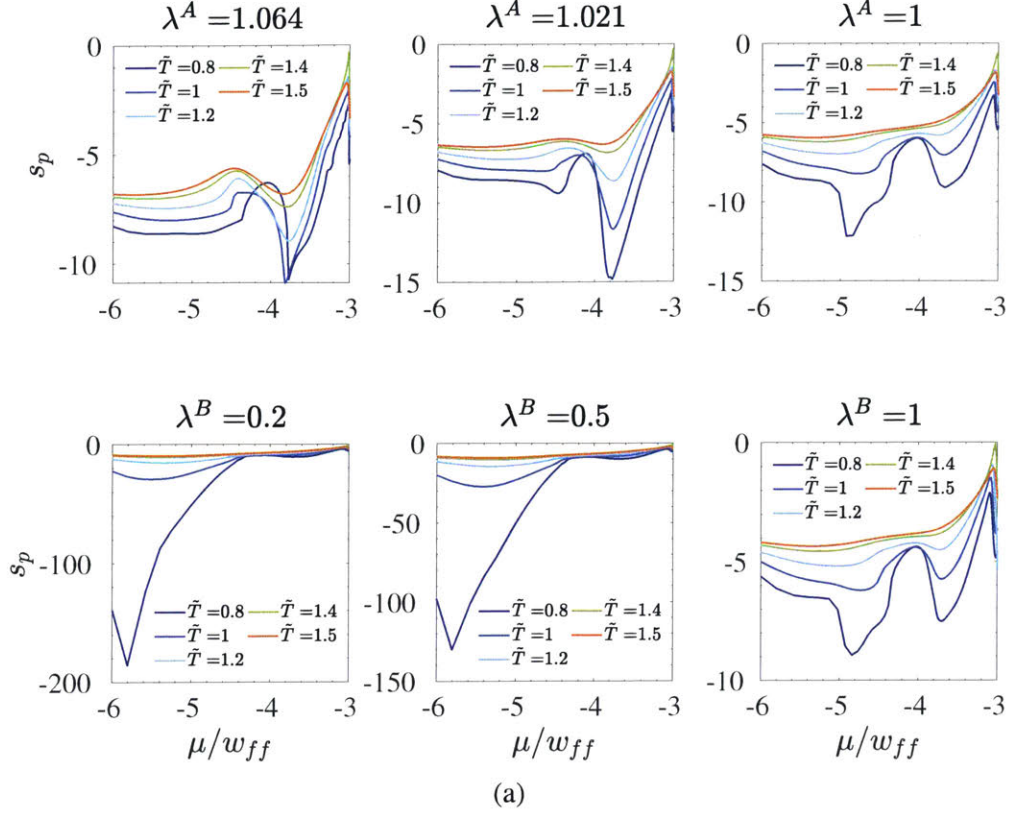


Figure 5-11: Skewness of capillary pressure field as it evolves with imposed chemical potential  $\mu$  for different structures and temperatures.

$$\begin{aligned}
 G^f = & \int_V [k_B T (\rho \ln \rho + (1 - \rho) \ln (1 - \rho)) - \mu \rho + \frac{w_{ff}}{2} a_0^2 (\vec{\nabla} \rho)^2 - \frac{w_{ff}}{2} c \rho^2] dV + \\
 & \int_S d\vec{S} \cdot \left( w_{sf} \rho \vec{n} - \frac{w_{ff}}{4} a_0^2 \rho \vec{\nabla} \rho \right)
 \end{aligned} \tag{5.15}$$

where  $a_0$  represents lattice spacing and  $c$  the coordination number, gradient energy coefficient  $\kappa = a_0^2 w_{ff}$  and  $f_0^f = k_B T (\rho \ln \rho + (1 - \rho) \ln (1 - \rho)) - \frac{c}{2} w_{ff} \rho^2$ . This energy can be minimized by taking the variational of Eq.(5.15) with the constraint  $\delta \rho|_{\partial V} = 0$  which results in [137]:

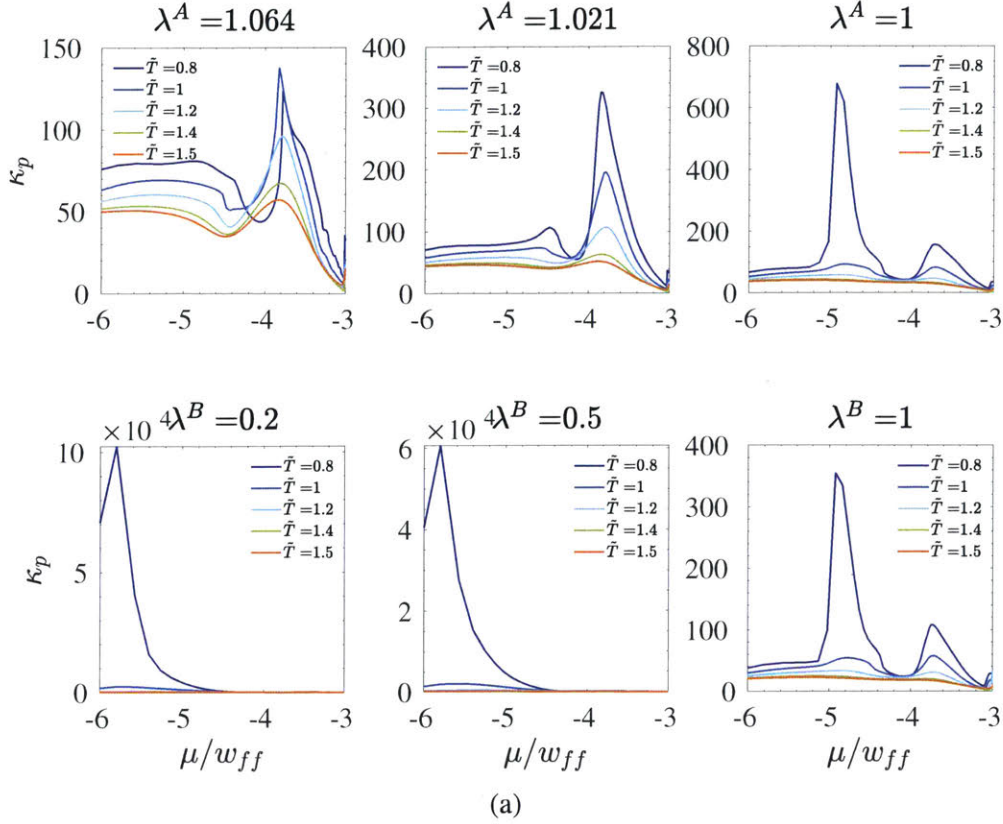


Figure 5-12: Kurtosis of capillary pressure field as it evolves with imposed chemical potential  $\mu$  for different structures and temperatures.

$$\begin{aligned}
 \delta G^f = & \int_V \left( -c w_{ff} \rho - a_0^2 w_{ff} (\vec{\nabla}^2 \rho) - \mu + k_B T \ln \left( \frac{\rho}{1-\rho} \right) \right) \delta \rho dV \\
 & + a_0^2 w_{ff} \int_{\partial V} d\vec{S} \cdot \delta \rho \vec{\nabla} \rho - \frac{a_0^2}{2} w_{ff} \int_{\partial V} d\vec{S} \cdot \rho \delta \vec{\nabla} \rho
 \end{aligned} \quad (5.16)$$

furthermore, imposing  $\delta \frac{\partial \rho}{\partial \vec{n}} |_{\partial V} = 0$  ensures that surface terms vanish. Thus, the equilibrium can be expressed as:

$$-w_{ff} (c\rho + a_0^2 \vec{\nabla}^2 \rho) + k_B T \ln \left( \frac{\rho}{1-\rho} \right) - \mu = 0 \quad (5.17)$$

from thermodynamics, the classical expression for reference pressure,  $p_0$  reads:

$$p_0 = \mu \rho - f_0^f(\rho) \quad (5.18)$$

To ensure mechanical equilibrium, the hydrostatic pressure tensor,  $\boldsymbol{\sigma}_f = p_0 \mathbf{1}$  with  $\mathbf{1}$  denoting the second order identity tensor, needs to satisfy:

$$-\vec{\nabla} \cdot \boldsymbol{\sigma}_f = -\vec{\nabla} p_0 = -\vec{f}_{ext} \quad (5.19)$$

re-writing Eq. (5.19) with Eq. (5.18) results in:

$$-\vec{\nabla} \cdot (\boldsymbol{\sigma}_f - \mu \rho \mathbf{1}) = \vec{\nabla} \cdot (f_0^f \mathbf{1}) = \frac{\partial f_0^f}{\partial \rho} \vec{\nabla} \rho \quad (5.20)$$

accounting for higher order term in the free energy, i.e.  $f^f = f^f(\rho, \vec{\nabla} \rho)$  modifies Eq. (5.20) as follows:

$$-\vec{\nabla} \cdot (\boldsymbol{\sigma}_f - \mu \rho \mathbf{1}) = \frac{\partial f^f(\rho, \vec{\nabla} \rho)}{\partial \rho} \vec{\nabla} \rho \quad (5.21)$$

specifically, the second-order term in free energy expansion, Eq. (5.13) reads:

$$F_1^f = \int_V f_1^f dV = \int_V \frac{1}{2} \kappa (\vec{\nabla} \rho)^2 dV \quad (5.22)$$

similar to Eq. (5.20), to ensure mechanical equilibrium due to contributions of Eq. (5.22), one can write:

$$\vec{\nabla} \cdot \boldsymbol{\sigma}_f = -\frac{\delta F_1^f}{\delta \rho} \vec{\nabla} \rho = \left( \frac{-\partial f_1^f}{\partial \rho} + \vec{\nabla} \cdot \frac{\partial f_1^f}{\partial \vec{\nabla} \rho} \right) \vec{\nabla} \rho = \kappa \vec{\nabla} \rho \vec{\nabla}^2 \rho \quad (5.23)$$

utilizing vector identity  $\vec{u} \cdot \vec{\nabla} \vec{u} = \vec{\nabla} \cdot (\vec{u} \otimes \vec{u}) - \vec{u} \vec{\nabla} \cdot \vec{u}$ , R.H.S. of Eq.(5.23) can be written as:

$$\kappa \vec{\nabla} \rho \vec{\nabla}^2 \rho = \kappa \left( \vec{\nabla} \cdot (\vec{\nabla} \rho \otimes \vec{\nabla} \rho) - \vec{\nabla} \rho \cdot \vec{\nabla} (\vec{\nabla} \rho) \right) \quad (5.24)$$

Additionally, since  $\vec{u} \times (\vec{\nabla} \times \vec{u}) = \frac{1}{2} \vec{\nabla} (\vec{u} \cdot \vec{u}) - \vec{u} \cdot \vec{\nabla} \vec{u}$ , Eq.(5.23) reduces to:

$$\begin{aligned} \kappa \vec{\nabla} \rho \vec{\nabla}^2 \rho &= \kappa \left( \vec{\nabla} \cdot (\vec{\nabla} \rho \otimes \vec{\nabla} \rho) - \vec{\nabla} \rho \cdot \vec{\nabla} (\vec{\nabla} \rho) \right) \\ &= \kappa \left( \vec{\nabla} \cdot (\vec{\nabla} \rho \otimes \vec{\nabla} \rho) - \left( \frac{1}{2} \vec{\nabla} (\vec{\nabla} \rho \cdot \vec{\nabla} \rho) - \vec{\nabla} \rho \times (\vec{\nabla} \times \vec{\nabla} \rho) \right) \right) \end{aligned} \quad (5.25)$$

where  $\vec{\nabla} \times \vec{\nabla} \rho = 0$ . Finally, utilizing  $\vec{\nabla} (\vec{u} \cdot \vec{u}) = \vec{\nabla} \cdot (\vec{u} \cdot \vec{u} \mathbf{1})$ , Eq.(5.23) now reads:

$$\begin{aligned}
\kappa \vec{\nabla} \rho \vec{\nabla}^2 \rho &= \kappa \left( \vec{\nabla} \cdot (\vec{\nabla} \rho \otimes \vec{\nabla} \rho) - \vec{\nabla} \rho \cdot \vec{\nabla} (\vec{\nabla} \rho) \right) \\
&= \kappa \left( \vec{\nabla} \cdot (\vec{\nabla} \rho \otimes \vec{\nabla} \rho) - \left( \frac{1}{2} \vec{\nabla} (\vec{\nabla} \rho \cdot \vec{\nabla} \rho) - \vec{\nabla} \rho \times (\vec{\nabla} \times \vec{\nabla} \rho) \right) \right) \\
&= \kappa \vec{\nabla} \cdot \left( (\vec{\nabla} \rho \otimes \vec{\nabla} \rho) - \frac{1}{2} (\vec{\nabla} \rho \cdot \vec{\nabla} \rho \mathbf{1}) \right)
\end{aligned} \tag{5.26}$$

Thus, capillary-stress tensor for a binary-fluid can be written as [72, 6]:

$$\sigma_f = \left( p_0(\rho) - \frac{1}{2} \kappa (\vec{\nabla} \rho)^2 \right) \mathbf{1} + \kappa \vec{\nabla} \rho \otimes \vec{\nabla} \rho + \sigma_0 \tag{5.27}$$

where  $p_0(\rho)$  is defined in Eq.(5.18) and represents the asymptotic bulk value of the hydrostatic pressure and  $\sigma_0$  is an arbitrary constant tensor. Thus, the capillary pressure,  $p$  can be obtained as follows:

$$p = \frac{1}{3} \text{tr} \sigma_f \tag{5.28}$$

The fluid-fluid interaction strength,  $w_{ff}$ , can be calibrated according to the bulk critical temperature,  $T_c^{3D}$  [71]:

$$k_B T_c^{3D} = \frac{c w_{ff}}{4} \tag{5.29}$$

where  $c$  denotes the lattice coordination number. The characteristic length scale for lattice can be obtained by combining energy parameter  $w_{ff}$  with surface tension,  $E_s$ . Estimates for surface energy between liquid-gas interface results in [137]:

$$E_s \sim \frac{w_{ff}}{2a_0^2} \tag{5.30}$$

The dimensionless form of these parameters read:

$$\tilde{\mu} = \mu/w_{ff} \quad \tilde{T} = k_B T/w_{ff} \quad \tilde{w}_{ff} = w_{ff}/w_{ff} \quad \tilde{w}_{sf} = w_{sf}/w_{ff} \tag{5.31}$$

In what follows, we have utilized a simple cubic lattice in 3D with  $c = 6$ . From the standard mean field equation of state for lattice with  $c = 6$ , we expect a critical point located at  $\tilde{T} = k_B T_c^{3D} / w_{ff} = c/4 = 1.5$  and  $\rho_c = 0.5$  for the bulk fluid which is readily reproduced as shown in Fig. 5-6. The fluid-solid wall interactions can be derived from *ab initio* calculations (see for e.g. [21]). It is often necessary to calibrate these potentials to reproduce experimental data that depends on fluid-solid interactions such as the isosteric heat of adsorption [33].

Furthermore, the qualitative behavior of our implemented Coarse Grained Lattice Gas (CGLG) DFT is examined utilizing simple pore geometries. Specifically, long cylindrical pores are considered with  $L_x = 100$ ,  $L_y = L_z = 8$  and  $R = 6$ . Reservoir are added to ends of the pore with  $L_x^{\text{res}} = 4$ . Fig. 5-7 display density maps during condensation for cross-section  $z = 4$ ,  $a_0 = 1.0$  and for various reservoir conditions,  $y = w_{sf}/w_{ff}$ , and temperatures. These maps are qualitatively comparable with higher resolution methods such as Grand Canonical Monte Carlo (GCMC) simulations. For example surface wetting in the form of liquid film formation is expected to occur in the wetting case (see Figs. 5-7a and 5-7b), i.e.  $y = 3.0$ , and during condensation. This is however is not the case for the non-wetting, i.e.  $y = 0.5$  case (see Figs. 5-7c and 5-7d). Furthermore, similar concave menisci at the cylindrical pore ends during filling for a wetting fluid (see Figs. 5-7a and 5-7b) and convex menisci for filling with non-wetting fluids (see Figs. 5-7c and 5-7d) can be observed in GCMC simulations [33].

## 5.3 Results

### 5.3.1 Criticality & Confinement

Experimental observations, theoretical modeling and molecular simulations of capillary condensation in porous solids point to the existence of a temperature beyond which capillary condensation becomes reversible - this is known as capillary critical temperature,  $T_{cc}$ . As temperature increases, the hysteresis loop shrinks and eventually disappears at  $T = T_{cc} <$

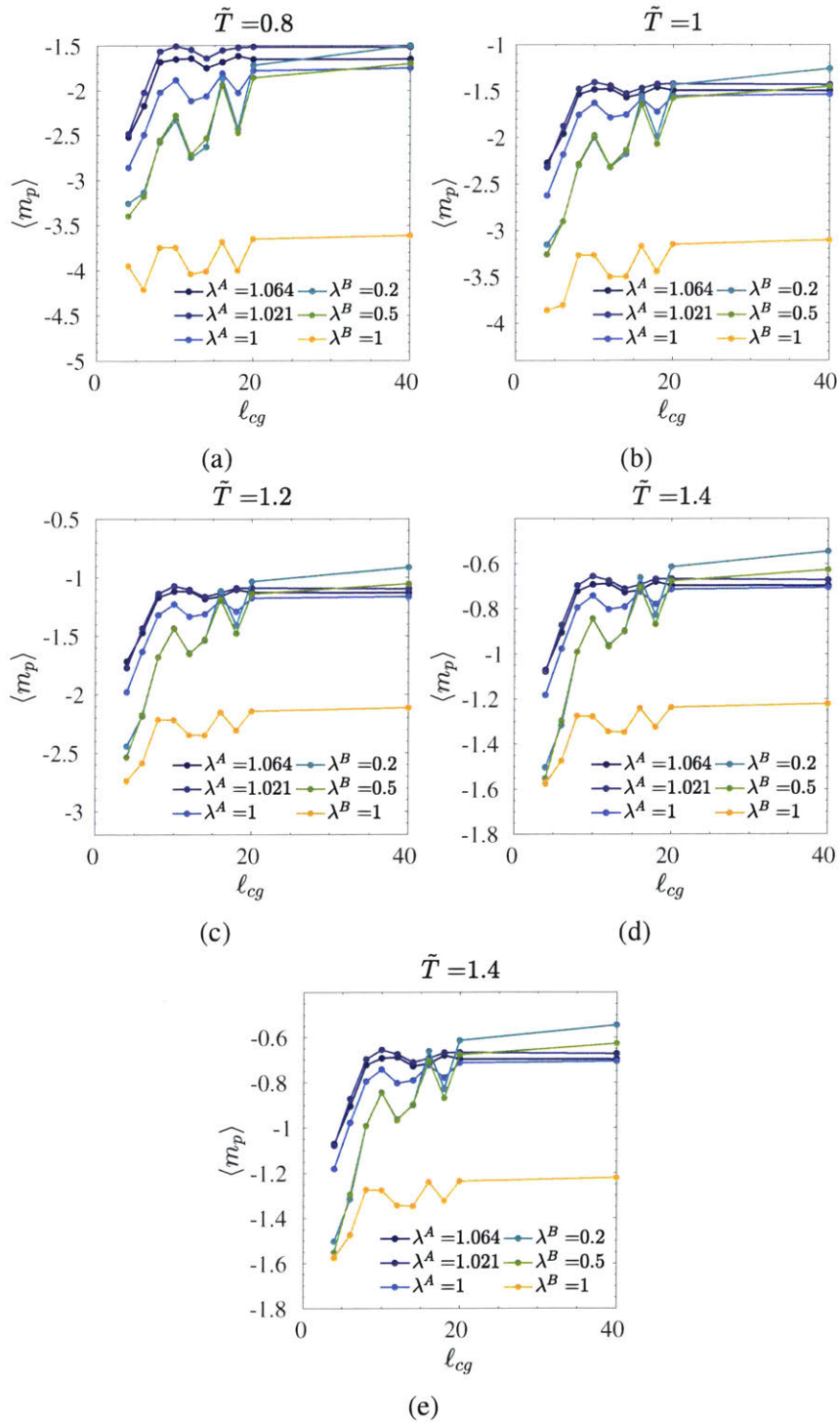


Figure 5-13: Coarse-grained mean for capillary pressure field for all structures and temperatures  $\tilde{T} = 0.8$  (5-13a),  $\tilde{T} = 1.0$  (5-13b),  $\tilde{T} = 1.2$  (5-13c),  $\tilde{T} = 1.4$  (5-13d) and  $\tilde{T} = 1.5$  (5-13e) plotted against the corresponding coarse-graining length scale  $\ell_{cg}$  at  $h = 0.90$ .

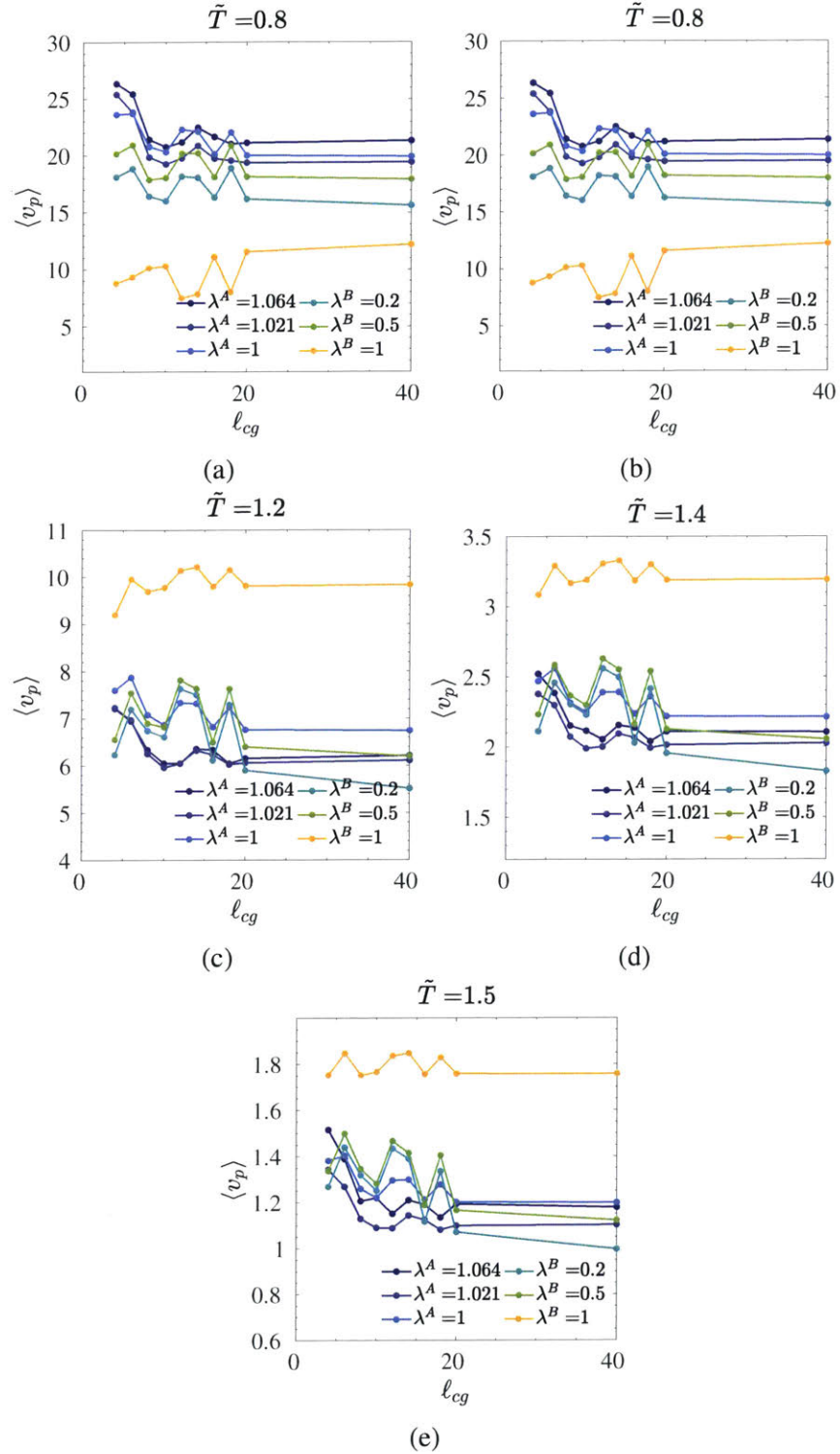


Figure 5-14: Coarse-grained variance for capillary pressure field for all structures and temperatures  $\tilde{T} = 0.8$  (5-14a),  $\tilde{T} = 1.0$  (5-14b),  $\tilde{T} = 1.2$  (5-14c),  $\tilde{T} = 1.4$  (5-14d) and  $\tilde{T} = 1.5$  (5-14e) plotted against the corresponding coarse-graining length scale  $\ell_{cg}$  at  $h = 0.90$ .

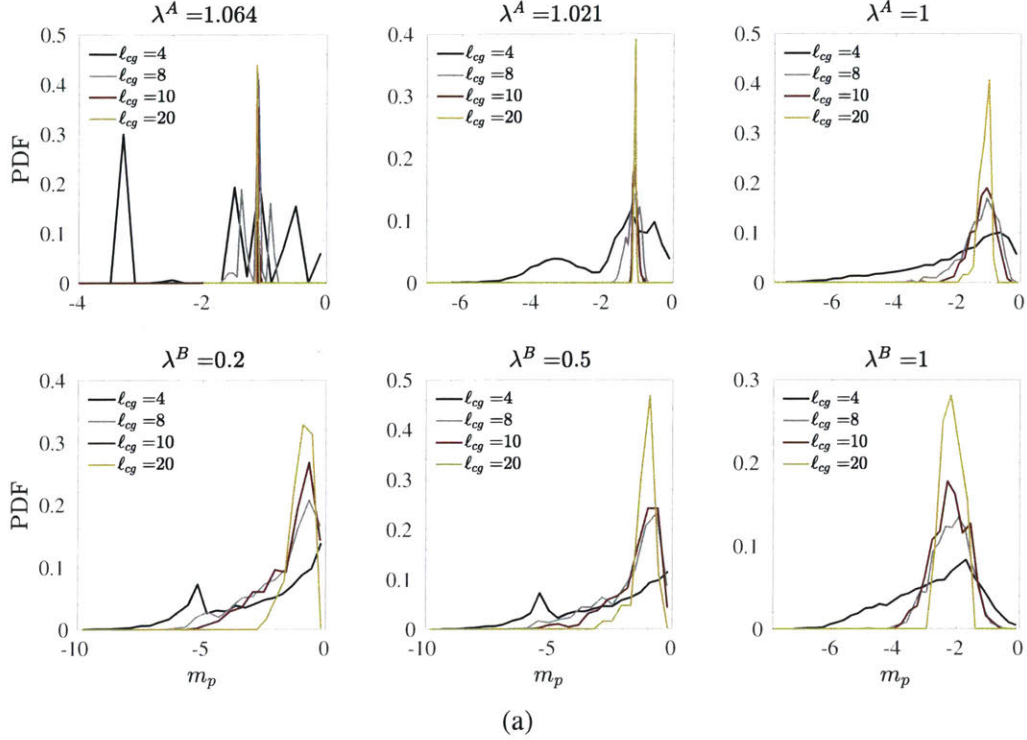


Figure 5-15: Distributions for  $m_p$  computed at different coarse-graining length scale for different structures,  $\tilde{T} = 1.2$  and  $h = 0.90$ .

$T_c^{3D}$  (see for e.g. [49]). This shift in critical temperature due to confinement can be characterized as  $\Delta T_c = T_c^{3D} - T_{cc}$ . Experimental data and simulations on vycor and cylindrical pores suggest a one-to-one scaling,  $\Delta T_c / T_c^{3D} \sim 2\sigma / \langle r_p \rangle$  with  $\sigma$  representing the diameter of a molecule ( $\approx a_0$  in the coarse-grained lattice gas model) and  $\langle r_p \rangle$  denoting the mean of pore radius distribution (see [33]). To ensure the implemented fluid description in this work utilizing the Coarse Grained Lattice Gas (CGLG) can reproduce this scaling, the capillary critical temperature  $T_{cc}$  for cylindrical pores with  $r_p \in \{2, 4, 6, 8\}$  and  $a_0 \in \{0.2, 0.25, 0.5, 1\}$  with a temperature resolution of  $\approx 4$  K was determined. Additionally, the level of confinement for granular packings employed in this work is explored by determining their capillary critical temperatures. This is done by considering three different lattice spacings  $a_0 \in \{0.25, 0.5, 1.0\}$ . The average pore radius  $\langle r_p \rangle$  is obtained from Fig. 5-4. The shift in critical temperature,  $\Delta T_c / T_c^{3D}$ , is plotted against disorder parameter  $\lambda$  for a given lattice spacing  $a_0$  as shown in Figs. 5-17a and 5-17b for Type A and Type B structures, respectively. Furthermore, for both cylindrical pores and disordered particle packings the

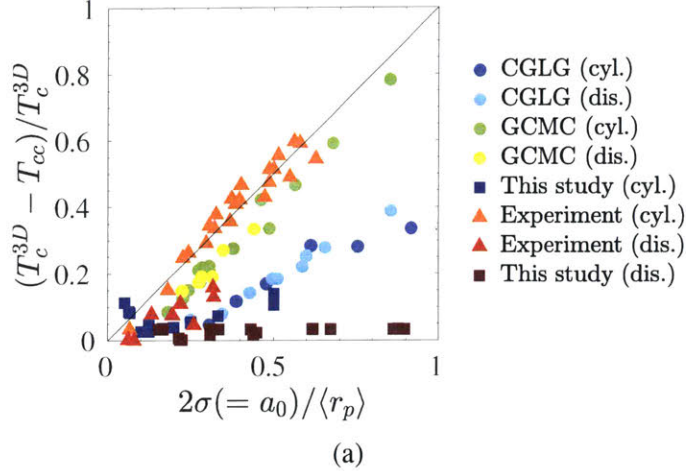


Figure 5-16: Shift in capillary critical temperature  $T_{cc}$  as a function of  $2\sigma/R_p$ .

shift in capillary critical temperature along with data from literature are displayed in Fig. 5-16. In terms of methodology the data in literature can be grouped into simulations - either Coarse Grained Lattice Gas (CGLG) or Grand Canonical Monte Carlo (GCMC) - and experiments. In terms of materials, the published  $T_{cc}$  values correspond to either cylindrical pores with a given pore radius or vycor samples with a sharp (narrow) pore size distribution and thus a well defined  $\langle r_p \rangle$ . This significantly departs from our granular packings (vycor is a porous solid with a continuous solid matrix) exhibiting rather wide pore size distributions.

### 5.3.2 Capillary Pressure in Disordered Granular Packings

Consider the case of a bulk fluid with no confinement - for each imposed increment of chemical potential  $\mu$ , the PDFs for  $\rho(\vec{x})$  and  $p(\vec{x})$  follow a Dirac's delta function, i.e. no variations in space. This picture changes as soon as the energy landscape is perturbed via introduction of confinement. This effect is explored by simulating a binary fluid inside the described granular packings. In real units, the cubic simulation box of length  $L = 80$  nm is discretized using a lattice spacing  $a_0 = 0.25$  nm which is on par with characteristic size of a water molecule. A reservoir of length  $L = 5$  nm is added in each direction while imposing periodic boundary conditions (PBC) in all directions. The density field in the reservoir domain,  $\Omega_{\text{res}}$ , evolves with each increment during both condensation

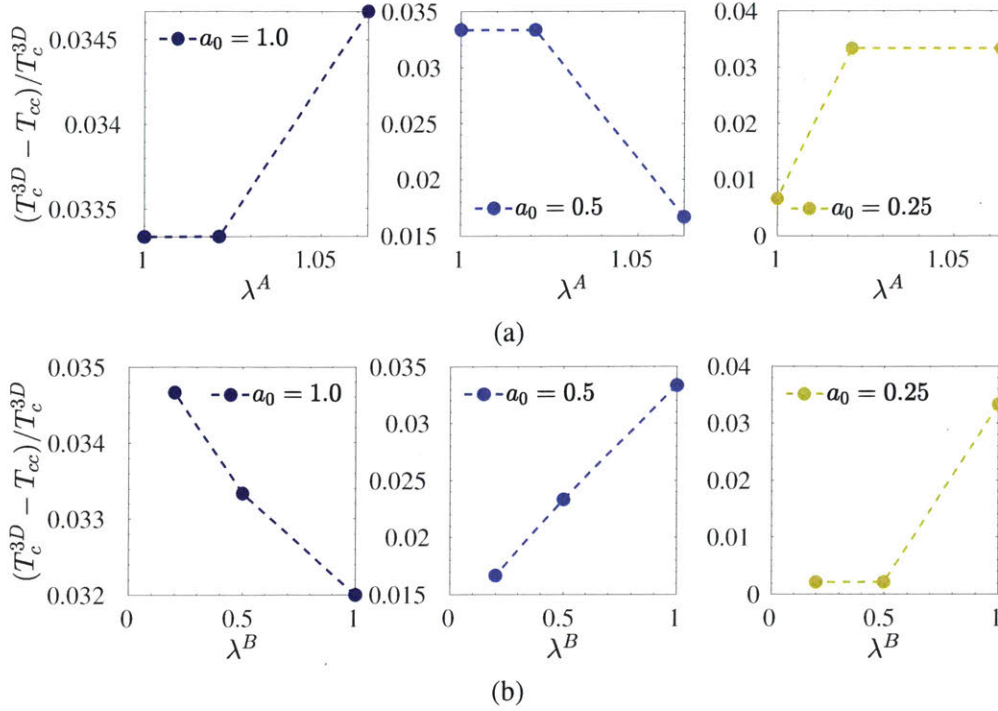


Figure 5-17: Shift in capillary critical temperature  $T_{cc}$  as a function of  $\lambda^A$  and  $\lambda^B$  for an initial assessment of confinement effects on  $T_{cc}$ .

and evaporation. For each structure, simulations are done for a range of (normalized) temperatures  $\tilde{T} = k_B T / w_{ff} \in \{0.8, 1.0, 1.2, 1.4, 1.5\}$  and for  $y = w_{sf} / w_{ff} = 2.5$  by imposing  $\mu$  and consequently relative humidity  $h = \exp((\mu - \mu_{sat}) / k_B T)$ . The resulting isotherms are shown in Fig. 5-8. It should be noted that for a simple cubic lattice ( $c = 6$ ),  $\tilde{T} = 1.5$  corresponds to the bulk critical temperature of the fluid in the CGLG approach. Additionally, for all the considered granular packings, capillary critical temperature  $T_{cc}$  for  $a_0 = 0.25$  lies between  $1.4 < \tilde{T}_{cc} < 1.5$ . The capillary pressure field inside the pore domain is characterized utilizing the first four cumulants of its (spatial) distribution. Pore domain is defined as all fluid nodes with no solid neighbors. Additionally prior to any analyses, the average pressure of the reservoir  $\langle p \rangle_{\Omega_{res}}$  is subtracted from the capillary pressure scalar field,  $p(\vec{x})$ . During these simulations, the particle packing remains static. In reality this would imply a high confining pressure compared to capillary stress so that force balance remains satisfied on each particle [42]. For each imposed  $\mu$ , the capillary pressure field in the pore domain is characterized by the first four cumulants of its PDF via Eqs. (5.2). The results for condensation are displayed in Figs. 5-9, 5-10, 5-11 and 5-12 for mean, variance, skewness

and kurtosis, respectively. Similar to packing density  $\eta$ , capillary pressure is coarse grained and displayed for  $h = 0.90$  in Figs. 5-13, 5-14 for the mean and the variance, respectively. In addition, as an example, the PDFs for  $m_p$  for  $\ell_{cg} = \{4, 8, 10, 20\}$ ,  $\tilde{T} = 1.2$  and  $h = 0.90$  for all structures are shown in Fig. 5-15.

### 5.3.3 Liquid Texturing & Morphology

The formation and coalescence of liquid clusters for Type A granular packings were investigated. This was done through determining the number of clusters,  $n_c$  formed during condensation at each imposed  $\mu$  (see Fig. 5-19) as well as the volume of clusters,  $V_c$  in voxels (see Fig. 5-20). A cluster is defined as a set of at least 20, 26-connected voxels satisfying  $\rho \geq \rho_L$  where  $\rho_L$  is the normalized liquid density determined from isotherms displayed in Figs. 5-8. As an example, these liquid clusters are visualized in Fig. 5-21 for  $\lambda^A = 1.0$ ,  $\tilde{T} = 0.8$  and for  $h \in \{0.82, 0.84, 0.88, 0.90, 0.94, 0.98\}$ . Figs. 5-22 and 5-23 display density maps for  $\lambda^A = 1.0$  (at  $h = 0.91$ ) and  $\lambda^B = 0.20$  (at  $h = 0.82$ ) structures, respectively, providing insights into temperature dependent formation and growth of these liquid clusters.

### 5.3.4 Poromechanics of Unsaturated Media

The current approach to poromechanics of unsaturated porous media involves decomposing the pore space into liquid and gas phases with a distinct uniform pressure prevailing in each. Then an effective pressure is sought such that it captures the interactions of a fluid comprised of liquid and vapor acting independently on the pore solid wall. A natural candidate for such an effective pore pressure is the space-averaged pore pressure - that is the sum of the fluid pressure weighted by the pore volume fraction of each fluid phase. This is shown to be only valid assuming iso-deformation of the pore network [37]. The prevailing macroscopic constitutive modeling approach was proposed by Coussy [37]. It introduces Lagrangian saturation as a state variable that is associated with interfacial energy changes, independent of elastic energy required for deforming the solid matrix. On the other hand, the microporomechanics approach of Dormieux et al. [29, 44] requires same liquid and gas

morphology in the pore space to remain consistent. The statistical mechanics based fluid description outlined here along with the outlined discrete heterogeneous solid description provides a powerful tool to probe the mechanics of unsaturated porous continua. This differs from granular response and the re-arrangement of a set of particles as a consequence of net capillary forces [137, 136].

Previously, Monfared et al. [91] (see Chapter 3) proposed a method to impose an average pressure inside a pore domain  $\Omega_p$  in a discrete solid mechanics framework (Lattice Element Method) through an effective pore-pressure force field potential that takes advantage of the regularity of the lattice network and the fabric tensor of the pore domain. This pore pressure force field assumes full saturation in the pore domain, i.e.  $\rho(\vec{x}) = 1$ , which results in a uniform pore pressure field in  $\Omega_p$  with a PDF that follows a Dirac's delta function. In this case, the average stresses in  $\Omega_p$  utilizing Virial stress definition can be written as:

$$\langle \sigma \rangle_{\Omega_p} = -p\mathbf{1} = \frac{n_\ell^p}{2V_p} \langle r_{ij} F_i^{j,n} \vec{e}_n \otimes \vec{e}_n \rangle = \frac{1}{2V_p} \sum_{i=1}^{N_p} \sum_{j=1}^{N_i^b} r_{ij} F_i^{j,n} \vec{e}_n^i \otimes \vec{e}_n^j \quad (5.32)$$

where only central-forces are considered, i.e.  $\vec{F}_i^j = F_i^{j,n}$  and  $n_\ell^p$  denotes number of links in the pore domain. In a zeroth-order description of the microtexture,  $F_i^{j,n}$  and  $r_{ij}$  are considered to be independently distributed and thus not correlated [104, 7] which allows Eq. (5.32) to be expressed as  $\langle \sigma \rangle_{\Omega_p} = \frac{n_\ell^p}{2V_p} \langle r F^n \rangle \langle \vec{e}_n \otimes \vec{e}_n \rangle$ , leading to:

$$F_i^{j,n} = -\frac{6p V_p}{r_{ij} n_\ell^p} \quad (5.33)$$

It is important to note in this approach, the mechanical work due to the prevailing pressure in the pore domain is transferred onto the solid via nearest pore neighbors of a solid node. Eq. (5.33) addresses the fully saturated case where a uniform pressure prevails in the pore domain. In the unsaturated case however the temperature dependent behavior of a confined fluid is far from a Dirac's delta function as shown in Section 5.3.2 and for e.g. Fig. 5-15. Thus, any mechanics approach needs to take into account the local information carried by the capillary pressure field  $p(\vec{x})$  - specifically those pore nodes nearest to the solid wall

(nodes). This can be achieved by applying Eq. (5.33) not to the entire pore domain but to the (pore fluid) voxels in the vicinity of the solid wall. Thus, with Eq. (5.33) as its basis the local capillary pressure  $p_i \equiv p(\vec{x}_i)$  is utilized to determine the forces acting on the solid wall:

$$F_i^{j,n} = -\frac{6p_i a_0^3}{r_{ij} N_i^b} \quad \forall i \in \Omega_p \wedge j \in \Omega_s \quad (5.34)$$

To validate Eq. (5.34), the fully saturated limit case is considered. For a hollow sphere with inner radius  $a$  and outer radius  $b$  subjected to an internal uniform pressure  $p_i$  and an external uniform pressure  $p_o$  there exists an analytical solution due to Lamé [75] for the induced radial  $\sigma_{rr}$  and tangential  $\sigma_{\theta\theta}$  stresses:

$$\sigma_{rr} = \frac{p_o b^3 (r^3 - a^3)}{r^3 (a^3 - b^3)} + \frac{p_i a^3 (b^3 - r^3)}{r^3 (a^3 - b^3)} \quad (5.35)$$

$$\sigma_{\theta\theta} = \frac{p_o b^3 (2r^3 + a^3)}{2r^3 (a^3 - b^3)} - \frac{p_i a^3 (2r^3 + b^3)}{2r^3 (a^3 - b^3)} \quad (5.36)$$

where  $r$  denotes the distance from the inner radius. It is important to note that uniform pressures  $p_o$  and  $p_i$  imply full saturation, i.e.  $\rho(\vec{x}) = 1$  for  $\vec{x} \in \Omega_p$  and a Dirac's delta function for PDF of  $p(\vec{x})$  for  $\vec{x} \in \Omega_p$ . As such, this provides a platform to validate Eq. (5.34) against analytical solutions Eqs. (5.35). The results are shown in Fig. 5-18 with great agreement. The noise in numerical values in Fig. 5-18 is rooted in the discrete nature of the simulations. With this validation at hand, next the unsaturated case is explored by bringing together the capillary pressure simulations as outlined in Section 4.1 and local pore pressure force formulation in Eq. (5.34). To this end, the granular packing  $\lambda^B = 1$  with  $\eta = 0.50$  is turned into a porous solid by flipping pore and solid voxels. The structure is then discretized using a lattice spacing of  $a_0 = 1.0$  for both solid and fluid simulations. The temperature  $\tilde{T} = 1.2$ , chemical potential  $\mu$  of the fluid and entire volume  $V$  through  $\vec{\xi}^d(\vec{x}) = \vec{0}$  for  $\vec{x} \in \partial V$  are imposed. During condensation and for  $h \in \{0.8, 0.85, 0.88, 0.90\}$  the simulated pressure field  $p(\vec{x})$  and its first moment, i.e.  $m_p = \langle p(\vec{x}) \rangle_{\Omega_p}$  are imposed separately utilizing Eqs. (5.33) and (5.34), respectively. Through the discrete description of solids and utilizing Lattice Element Method (see Chapter 2), the induced stresses and

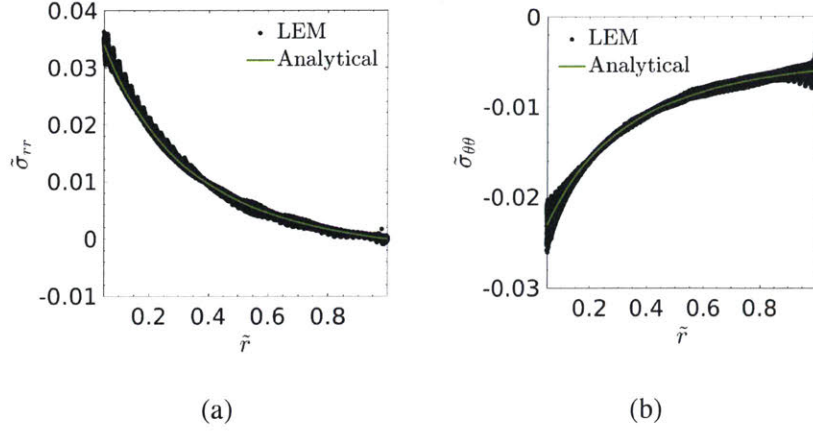


Figure 5-18: Radial -  $\tilde{\sigma}_{rr} = \sigma_{rr}/M_s$  - (5-18a) and tangential -  $\tilde{\sigma}_{\theta\theta} = \sigma_{\theta\theta}/M_s$  - stresses (5-18b) corresponding to Lamé’s problem calculated from analytical solutions and numerical simulations.  $M_s$  is the imposed isotropic indention modulus for the solid shell.

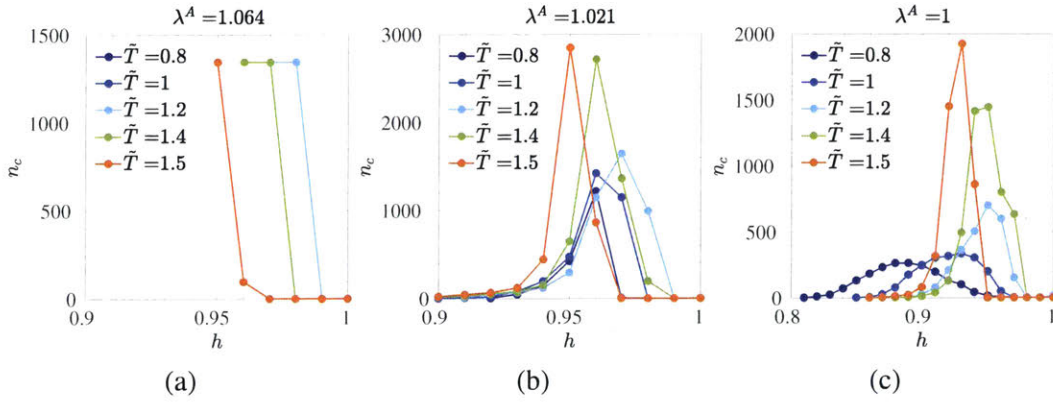


Figure 5-19: Number of clusters at different relative humidities for  $\lambda^A = 1.064$  (5-19a),  $\lambda^A = 1.021$  (5-19b) and  $\lambda^A = 1.0$ .

deformation are simulated. The objective is to examine the mechanics response of the solid as the local information from the capillary pressure field is lost through averaging operations.

## 5.4 Discussions

Criticality due to confinement is examined through determining capillary critical temperature  $T_{cc}$  for the disordered packings studied here. The shift in capillary critical points,  $\Delta T_c/T_c^{3D}$ , of all the considered disordered packings and for different lattice spacings, i.e.

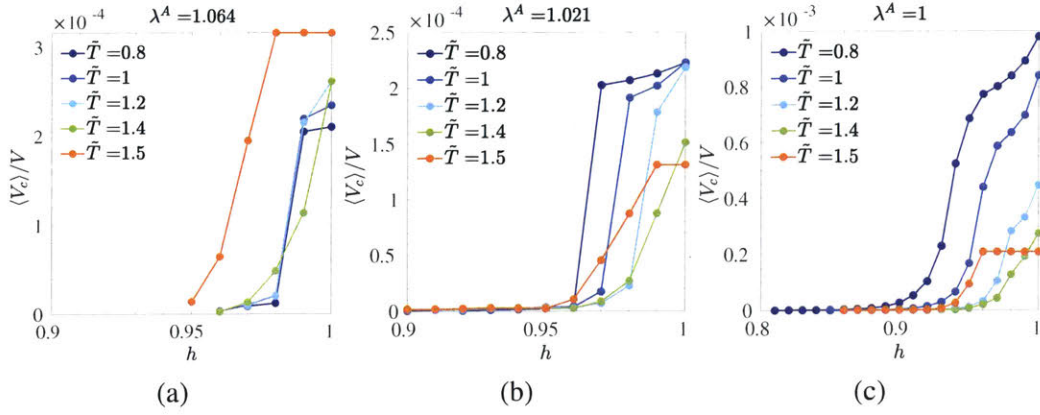


Figure 5-20: First moment of cluster volume,  $V_c$  (in voxels) normalized by the total simulation box volume  $V$  for  $\lambda^A = 1.064$  (5-20a),  $\lambda^A = 1.021$  (5-20b) and  $\lambda^A = 1.0$ .

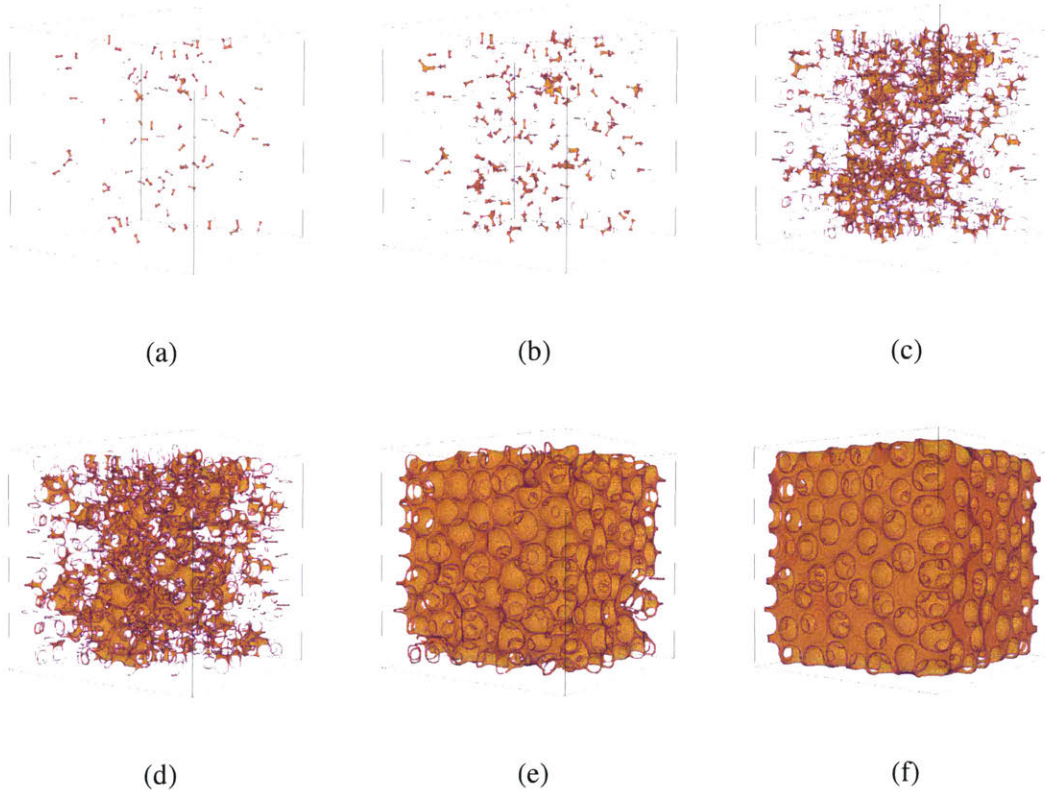


Figure 5-21: Visualizations for liquid clusters for  $\lambda^A = 1.0$ ,  $\tilde{T} = 0.80$  and for  $h = 0.82$  (5-21a),  $h = 0.84$  (5-21b),  $h = 0.88$  (5-21c),  $h = 0.90$  (5-21d),  $h = 0.94$  (5-21e) and  $h = 0.98$  (5-21f).

$a_0 \in \{0.25, 0.5, 1.0\}$ , are shown in Fig. 5-17. The results depart from the expected scaling  $\Delta T_c / T_c^{3D} \sim 2\sigma / \langle r_p \rangle$  which is thought to be independent of the nature of the adsorbate, the chemical nature of the absorbent and shape of the pore and inter-pore connections [33]. The

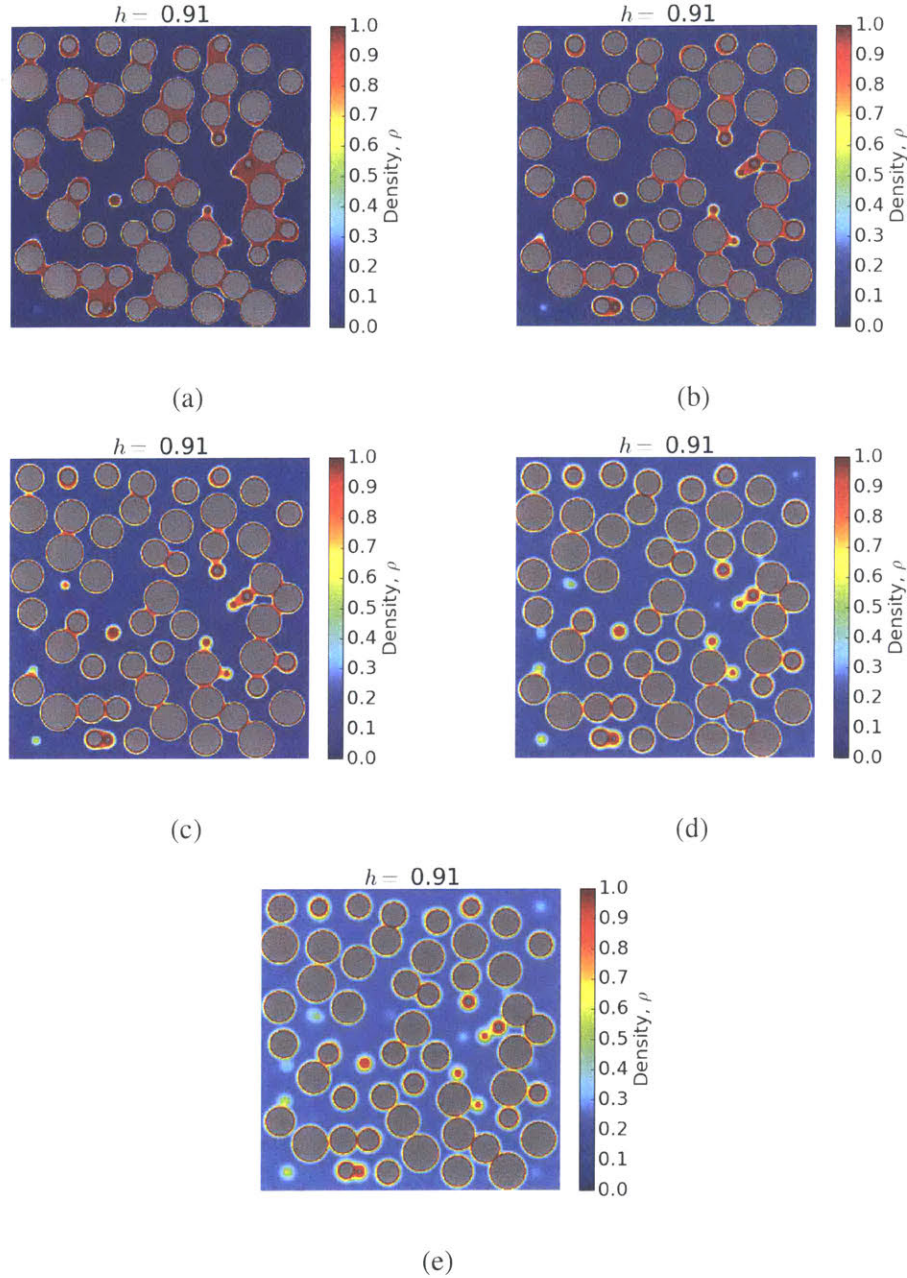


Figure 5-22: Cross-sections at  $z = 44$ ,  $\lambda^A = 1.0$ ,  $h = 0.91$  and for  $\tilde{T} = 0.8$  (5-22a),  $\tilde{T} = 1.0$  (5-22b),  $\tilde{T} = 1.2$  (5-22c),  $\tilde{T} = 1.4$  (5-22d) and  $\tilde{T} = 1.5$  (5-22e).

reported Coarse Grained Lattice Gas simulations in the literature also slightly depart from this one-to-one scaling. This is due to the coarse grained nature of the CGLG approach that does not account for thermal fluctuations compared to higher resolutions methods such as Grand Canonical Monte Carlo (GCMC). Our determination for the shift in critical temperature for cylindrical pores is consistent with those reported in the literature using the

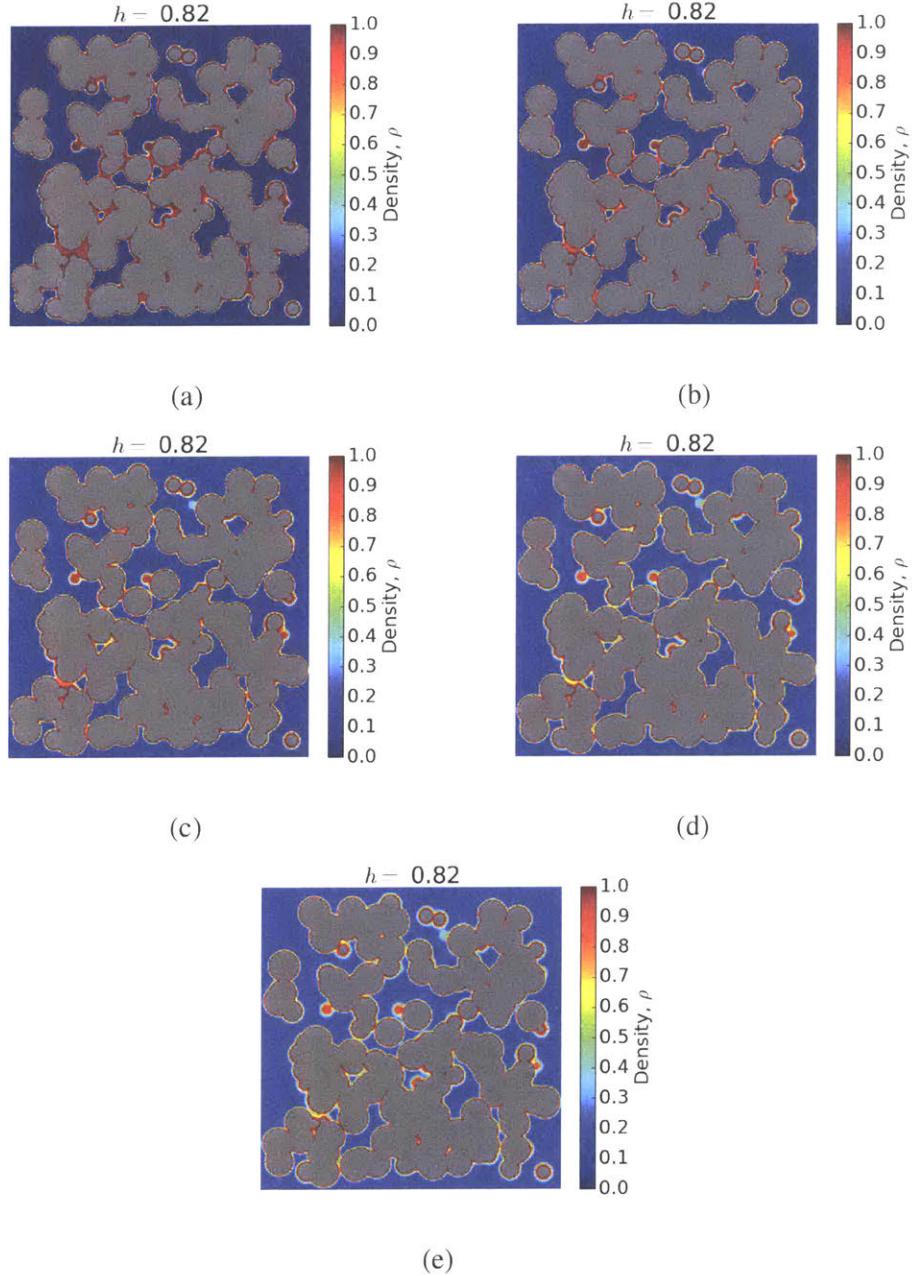


Figure 5-23: Cross-sections at  $z = 44$ ,  $\lambda^B = 0.20$ ,  $h = 0.82$  and for  $\tilde{T} = 0.8$  (5-23a),  $\tilde{T} = 1.0$  (5-23b),  $\tilde{T} = 1.2$  (5-23c),  $\tilde{T} = 1.4$  (5-23d) and  $\tilde{T} = 1.5$  (5-23e).

same method, i.e. CGLG (see Fig. 5-17). The departure of the granular packings from this scaling raises questions about its universality. Furthermore, one needs to ask if this scaling should be based on the first moment of pore size distribution  $\langle r_p \rangle$  or some other representation of the pore topology and pore morphology such as constricted pore radius. The established scaling  $\Delta T_c / T_c^{3D} \sim 2\sigma / \langle r_p \rangle$  is based on experiments and simulations on

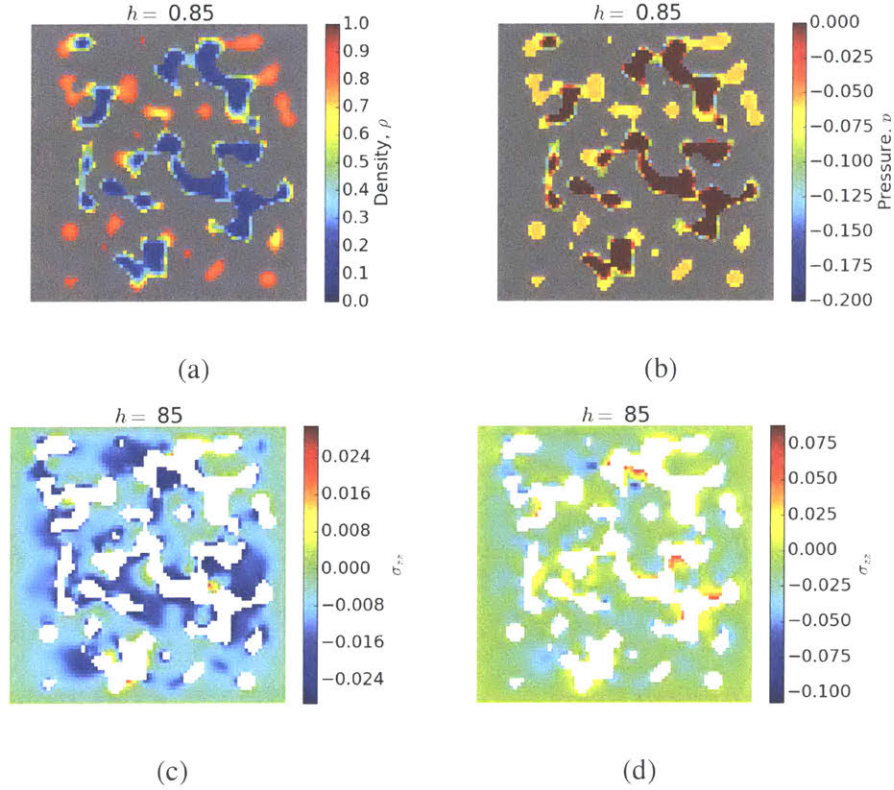


Figure 5-24: Cross-section at  $z = 40$  and for  $h = 0.85$  displaying normalized density (5-24a), capillary pressure (5-24b) and solid stresses  $\sigma_{zz}$  induced by  $\langle p \rangle$  (5-24c) and  $p(\vec{x})$  (5-24b).

very well defined porous materials, for example MCM-41 like cylindrical pores or vycor glass with a well-defined, sharp and narrow Gaussian pore size distribution. However, this is not the case with our granular packings given the wide range of pore size distributions (see Fig. 5-4) and considering its discrete nature, i.e. lacking a continuous solid matrix. The relationship between disorder parameter,  $\lambda$  and shift in capillary critical temperature  $\Delta T_c/T_c^{3D}$  depends on lattice spacing, i.e. size of the molecule, as expected. Although no conclusive observation can be made regarding the displayed results(see Fig. 5-17), there seems to be a trend that needs to be explored further on a larger set of structures while considering other metrics most relevant for characterizing the confinement induced by the underlying structure.

A curious result from examining the evolution of  $m_p$  with  $\tilde{\mu}$  for  $\tilde{T} = 1.5$  sheds light on critical behavior of fluids in confinement. If  $T_{cc}$  represents a true critical point, then one

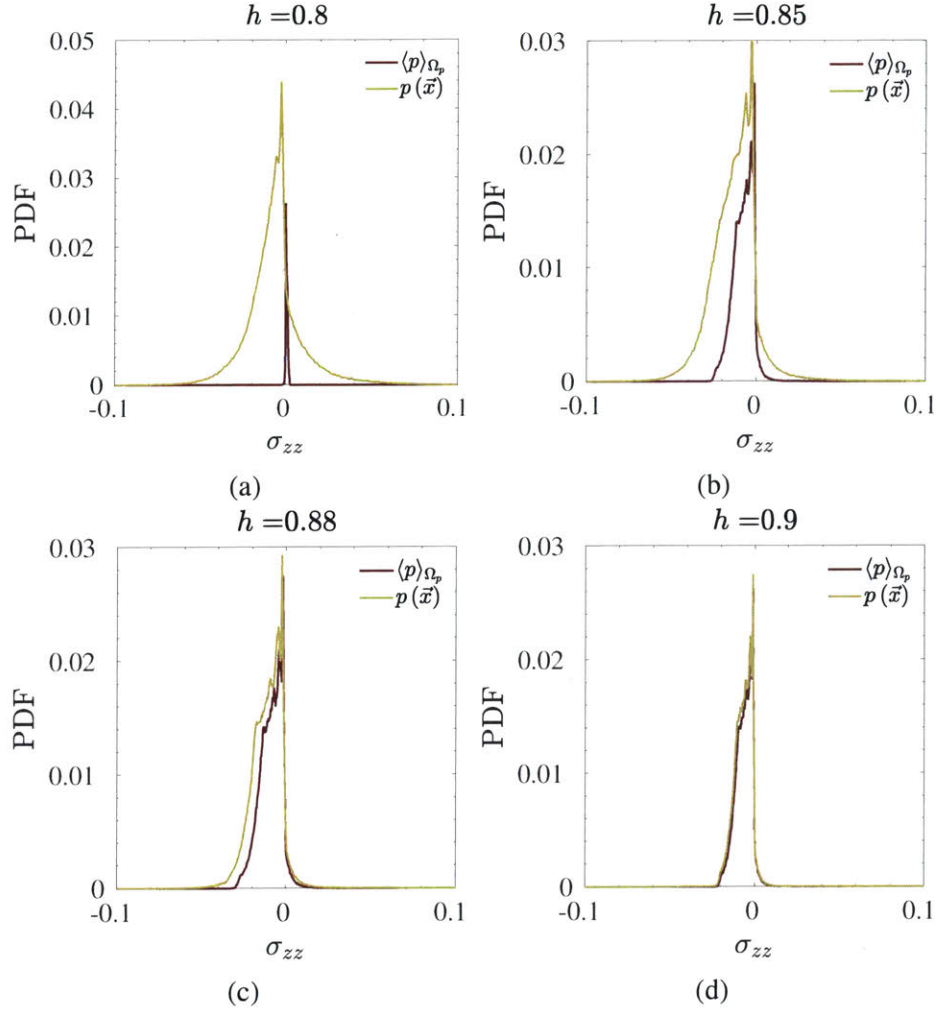
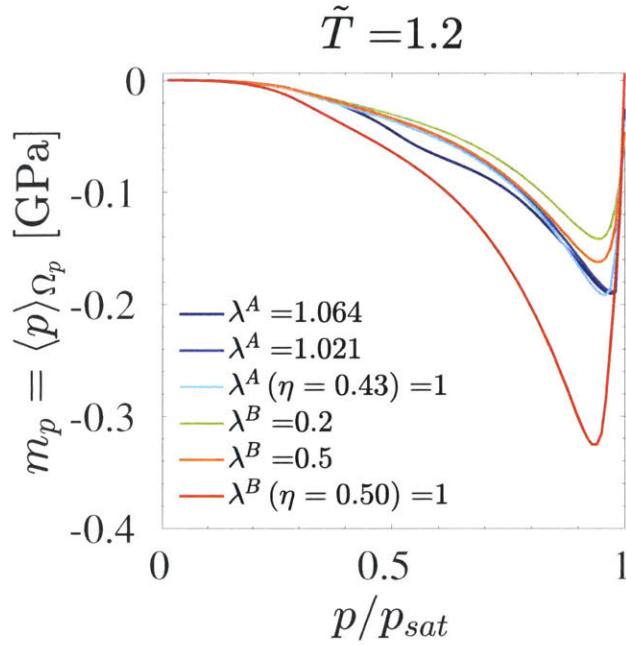


Figure 5-25: PDFs for solid stresses  $\sigma_{zz}$  induced by  $\langle p \rangle$  and  $p(\vec{x})$  for  $h = 0.8$  (5-25a),  $h = 0.85$  (5-25b),  $h = 0.88$  (5-25c) and  $h = 0.90$  (5-25d).

would expect no capillary pressure since liquid-gas interface should disappear. However, our results suggest that this may not be the case. The capillary critical point for all of the considered structures lies between  $1.4 < \tilde{T}_{cc} < 1.5$  however for  $\tilde{T}_{cc} > \tilde{T} = 1.5$ , there is a capillary pressure response for all the considered structures as shown through the first four cumulants of the capillary pressure field. (see Figs. 5-9, 5-10, 5-11 and 5-12).

The mean of capillary pressure field,  $m_p$ , as a function of  $\tilde{\mu} = \mu/w_{ff}$  displays a sharp transition for lower temperatures. As temperature increases, the evolution of  $m_p$  with  $\tilde{\mu}$  becomes more continuous (see Figs. 5-9). This is expected since as temperature increases and approaches  $T_{cc}$ , the liquid-gas transition become continuous and reversible (see Fig.



(a)

Figure 5-26: The mean,  $m_p$  evolution of capillary pressure field (in real units) with  $p/p_{sat} = \exp(\mu - \mu_{sat})/k_B T$  for different structures at  $\tilde{T} = 1.2$ .

5-8). The sharp liquid-gas transition at lower temperatures, as shown in Figs. 5-22 and 5-23, imply higher gradient of  $\rho(\vec{x})$  which is directly accounted for in Kortweg capillary stress tensor definition (see Eq. (5.27)). Interestingly, the effect of spatial disorder of particles is reflected in  $m_p$  and for  $\tilde{T} = 0.8$  and  $\lambda^A = 1.064$ . For this case, the evolution of  $m_p$  with  $\tilde{\mu}$  seems to remain almost constant for a range of  $\tilde{\mu}$  which is a departure from other structures and for higher temperatures. This is due to spatial arrangement of particles which hinders continuous nucleation, growth and coalescence of capillary bridges and liquid clusters as a result of the regular spacing between the particles. Furthermore, the effect of packing density is clearly highlighted in Fig. 5-26 for  $\tilde{T} = 1.2$ . In real units for the evolution of  $m_p$  with  $p/p_{sat} = \exp(\mu - \mu_{sat})/k_B T$ , it can be seen that for similar spatial disorder, i.e.  $\lambda^A(\eta = 0.43) = \lambda^B(\eta = 0.50) = 1.0$ , the  $m_p$  peaks at a lower pressure value for a higher packing density.

The variance of capillary pressure field,  $v_p$ , as a function of  $\tilde{\mu} = \mu/w_{ff}$  amplifies the effect of spatial arrangement of the particles relative to evolution of  $m_p$  discussed before

(see Figs. 5-10). This is most evident for Type A structures and  $\tilde{T} = 0.8$  for which the evolution of  $v_p$  with  $\tilde{\mu}$  shows multiple peaks for the ordered structure, i.e.  $\lambda^A = 1.064$ , followed by less pronounced peaks for  $\lambda^A = 1.021$  and a smooth evolution (no peaks) for  $\lambda^A = 1.0$  reminiscent of the computed  $g(r)$  for each one of these structures (see Fig. 5-2). Furthermore, as expected (and outlined before) variations in capillary pressure field near liquid-gas transition for lower temperatures are more pronounced. This is also reflected in Figs. 5-10. The skewness of capillary pressure field,  $s_p$ , remains negative and multi-modal for all temperatures, structures and  $\tilde{\mu}$ . Both  $s_p$  and  $\kappa_p$  seem to be most sensitive to the overlapping structures, i.e.  $\lambda^B = 0.20$  and  $\lambda^B = 0.5$  at  $\tilde{T} = 0.8$ .

The coarse-grained  $m_p$  (Fig. 5-13) and  $v_p$  (Fig. 5-14) display some fluctuations for  $\ell_{cg} < 20$  while converging for all structures and the range of considered temperatures around  $\ell_{cg} = 20$ . This length scale coincides with the length scale for which statistical descriptors for local packing density  $\eta$  start to converge for both structure types (see Figs. 5-5). As an example, at  $h = 0.90$  and  $\tilde{T} = 0.8$  the PDFs for  $m_p$  associated with  $\ell_{cg} \in \{4, 8, 10, 20\}$  are shown in Fig. 5-15. Even at such high relative humidity, the behavior of capillary pressure characterized here by its first moment clearly displays a length scale dependence. This is a reflection of the underlying microstructural features. For example multi-modal  $m_p$  peaks for  $\lambda^A$  is a manifestation of the ordered arrangement of spherical particles in space. As  $\ell_{cg}$  increases, the PDFs become less broad approaching a Gaussian distribution.

The liquid clustering analysis highlights the role of confinement in formation of liquid clusters. This is best illustrated via visualizations of two cross-sections ( $z = 44$ ) for  $\lambda^A = 1.0$  and  $\lambda^B = 0.20$  as shown in Figs. 5-22 and 5-23, respectively, for different  $\tilde{T}$ . Furthermore, quantitative analyses as shown in Figs. 5-19 and 5-20 for Type A structures highlights the role of disordered confinement and temperature in formation, growth and coalescence of clusters. Specifically, for  $\lambda^A = 1.064$ , the (reference) ordered granular packing, there are no clusters as defined in Section 5.3.3 for  $\tilde{T} < 1.2$ . For  $\tilde{T} \geq 1.2$  there is a sudden appearance of many clusters (see Fig. 5-19). The formation of these clusters becomes more gradual as disorder is increased (see Fig. 5-21 for visualization of liquid

clusters as a function of  $h$ ). Additionally, the role of temperature can be observed through more rapid formation and coalescence of clusters for higher temperature compared to the lower ones. Fig. 5-20 show the normalized cluster volumes displaying a more gradual increase in cluster volumes as disorder increases while indicating that percolation of liquid clusters occurs at a lower relative humidity  $h$  as disorder increases.

The local pore pressure force formulation presented in Section 5.3.4 provides the means for applying the mechanical work due to a pressure field onto the solid through the forces acting on the pore-solid wall. This method utilizes the Virial stress definition which bypasses the need for defining a surface and its normal typical of Cauchy stresses. It is also important to note that the computed capillary stress tensorial field satisfies equilibrium via Eq. 5.19. The solid's responses to a special case of effective pressure, i.e.  $\langle p(\vec{x}) \rangle$ , and pressure field  $p(\vec{x})$  is displayed in Figs. 5-24c and 5-24d for  $h = 0.85$ . The PDFs for  $\sigma_{zz}$  component of the solid stress tensor are plotted in Fig. 5-25 highlighting the contrasting response of the solid for the two presented pore pressure formulations at lower saturations. As saturation increases, the two PDFs approach each other which indicates that the first cumulant of the pressure field, i.e.  $\langle p(\vec{x}) \rangle$  carries sufficient information at high saturations. This sets the stage to re-formulate the poromechanics of unsaturated media in the osmotic ensemble through minimizing the osmotic potential that is a hybrid potential in which the solid is in isothermal-isobaric ensemble and the fluid is in the grand canonical ensemble [116, 87, 35].

## 5.5 Chapter Summary

The capillary pressure fields in disordered granular packings are studied. The results suggest strong fluctuations in local capillary pressure depending on the length scale which is very relevant for mechanics. Our results suggest that capillary critical temperature may not be a true critical point as evident by a capillary pressure response characterized by the cumulants of the capillary pressure field for temperatures greater than  $T_{cc}$ . Additionally, the universality of the scaling between the shift in capillary critical temperature and an

expression involving the size of the molecule and the mean pore radius,  $\langle r_p \rangle$ , is questioned. This is done through determining this scaling for granular packings exhibiting wide pore size distributions and lacking a continuous solid matrix. The response of capillary pressure field is shown to reflect the underlying disorder of the structure. This is most evident for  $\tilde{T} = 0.8$  and for the first two cumulants of the capillary pressure field. The role of disorder and temperature on liquid formation and coalescence is clearly highlighted. The results suggest that more clusters are formed as disorder increases while the rate of formation and coalescence seem to increase with temperature. Lastly, a local pore pressure force formulation is proposed to translate the mechanical work by the capillary pressure field into solid mechanics response. The proposed force field potential is validated in the limit case of full saturation. Lastly, its application suggest a significant departure between the solid's response to  $p(\vec{x})$  and  $\langle p(\vec{x}) \rangle$  for low saturation. This contrast disappears at higher saturations rendering a mean-field description of pressure field  $p(\vec{x})$  sufficient for capturing the induced solid deformation.

# Chapter 6

## Conclusions

### 6.1 Summary of Main Findings

The experimental advancements in characterizing highly heterogeneous porous solids by resolving the microstructure and the mechanics at high resolutions via advanced imaging techniques and small-scale mechanical testings call for development of new theoretical and computational tools to model and to predict the deformation of porous materials in response to various external loadings while incorporating the newly accessible information. This is the main objective of this thesis pursued via a discrete approach to poromechanics to overcome the limitations of mean-field theories of continuum micromechanics in capturing spatial variations of mechanical properties and limited to scale separability. In this vein, Lattice Element Method (LEM) provides a rigorous computational mechanics framework to study highly heterogeneous solids whether linear, non-linear, isotropic or anisotropic. This is done by capturing the mechanical interactions between material points in space. Its parallelization with Message Passing Interface (MPI) provides a powerful tool to probe elasticity [77, 90], poroelasticity [91, 90], fracture and failure properties [79, 80] of a range of materials. One needs to keep in mind the limitations of the current formulation to capture the full range of possible desired behaviors.

The statistical mechanics based formulation in Chapter 3 provides access to Biot poroelastic coefficients for highly heterogeneous solids. Specifically, It was shown that if formu-

lated properly, the grand canonical ensemble ( $\mu VT$ -ensemble) provide access to the tensor of Biot pore pressure coefficients,  $\mathbf{b}$ , while isothermal-isobaric ensemble ( $NPT$ -ensemble) permit determination of the Biot solid modulus,  $N$ . This discrete model is then validated after its implementation in LEM with a (global) pore pressure force field potential in the pore domain capturing the case of fully saturated pore, i.e. uniform pressure.

Chapter 4 brings together one of the main objective of this thesis that is to study real heterogeneous materials utilizing advanced imaging data, small-scale mechanics data and the developed theoretical (discrete) modeling and computational framework presented in Chapters 2 and 3. To this end, a methodology to calibrate and to validate effective interaction potentials of the solid constituents of a highly heterogeneous porous material in LEM is developed utilizing experimentally measured nanoindentation data and 3D computed tomography scans. Accounting for the spatial variations of elasticity are shown to be a necessary ingredient for capturing heavy-tails of measured indentation data. The Biot poroelastic coefficients for these scans are simulated in a forward modeling approach and are shown to generally follow a Stable distribution, a manifestation of interactions of many heavy-tailed PDFs representative of various physical quantities. Stress transmission highlights the distinct percolation paths in each scan due to underlying microtextural features while stress coarse-graining delineates the highly heterogeneous nature of the organic-shale materials examined and highlights the challenges involved in defining a representative elementary volume for continuum based analysis.

A statistical mechanics approach is employed in Chapter 5 to describe confined fluids. Utilizing disordered monodisperse granular packings, the capillary pressure field and how its affected by confinement as well as temperature is studied. The results raises questions with regards to capillary critical temperature representing a true critical point. Furthermore, the universality of the scaling between the shift in capillary critical temperature and an expression involving the size of the fluid molecule and the mean pore radius,  $\langle r_p \rangle$ , is questioned. Lastly, the mean-field description for pressure field, a especial case of effective stress concept in unsaturated poromechanics, is shown to be inaccurate at lower saturation

while sufficient for capturing the induced solid deformation at higher saturations.

## 6.2 Limitations & Future Perspectives

The implemented formulation for LEM utilizes a regular lattice for material discretization. Exploring other lattice-network combinations including irregular ones and characterizing the behavior of such discrete approach to solid mechanics would be very interesting. Especially given the limitations of the current formulation in capturing the range of transversely isotropic behavior (see Eq. (2.31)) and isotropic behavior beyond  $\nu = 0.25$ . It would be worthwhile to incorporate the evolution of comparable discrete methods that have addressed such restrictions such as peridynamics [114] and elastic networks [95] by for example including non-local interactions effects.

The discrete method developed for poroelasticity of heterogeneous materials provides the means to characterize the Biot poroelastic coefficients for any porous media of arbitrary heterogeneity while accounting for anisotropy. Similar to the elastic case [77], this method can be applied to disordered porous materials to explore how Biot poroelastic coefficients are affected by disorder.

The methodology presented in Chapter 4 provides the means to connect the simulation and experimental realms. The calibration of elastic content of a highly heterogeneous systems from experimental data paves the path for other studies on imported computed tomography scans including wave propagation, creep, failure and fracture behaviors.

The discrete fluid description outlined in Chapter 5 in conjunction with the discrete solid description in Chapter 2 provides a platform to study unsaturated poromechanics of highly heterogeneous materials. Also parallelized with MPI, this computational framework should be utilized to study a wide range of disordered confinements, fluid-solid interactions and temperatures to provide a comprehensive understanding of confined fluid behavior, fluid criticality, capillary condensation and liquid-gas phase transition as well as spatial

distribution of capillary pressure through characterizing capillary stress tensorial field.

# Appendix A

## Global to Local Coordinate Transformation

The local coordinate system for link  $0i$  -  $(\vec{e}_n^i, \vec{e}_b^i, \vec{e}_t^i)$  - is related to the global coordinate system -  $(\vec{e}_x, \vec{e}_y, \vec{e}_z)$  - as follows:

$$\vec{e}_n^i = P_{1i}^n \vec{e}_x + P_{2i}^n \vec{e}_y + P_{3i}^n \vec{e}_z \quad (\text{A.1})$$

$$\vec{e}_b^i = P_{1i}^b \vec{e}_x + P_{2i}^b \vec{e}_y + P_{3i}^b \vec{e}_z \quad (\text{A.2})$$

$$\vec{e}_t^i = P_{1i}^t \vec{e}_x + P_{2i}^t \vec{e}_y + P_{3i}^t \vec{e}_z \quad (\text{A.3})$$

$$\vec{e}_n^i = P_{1i}^n \vec{e}_x + P_{2i}^n \vec{e}_y + P_{3i}^n \vec{e}_z \quad (\text{A.4})$$

$$\vec{e}_b^i = P_{1i}^b \vec{e}_x + P_{2i}^b \vec{e}_y + P_{3i}^b \vec{e}_z \quad (\text{A.5})$$

$$\vec{e}_t^i = P_{1i}^t \vec{e}_x + P_{2i}^t \vec{e}_y + P_{3i}^t \vec{e}_z \quad (\text{A.6})$$

where  $P^{n,b,t}$  are given by:

$$\mathbf{P}^n = \begin{bmatrix} 1 & 0 & 0 & \frac{\sqrt{2}}{2} & -\frac{\sqrt{2}}{2} & 0 & 0 & \frac{\sqrt{2}}{2} & \frac{\sqrt{2}}{2} & \frac{\sqrt{3}}{3} & \frac{\sqrt{3}}{3} & -\frac{\sqrt{3}}{3} & -\frac{\sqrt{3}}{3} \\ 0 & 1 & 0 & \frac{\sqrt{2}}{2} & \frac{\sqrt{2}}{2} & \frac{\sqrt{2}}{2} & \frac{\sqrt{2}}{2} & 0 & 0 & \frac{\sqrt{3}}{3} & \frac{\sqrt{3}}{3} & \frac{\sqrt{3}}{3} & \frac{\sqrt{3}}{3} \\ 0 & 0 & 1 & 0 & 0 & \frac{\sqrt{2}}{2} & -\frac{\sqrt{2}}{2} & \frac{\sqrt{2}}{2} & -\frac{\sqrt{2}}{2} & \frac{\sqrt{3}}{3} & -\frac{\sqrt{3}}{3} & -\frac{\sqrt{3}}{3} & \frac{\sqrt{3}}{3} \end{bmatrix} \quad (\text{A.7})$$

$$\mathbf{P}^b = \begin{bmatrix} 1 & 0 & 0 & \frac{\sqrt{2}}{2} & -\frac{\sqrt{2}}{2} & 0 & 0 & \frac{\sqrt{2}}{2} & \frac{\sqrt{2}}{2} & \frac{\sqrt{3}}{3} & \frac{\sqrt{3}}{3} & -\frac{\sqrt{3}}{3} & -\frac{\sqrt{3}}{3} \\ 0 & 1 & 0 & \frac{\sqrt{2}}{2} & \frac{\sqrt{2}}{2} & \frac{\sqrt{2}}{2} & \frac{\sqrt{2}}{2} & 0 & 0 & \frac{\sqrt{3}}{3} & \frac{\sqrt{3}}{3} & \frac{\sqrt{3}}{3} & \frac{\sqrt{3}}{3} \\ 0 & 0 & 1 & 0 & 0 & \frac{\sqrt{2}}{2} & -\frac{\sqrt{2}}{2} & \frac{\sqrt{2}}{2} & -\frac{\sqrt{2}}{2} & \frac{\sqrt{3}}{3} & -\frac{\sqrt{3}}{3} & -\frac{\sqrt{3}}{3} & \frac{\sqrt{3}}{3} \end{bmatrix} \quad (\text{A.8})$$

$$\mathbf{P}^t = \begin{bmatrix} 0 & 0 & 0 & 0 & 0 & 1 & 1 & 0 & 0 & \frac{\sqrt{6}}{6} & -\frac{\sqrt{6}}{6} & \frac{\sqrt{6}}{6} & -\frac{\sqrt{6}}{6} \\ 0 & 0 & 1 & 0 & 0 & 0 & 0 & 1 & 1 & \frac{\sqrt{6}}{6} & -\frac{\sqrt{6}}{6} & -\frac{\sqrt{6}}{6} & \frac{\sqrt{6}}{6} \\ 1 & 1 & 0 & 1 & 1 & 0 & 0 & 0 & 0 & -\frac{\sqrt{6}}{3} & -\frac{\sqrt{6}}{3} & -\frac{\sqrt{6}}{3} & -\frac{\sqrt{6}}{3} \end{bmatrix} \quad (\text{A.9})$$

## Appendix B

# Nodal Displacements for Uniform Imposed Deformation

For a uniform deformation, the nodal displacements of a lattice can be obtained as follows:

$$\Delta^n = \begin{bmatrix} 1 & 0 & 0 & \frac{\sqrt{2}}{2} & \frac{\sqrt{2}}{2} & 0 & 0 & \frac{\sqrt{2}}{2} & \frac{\sqrt{2}}{2} & \frac{\sqrt{3}}{3} & \frac{\sqrt{3}}{3} & \frac{\sqrt{3}}{3} & \frac{\sqrt{3}}{3} \\ 0 & 1 & 0 & \frac{\sqrt{2}}{2} & \frac{\sqrt{2}}{2} & \frac{\sqrt{2}}{2} & \frac{\sqrt{2}}{2} & 0 & 0 & \frac{\sqrt{3}}{3} & \frac{\sqrt{3}}{3} & \frac{\sqrt{3}}{3} & \frac{\sqrt{3}}{3} \\ 0 & 0 & 1 & 0 & 0 & \frac{\sqrt{2}}{2} & \frac{\sqrt{2}}{2} & \frac{\sqrt{2}}{2} & \frac{\sqrt{2}}{2} & \frac{\sqrt{3}}{3} & \frac{\sqrt{3}}{3} & \frac{\sqrt{3}}{3} & \frac{\sqrt{3}}{3} \\ 0 & 0 & 0 & \frac{\sqrt{2}}{2} & -\frac{\sqrt{2}}{2} & 0 & 0 & 0 & 0 & \frac{\sqrt{3}}{3} & \frac{\sqrt{3}}{3} & -\frac{\sqrt{3}}{3} & -\frac{\sqrt{3}}{3} \\ 0 & 0 & 0 & 0 & 0 & 0 & 0 & \frac{\sqrt{2}}{2} & -\frac{\sqrt{2}}{2} & \frac{\sqrt{3}}{3} & -\frac{\sqrt{3}}{3} & \frac{\sqrt{3}}{3} & -\frac{\sqrt{3}}{3} \\ 0 & 0 & 0 & 0 & 0 & \frac{\sqrt{2}}{2} & -\frac{\sqrt{2}}{2} & 0 & 0 & \frac{\sqrt{3}}{3} & -\frac{\sqrt{3}}{3} & -\frac{\sqrt{3}}{3} & \frac{\sqrt{3}}{3} \end{bmatrix} \quad (\text{B.1})$$

$$\Delta^b = \begin{bmatrix} 0 & 0 & 0 & -\frac{\sqrt{2}}{2} & \frac{\sqrt{2}}{2} & 0 & 0 & \frac{\sqrt{2}}{2} & -\frac{\sqrt{2}}{2} & \frac{\sqrt{2}}{2} & \frac{\sqrt{2}}{2} & -\frac{\sqrt{2}}{2} & -\frac{\sqrt{2}}{2} \\ 0 & 0 & 0 & \frac{\sqrt{2}}{2} & -\frac{\sqrt{2}}{2} & -\frac{\sqrt{2}}{2} & \frac{\sqrt{2}}{2} & 0 & 0 & -\frac{\sqrt{2}}{2} & -\frac{\sqrt{2}}{2} & \frac{\sqrt{2}}{2} & \frac{\sqrt{2}}{2} \\ 0 & 0 & 0 & 0 & 0 & \frac{\sqrt{2}}{2} & -\frac{\sqrt{2}}{2} & -\frac{\sqrt{2}}{2} & \frac{\sqrt{2}}{2} & 0 & 0 & 0 & 0 \\ 0 & -1 & 0 & -\frac{\sqrt{2}}{2} & -\frac{\sqrt{2}}{2} & 0 & 0 & 0 & 0 & \frac{\sqrt{2}}{2} & \frac{\sqrt{2}}{2} & \frac{\sqrt{2}}{2} & \frac{\sqrt{2}}{2} \\ 0 & 0 & 1 & 0 & 0 & 0 & 0 & \frac{\sqrt{2}}{2} & \frac{\sqrt{2}}{2} & \frac{\sqrt{2}}{2} & \frac{\sqrt{2}}{2} & -\frac{\sqrt{2}}{2} & \frac{\sqrt{2}}{2} \\ 0 & 0 & 0 & 0 & 0 & -\frac{\sqrt{2}}{2} & -\frac{\sqrt{2}}{2} & 0 & 0 & -\frac{\sqrt{2}}{2} & \frac{\sqrt{2}}{2} & -\frac{\sqrt{2}}{2} & \frac{\sqrt{2}}{2} \end{bmatrix} \quad (\text{B.2})$$

$$\Delta^t = \begin{bmatrix} 0 & 0 & 0 & 0 & 0 & 0 & 0 & 0 & 0 & \frac{\sqrt{6}}{6} & -\frac{\sqrt{6}}{6} & -\frac{\sqrt{6}}{6} & \frac{\sqrt{6}}{6} \\ 0 & 0 & 0 & 0 & 0 & 0 & 0 & 0 & 0 & \frac{\sqrt{6}}{6} & -\frac{\sqrt{6}}{6} & -\frac{\sqrt{6}}{6} & \frac{\sqrt{6}}{6} \\ 0 & 0 & 0 & 0 & 0 & 0 & 0 & 0 & 0 & -\frac{\sqrt{6}}{3} & \frac{\sqrt{6}}{3} & \frac{\sqrt{6}}{3} & -\frac{\sqrt{6}}{3} \\ 0 & 0 & 0 & 0 & 0 & 1 & 1 & 0 & 0 & \frac{\sqrt{6}}{6} & -\frac{\sqrt{6}}{6} & \frac{\sqrt{6}}{6} & -\frac{\sqrt{6}}{6} \\ 0 & 0 & 0 & 0 & 0 & 1 & -1 & 0 & 0 & \frac{\sqrt{6}}{6} & \frac{\sqrt{6}}{6} & -\frac{\sqrt{6}}{6} & -\frac{\sqrt{6}}{6} \\ 0 & 0 & 1 & 0 & 0 & 0 & 0 & 1 & -1 & \frac{\sqrt{6}}{6} & \frac{\sqrt{6}}{6} & \frac{\sqrt{6}}{6} & \frac{\sqrt{6}}{6} \end{bmatrix} \quad (\text{B.3})$$

# Appendix C

## Hill Concentration Tensor

The generalized Hill concentration tensor can be defined as (see for e.g. [134])

$$P_{ijkl} = - \left( \frac{\partial^2}{\partial x_j \partial x_l} \int_{\Omega} G_{ik}(\underline{x} - \underline{x}') d\Omega \right)_{(ij)(kl)} \quad (\text{C.1})$$

where (ij)(kl) indicates symmetrization and  $G_{ij}(\underline{x} - \underline{x}')$  is the  $2^{nd}$  order Green's tensor for generalized linear, elastic, anisotropic media that expresses displacement at point  $\underline{x}$  due to a Dirac delta type point force at  $\underline{x}'$ . For a transversely isotropic medium, the solution for Green's function can be found in [96]. Note that  $\mathbb{P}$  is positive definite and exhibits both major and minor symmetries. In a different form, Laws [81] expressed the generalized Hill concentration as follows:

$$P_{ijkl} = \frac{1}{16} (\mathcal{M}_{kijkl} + \mathcal{M}_{kjil} + \mathcal{M}_{lijk} + \mathcal{M}_{ljik}) \quad (\text{C.2})$$

with;

$$\mathcal{M}_{kijl} = \int_{S(\underline{\tilde{\omega}})} \frac{a_1 a_2 a_3}{(a_1^2 \tilde{\omega}_1^2 + a_2^2 \tilde{\omega}_2^2 + a_3^2 \tilde{\omega}_3^2)^{3/2}} \tilde{\Gamma}_{kj}^{-1}(\underline{\tilde{\omega}}) \tilde{\omega}_i \tilde{\omega}_j dS_{\tilde{\omega}} \quad (\text{C.3})$$

parameters  $a_1, a_2, a_3$  are geometric degrees of freedom that constraint the topology of an ellipsoid,  $dS_{\tilde{\omega}}$  is the surface element of an unit ellipsoid with components  $\tilde{\omega}_1, \tilde{\omega}_2, \tilde{\omega}_3$ , and  $\tilde{\Gamma}_{ik}(\underline{\tilde{\omega}}) = C_{ijkl} \tilde{\omega}_j \tilde{\omega}_l$  is known as the Christoffel matrix. One may be able to derive the explicit expressions for (C.1) and (C.2), depending on the elastic symmetry of the background medium, as well as the orientation and aspect ratio associated with the inclusion. In what

follows, we will present two well-known special cases; first the solution for a spheroidal inclusion embedded in an isotropic medium and then the solution for a spherical inclusion embedded in a transversely isotropic matrix.

## C.1 Spheroidal Inclusion in an Isotropic Medium

The simplest expression for Hill concentration tensor is that of a spheroidal inclusion embedded in an isotropic medium. It reads as follows (see e.g.[44]):

$$\mathbb{P} = \frac{\tilde{\alpha}}{3K}\mathbb{J} + \frac{\tilde{\beta}}{2G}\mathbb{K} \quad (\text{C.4})$$

where:

$$\tilde{\alpha} = \frac{3K}{3K + 4G} \quad (\text{C.5})$$

$$\tilde{\beta} = \frac{6(K + 2G)}{5(3K + 4G)} \quad (\text{C.6})$$

with  $K$  and  $G$  denoting the bulk and shear moduli of the background isotropic matrix, respectively. As a reminder,  $\mathbb{J} = J_{ijkl} = \frac{1}{3}(\delta_{ij}\delta_{kl})$  and  $\mathbb{K} = \mathbb{I} - \mathbb{J}$ .

## C.2 Spheroidal Inclusion in a Transversely Isotropic Medium

Evaluation of  $\tilde{\Gamma}_{ik}(\underline{\tilde{\omega}}) = C_{ijkl}\tilde{\omega}_j\tilde{\omega}_l$  in (C.3) can be performed by the following matrix operation:

$$[\tilde{\Gamma}] = [\tilde{\omega}][C][\tilde{\omega}]^T \quad (\text{C.7})$$

where  $[\dots]^T$  stands for transpose. Writing  $\underline{\tilde{\omega}}$  in matrix form:

$$[\tilde{\omega}] = \begin{bmatrix} \tilde{\omega}_1 & 0 & 0 & \frac{1}{2}\tilde{\omega}_2\sqrt{2} & 0 & \frac{1}{2}\tilde{\omega}_2\sqrt{2} \\ 0 & \tilde{\omega}_2 & 0 & \frac{1}{2}\tilde{\omega}_1\sqrt{2} & \frac{1}{2}\tilde{\omega}_3\sqrt{2} & 0 \\ 0 & 0 & \tilde{\omega}_3 & 0 & \frac{1}{2}\tilde{\omega}_2\sqrt{2} & \frac{1}{2}\tilde{\omega}_1\sqrt{2} \end{bmatrix} \quad (\text{C.8})$$

with the unit vector  $\underline{\tilde{\omega}}$  in spherical coordinates [57];  $\theta \in [0, \pi]$  and  $\phi \in [0, 2\pi]$ , being defined

as:

$$\tilde{\omega}_1 = \sin \theta \cos \phi \quad (\text{C.9})$$

$$\tilde{\omega}_2 = \sin \theta \sin \phi \quad (\text{C.10})$$

$$\tilde{\omega}_3 = \cos \theta \quad (\text{C.11})$$

the none-zero terms in (C.2) and (C.3) lead to line integrals:  $\xi = \cos \theta$  and  $d\xi = -\sin \theta d\theta$  which can be evaluated numerically. Finally, in Voigt's notation the non-zero components of  $\mathbb{P}$  reads [57]:

$$P_{11} = \frac{1}{16} \int_{-1}^1 \frac{(\xi^2 - 1)(-8\xi^4 C_{33} C_{44} - 3\xi^4 C_{12} C_{33} - 2\xi^4 C_{13}^2 + 3\xi^4 C_{12} C_{44} \dots}{D_1} \dots \frac{\dots - 5\xi^4 C_{11} C_{44} + 5\xi^4 C_{11} C_{33} - 4\xi^4 C_{13} C_{44} - 6\xi^2 C_{44}^2 + 6\xi^4 C_{44}^2 \dots}{D_1} \dots \frac{\dots + 4\xi^2 C_{13} C_{44} + 3\xi^2 C_{12} C_{33} - 5\xi^2 C_{11} C_{33} - 6\xi^2 C_{12} C_{44} + 2\xi^2 C_{13}^2 + \dots}{D_1} \dots \frac{\dots 10\xi^2 C_{11} C_{44} + 3C_{12} C_{44} - 5C_{11} C_{44}}{D_1} d\xi \quad (\text{C.12})$$

$$P_{12} = -\frac{1}{16} \int_{-1}^1 \frac{(\xi - 1)^2 (\xi + 1)^2 (C_{12} C_{44} - \xi^2 C_{12} C_{44} + \xi^2 C_{12} C_{33} + C_{11} C_{44} \dots)}{D_1} \dots \frac{\dots - \xi^2 C_{11} C_{44} + \xi^2 C_{11} C_{33} - 2\xi^2 C_{13}^2 - 4\xi^2 C_{13} C_{44} - 2\xi^2 C_{44}^2}{D_1} d\xi \quad (\text{C.13})$$

$$P_{13} = -\frac{1}{4} (C_{13} + C_{44}) \int_{-1}^1 \frac{\xi^2 (\xi^2 - 1)}{D_2} d\xi \quad (\text{C.14})$$

$$P_{33} = \frac{1}{2} \int_{-1}^1 \frac{\xi^2 (-C_{11} + C_{11} \xi^2 - C_{44} \xi^2)}{D_2} d\xi \quad (\text{C.15})$$

$$\begin{aligned}
P_{44} = & -\frac{1}{16} \int_{-1}^1 \frac{(3\xi^2 C_{11}^2 - 2\xi^6 C_{13}^2 - C_{11}^2 - 4\xi^6 C_{11} C_{44} - 8\xi^6 C_{13} C_{44} - \dots}{D_1} \\
& \frac{\dots 4\xi^6 C_{33} C_{44} + 3\xi^6 C_{11} C_{33} - 3\xi^4 C_{11}^2 + C_{11} C_{22} + \xi^6 C_{11}^2 - \xi^6 C_{11} C_{12} - \dots}{D_1} \\
& \frac{\dots \xi^6 C_{12} C_{33} + 4\xi^4 C_{12} C_{13} - 2\xi^2 C_{12} C_{13} + 2\xi^6 C_{11} C_{13} + \dots}{D_1} \\
& \frac{\dots 2\xi^4 C_{13}^2 + \xi^4 C_{12} C_{33} + 8\xi^4 C_{11} C_{44} - 3\xi^4 C_{11} C_{33} - 4\xi^2 C_{11} C_{44} + \dots}{D_1} \\
& \frac{\dots 8\xi^4 C_{13} C_{44} - 4\xi^4 C_{11} C_{13} + 3\xi^4 C_{11} C_{12} - \dots}{D_1} \\
& \frac{\dots 3\xi^2 C_{11} C_{12} - 2\xi^6 C_{12} C_{13} + 2\xi^2 C_{11} C_{13})}{D_1} d\xi
\end{aligned} \tag{C.16}$$

where:

$$D_1 = (\xi^2 C_{11} - C_{11} - 2\xi^2 C_{44} - \xi^2 C_{12} + C_{12})(D_2) \tag{C.17}$$

$$\begin{aligned}
D_2 = & -\xi^4 C_{33} C_{44} + 2\xi^2 C_{13} C_{44} - \xi^2 C_{11} C_{33} - 2\xi^4 C_{13} C_{44} + \xi^4 C_{11} C_{33} \dots \\
& \dots + 2\xi^2 C_{11} C_{44} + \xi^2 C_{13}^2 - \xi^4 C_{11} C_{44} - \xi^4 C_{13}^2 - C_{11} C_{44}
\end{aligned} \tag{C.18}$$

# Bibliography

- [1] S. Abedi, M. Slim, R. Hofmann, T. Bryndzia, and F.-J. Ulm. Nanochemo-mechanical signature of organic-rich shales: a coupled indentation-edx analysis. Acta Geotech., 11:559–572, 2016.
- [2] Y.N. Abousleiman, K.L. Hull, Y. Han, G. Al-Muntasheri, P. Hosemann, S. Parker, and C.B. Howard. The granular and polymer composite nature of kerogen-rich shale. Acta Geotech., 11(3), 2016. 573-594.
- [3] R. Affes, J.-Y. Delenne, R. Monerie, F Radjai, and V. Topin. Tensile strength and fracture of cemented granular aggregates. Eur. Phys. J.E Soft Matter, 35, 2012.
- [4] K. Aleksandrov and T. Ryzhova. Elastic properties of rock-forming minerals. li layered silicates. Bull. USSR. Acad. Sci. Geophys. Ser., 9, 1961.
- [5] L. Anand. 2014 drucker medal paper: A derivation of the theory of linear poroelasticity from chemoelasticity. J. Appl. Mech., 82, 2015.
- [6] D.M. Anderson and G.B. McFadden. Diffuse-interface methods in fluid mechanics. Technical Report NISTIR 6018, U.S. Department of Commerce, Gathersburg, MD, April 1997.
- [7] E. Azema and F. Radjai. Internal structure of inertial granular flows. Phys. Rev. Lett., 112(7), 2014.
- [8] K.-J. Bathe. Finite Element Procedure. Prentice Hall, 2014.
- [9] A.S. Baumgarten and K. Kamrin. A general fluid-sediment mixture model and constitutive theory validated in many flow regimes. J Fluid Mech., 861:721–764, 2019.
- [10] Y. Beneviste. A new approach to the application of mori-tanaka’s theory in composite materials. Mech. Mater., 6(2), 1987.
- [11] M.J. Beran. Statistical Continuum Theories. J. Wiley, 1968.
- [12] F. Beroz, L.M. Jawerth, S. Munster, D.A. Weitz, and C.P. Broedersz. Physical limits to biomechanical sensing in disordered fibre network. Nat. Comm., 2017.

- [13] J.G. Berryman. Bounds and self-consistent estimates for elastic constants of random polycrystals with hexagonal, trigonal, and tetragonal symmetries. J. Mech. Phys. Solids, 53(10), 2005.
- [14] J. Berthouneau, O. Grauby, M. Abuhaikal, R. J.-M. Pellenq, F.-J. Ulm, and H. Van Damme. Evolution of organo-clay composites with respect to thermal maturity in type ii organic-rich source rocks. Geochim. Cosmochim. Acta, 195:68–83, 2016.
- [15] S. Bhattacharya and K.E. Gubbins. Fast method for computing pore size distributions of model materials. Langmuir, 22(18):7726–7731, 2006.
- [16] M.A. Biot. General theory of three-dimensional consolidation. J. Appl. Phys., 12(2), 1941.
- [17] M.A. Biot and D. Willis. The elastic coefficients of the theory of consolidation. J. Appl. Mech., 24, 1957.
- [18] A.W. Bishop and G.E. Blight. Some aspects of effective stress in saturated and partly saturated solids. Géotechnique, 13:177–197, 1963.
- [19] L. Bocquet, E. Charlaix, S. Ciliberto, and J. Crassous. Moisture-induced ageing in granular media and the kinetics of capillary condensation. Nature, 396, 1998. 735-737.
- [20] J.E.Jr. Bolander and S. Saito. Fracture analyses using spring networks with random geometry. Eng. Fract. Mech., 61(5):569–591, 1998.
- [21] P. Bonnaud, Q. Ji, B. Coasne, R. J.-M. Pellenq, and K. Van Vilet. Thermodynamics of water confined in porous calcium-silicate-hydrates. Langmuir, 28(31):11422–11432, 2012.
- [22] R.I. Borja and J.A. White. Conservation laws for coupled hydromechanical processes in unsaturated porous media: theory and implementation. Mechanics of Unsaturated Geomaterials, 2010. L.Laloui, ed., John Wiley and Sons, New York.
- [23] T. Bourbié, O. Coussy, and B. Zinszner. Acoustics of Porous Media. TECHNIP, 1987.
- [24] C. Bousige, C.M. Ghimbeu, C. Vix-Guterl, A.E. Pomerantz, A. Suleimenova, G. Vaughan, G. Garbarino, M. Feygenson, C. Wildgruber, F.-J. Ulm, R.-J.M. Pellenq, and B. Coasne. Realistic molecular model of kerogen’s nanostructure. Nat. Mat., 15:576–582, 2016.
- [25] L. Brochard, M. Vandamme, and R.J.-M. Pellenq. Poromechanics of microporous media. J. Mech. Phys. Solids, 60, 2012.
- [26] B. Budiansky. On the elastic moduli for some heterogeneous materials. J. Mech. Phys. Solids, 13, 1965.

- [27] J.W. Cahn and J.E. Hilliard. Free energy of a nonuniform system. i. interfacial free energy. J. Chem. Phys., 28(2), 1958.
- [28] G.T. Charras, J.C. Yarrow, M.A. Horton, L. Mahadevan, and T.J. Mitchison. Non-equilibration of hydrostatic pressure in blebbign cells. Nature, 435(7040), 2005. 365-369.
- [29] X. Chateau and L. Dormieux. Micromechanics of saturated and unsaturated porous media. Int. J. Numer. Anal. Methods Geomech., 26:831–844, 2002.
- [30] J. Christoffersen, M. Mehrabadi, and S. Nemat-Nasser. A micro-mechanical description of granular material behavior. J. Appl. Mech., 48(2):339–344, 1984.
- [31] B. Coasne, F. Di Renzo, A. Galarneua, and R.J.M. Pellenq. Adsorption of simple fluid on silica surface and nanopore: effect of surface chemistry and pore shape. Langmuir, 24, 2008. 7285-7293.
- [32] B. Coasne, A. Galarneau, F. Di Renzo, and R.J.M. Pellenq. Intrusion and retraction of fluids in nanopores: effect of morphological heterogeneity. J. Phys. Chem. C, 113, 2009. 1953-1962.
- [33] B. Coasne, A. Galarneau, R.J.-M. Pellenq, and F. Di Renzo. Adsorption, intrusion and freezing in porous silica: the view from the nanoscale. Chem. Soc. Rev., 42, 2013. 4141-4171.
- [34] G. Constantinidies, K.S. Ravi Chandran, F.-J. Ulm, and K.J. Van Vilet. Grid indentation analysis of composite microstructure and mechanics: Principles and validation. Mater. Sci. Eng. A., 430(1-2):189–202, 2006.
- [35] F.-X. Coudert, A. Boutin, M. Jeffroy, C. Mellot-Draznieks, and A. Fuchs. Thermodynamic methods and models to study flexible meta-organic frameworks. ChemPhysChem, 12(2):247–258, 2011.
- [36] O Coussy. Mechanics of porous continua. Wiley and Sons, Chichester, 1995.
- [37] O. Coussy. Revisiting the constitutive equations of unsaturated porous solids using a lagrangian saturation concept. Int. J. Numer. Anal. Methods Geomech., 31:1675–1694, 2007.
- [38] O Coussy. Mechanics and physics of porous solids. Wiley and Sons, Chichester, 2010.
- [39] S.C. Cowin. Bone fluid poroelasticity. Poromechanics, A tribute to M.A. Biot (Proceedings of the Biot conference on poromechannics) ed. By J.-F. Thimus et al., Balkema, 1998.
- [40] A. Deirieh, J.A. Ortega, and F.-J. Ulm. Nanochemomechanical assessment of shale: a coupled wds-indentation analysis. Acta Geotech., 7(4):271–295, 2012.

- [41] A. Delafargue and F.-J. Ulm. Explicit approximations of the indentation modulus of elastically orthotropic solids for conical indenters. Int. J. Solids. Struct., 41, 2004.
- [42] J.-Y. Delenne, V. Richefeu, and F. Radjai. Liquid clustering and capillary pressure in granular media. J. Fluid Mech., 762(5), 2015.
- [43] L.S. Dimas, T. Giesa, and M.J. Buehler. Coupled continuum and discrete analysis of random heterogeneous materials: Elasticity and fracture. J. Mech. Phys. Solids, 63, 2014. 481-490.
- [44] L. Dormieux, D. Kondo, and F.-J. Ulm. Microporomechanics. Wiley and Sons, Chichester, 2006.
- [45] L. Dormieux, A. Molinari, and D. Kondo. Micromechanical approach to the behavior of poroelastic materials. J. Mech. Phys. Solids, 50, 2002.
- [46] J. Dumais and Y. Forterre. Vegetable dynamics: The role of water in plant movements. Annu. Rev. Fluid Mech., 44, 2012. 453-478.
- [47] D. Ebrahimi, A.J. Whittle, and R. J.-M. Pellenq. Mesoscale properties of clay aggregates from potential of mean force representation of interactions between nanoplatelets. J. Chem. Phys., 140(154309), 2014.
- [48] J.D. Eshelby. The determination of the elastic field of an ellipsoidal inclusion, and related problems. Proc. R. Soc. A., 241, 1957.
- [49] R. Evans, U Marini Bettolo Marconi, and P. Tarazona. Fluids in narrow pores: Adsorption, capillary condensation, and critical points. J. Chem. Phys., 84(2376), 1986.
- [50] A. Fingerle and S. Herminghaus. Equation of state of wet granular matter. Phys. Rev. E., 77, 2008.
- [51] L. D. Gelb and K.E. Gubbins. Pore size distributions in porous glasses: A computer simulation study. Langmuir, 15(2):305–308, 1999.
- [52] J.W. Gibbs. On the equilibrium of heterogeneous substances. Trans. Conn. Acad., 3:108–248, 1878.
- [53] B.V. Gnedenko and A.N. Kolmogorov. Limit distributions for sums of independent random variables. Addison-Wesley, 1954.
- [54] G.N. Greaves, A.L. Greer, R.S. Lakes, and T. Rouxel. Poisson's ratio and modern materials. Nat. Mater., 10, 2011.
- [55] S. Hansen, A. Roux and H.J. Hermann. Rupture of central force lattices. J. Phys., 50(7):733–744, 1989.

- [56] G. Hantal, L. Brochard, H. Laubie, D. Ebrahimi, J.-M. Pellenq, F.-J. Ulm, and B. Cosane. Atomic-scale modeling of elastic and failure properties of clays. Mol. Phys.: An Int. J. Interface between Chem. Phys., 112, 2014.
- [57] C. Hellmich, J.-F. Barthelemy, and L. Dormieux. Mineral-collagen interactions in elasticity of bone ultrastructure—a continuum micromechanics approach. Eur. J. Mech. A-Solid, 23(5):783–810, 2005.
- [58] C. Hellmich, B. Pichler, and D. Adam. Poromechanics v: Proceedings of the fifth biot conference on poromechanics. Amer Society of Civil Engineers, 2013.
- [59] H. Herrmann and S. Roux. Statistical models for the fracture of disordered media. Random Materials and Processes. Elsevier Science, 1990.
- [60] A. Hershey. The elasticity of an isotropic aggregate of anisotropic cubic crystal. J. Appl. Mech., 21:226–240, 1954.
- [61] R. Hill. A self-consistent mechanics of composite materials. J. Mech. Phys. Solids, 13(4):213–222, 1965.
- [62] A. Hrennikoff. Solution of problems of elasticity by the framework method. J. Appl. Mech., 8(4):169–175, 1941.
- [63] M.H. Hubler, J. Gelb, and F.-J. Ulm. Microtexture analysis of gas shale by xrm imaging. J. Nanomech. Micromech., 7(3), 2017.
- [64] K. Ioannidou, K. Krakowiak, M. Bauchy, C. Hoover, E. Masoero, S. Yip, F.-J. Ulm, P. Levitz, R.M. Pellenq, and E. Del Gado. Mesoscale texture of cement hydrates. Proc. Natl. Acad. Sci. USA, 113(8):2029–2034, 2016.
- [65] B. Jha and R. Juanes. Coupled multiphase flow and poromechanics: A computational model of pore pressure effects on fault slip and earthquake triggering. Water Resour. Res., 50, 2014.
- [66] S.G. Johnson. The nlopt nonlinear-optimization package, 2009.
- [67] M. Kardar. Statistical physics of fields. Cambridge University Press, 2007.
- [68] M. Kardar. Statistical physics of particles. Cambridge University Press, 2007.
- [69] K. Katahara. Clay minerals elastic properties. In Proceedings of the 66th SEG Annual Meeting Expanded Technical Program Abstracts, 1996.
- [70] E. Kierlik, P.A. Monson, L. Rosinberg, L. Sarkisov, and G. Tarjus. Capillary condensation in disordered porous materials: Hysteresis versus equilibrium behavior. Phys. Rev. Lett., 87(5), 2001.
- [71] E. Kierlik, P.A. Monson, M.L. Rosinberg, and G. Tarjus. Adsorption hysteresis and capillary condensation in disordered porous solids: a density functional study. J. Phys. Condens. Matter, 14:9295–9315, 2002.

- [72] D.J. Korteweg. Sur la forme que prennent les équations du mouvements des fluides si l on tient compte des forces capillaires causés par des variations de densité considérables mais connues et sur la théorie de la capillarité dans l hypothèse d une variation continue de la densité. Archives Néerlandaises des Sciences exactes et naturelles, 6:1–24, 1901.
- [73] L. Kostaski, R. Barrios D’Ambra, and I. Iturrioz. Crack propagation in elastic solids using the truss-like discrete element method. Int. J. Fract., 174(2):139–161, 2012.
- [74] E. Kroner. Berechnung der elastischen konstanten des vielkristalls aus den konstanten des einkristalls. Zeitschrift für Physik und Chemie, 4, 1958.
- [75] G. Lamé. Leçons sur la théorie mathématique de l’élasticité des corps solides. Bachelier, Paris, 1852.
- [76] P. Larsson, A. Giannakopoulos, E. SoDerlund, D. Rowcliffe, and R. Vetergaard. Analysis of berkovich indentation. Int. J. Solids. Struct., 1996.
- [77] H. Laubie, S. Monfared, F. Radjai, R.J.-M. Pellenq, and F.-J. Ulm. Disorder-induced stiffness degradation of highly disordered porous materials. J. Mech. Phys. Solids, 106:207–228, 2017.
- [78] H. Laubie, S. Monfared, F. Radjai, R.J.-M. Pellenq, and F.-J. Ulm. Effective potentials and elastic properties in the lattice-element method: Isotropy and transverse isotropy. J. Nanomech. Micromech., 7(3), 2017.
- [79] H. Laubie, F. Radjai, R. Pellenq, and F.-J. Ulm. A potential-of-mean-force approach for fracture mechanics of heterogeneous materials using the lattice element method. J. Mech. Phys. Solids, 105:116–130, 2017.
- [80] H. Laubie, F. Radjai, R. Pellenq, and F.-J. Ulm. Stress transmission and failure in disordered porous media. Phys. Rev. Lett., 119, 2017.
- [81] N. Laws and G.J. Dvorak. The effect of fiber breaks and aligned penny-shaped cracks on the stiffness and energy release rates in unidirectional composites. Int. J. Solids. Struct., 23(9):1269–1283, 1987.
- [82] G. Lilliu and J.G.M. van Mier. 3d lattice type fracture model for concrete. Eng Fract. Mech., 70(7):927–941, 2003.
- [83] G. Lilliu, J.G.M. van Mier, and M.R.A. van Vilet. Numerical characterization of the elastic properties of heterogeneous materials with a 3d lattice model. Trans. Modell. Simul., 21:515–524, 1999.
- [84] E. Masoero, E. Del Gado, R.J.-M. Pellenq, F.-J. Ulm, and S. Yip. Nanostructure and nanomechanics of cement: polydisperse colloidal packing. Phys. Rev. Lett., 109, 2012. 3-6.

- [85] E. Masoero, E. Del Gado, R.J.-M. Pellenq, F.-J. Ulm, and S. Yip. Nano-scale mechanics of colloidal c-s-h gels. Soft Matter, 10, 2014.
- [86] G. Mavko, T. Mukerji, and J. Dvorkin. Rock Physics Handbook: Tools for Seismic Analysis in Porous media. Cambridge University Press, 2003.
- [87] M. Mehta and D.A. Kofke. Coexistence diagrams of mixtures by molecular simulation. Chem. Eng. Sci., 49, 1994.
- [88] K. Melnikov, R. Mani, F.K. Wittel, M. Thielmann, and H.J. Herrmann. Grain-scale modeling of arbitrary fluid saturation in random packings. Phys. Rev. E., 92, 2015.
- [89] E. Moeendarbary, L. Valon, M. Fritzsche, A.R. Harris, D.A. Moulding, A. Thrasher, E. Stride, L. Mahadevan, and G.T. Charras. The cytoplasm of living cells behave as a poroelastic material. Nat. Mater., 12(3), 2013. 253-261.
- [90] S. Monfared, H. Laubie, F. Radjai, M. Hubler, R.J.-M. Pellenq, and F.-J. Ulm. A methodology to calibrate and to validate effective solid potentials of heterogeneous porous media from computed tomography scans and laboratory-measured nanoindentation data. Acta. Geotech., 13(6):1369–1394, 2018.
- [91] S. Monfared, H. Laubie, F. Radjai, R.J.-M. Pellenq, and F.-J. Ulm. Mesoscale poroelasticity of heterogeneous media. J. Nanomech. Micromech., 7(4), 2017.
- [92] S. Monfared and F.-J. Ulm. A molecular informed poroelastic model for organic-rich, naturally occurring porous geocomposites. J. Mech. Phys. Solids, 88, 2016.
- [93] T. Mori and K. Tanaka. Average stress in matrix and average elastic energy of materials with misfitting inclusions. Acta Metallurgica, 21, 1973.
- [94] A.H. Nayfeh and M.S. Hefzy. Continuum modeling of three-dimensional truss-like space structures. AIAA J., 16(8):779–787, 1978.
- [95] A.N. Norris. Mechanics of elastic networks. Proc. R. Soc. A., 470, 2014.
- [96] Y.-C. Pan and T.-W. Chou. Point force solution for an infinite transversely isotropic solid. Transactions of ASME, pages 608–612, December 1976.
- [97] G.A. Pavliotis and A.M. Stuart. Multiscale Methods - Averaging and Homogeniation. Springer, 2007.
- [98] R.J.-M. Pellenq, B. Coasne, R.O. Denoyel, and O. Coussy. Simple phenomenological model for phase transitions in confined geometry. 2. capillary condensation/evaporation in cylindrical mesopores. Langmuir, 25, 2009. 1393-1402.
- [99] S. Plimpton. Fast parallel algorithms for short-range molecular dynamics. J. Comp. Phys., 117:1–19, 1995.
- [100] J.P. Poirier and A. Tarantola. A logarithmic equation of state. Phys. Earth. Planet. Int., 109, 1998.

- [101] M.J.D. Powell. A direct search optimization method that models the objective and constraint functions by linear interpolation. in Advances in Optimization and Numerical Analysis, eds. S. Gomez and J.-P. Hennart, Kluwer Academic: Dordrecht, 1994.
- [102] M.J.D. Powell. Direct search algorithms for optimization calculations. Acta Numerica, 7, 1998.
- [103] F. Radjai, M. Jean, J.-J. Moreau, and S. Roux. Force distribution in dense two-dimensional granular systems. Phys. Rev. Lett., 77, 1996.
- [104] F. Radjai, D. Wolf, M. Jean, and J.-J. Moreau. Bimodal character of stress transmission in granular packings. Phys. Rev. Lett., 80(1), 1998. 61-64.
- [105] L. Rayleigh. On the theory of surface forces.-ii. compressible fluids. Phil. Mag., 33:209–220, 1892.
- [106] J.R. Rice and M.P. Cleary. Some basic stress-diffusion solutions for fluid-saturated elastic porous media with compressible constituents. Rev. Geophys. Space Phys., 14, 1976. 227-241.
- [107] C.H. Rycroft. Voro++: A three-dimensional voronoi cell library in c++. Chaos, 19(041111), 2009.
- [108] M. Scheel, R. Seemann, M. Brinkmann, M. Di Michiel, A. Sheppard, and B. Breidenbach. Morphological clues to wet granular pile stability. Nat. Mater., 7:189–193, 2008.
- [109] E. Schlangen and E.J. Garboczi. New method for simulating fracture using an elastically uniform random geometry lattice. Int. J. Eng. Sci., 34(10):1131–1144, 1996.
- [110] E. Schlangen and E.J. Garboczi. Fracture simulations of concrete using lattice models: Computational aspects. Eng. Fract. Mech., 57(2):319–332, 1997.
- [111] J.S. Seewald. Organic-inorganic interactions in petroleum-producing sedimentary basins. Nature, 426:327–333, 2003.
- [112] S.J. Semnani and R.I. Borja. Quantifying the heterogeneity of shale through statistical combination of imaging across scales. Acta Geotech., 12, 2017. 1193-1205.
- [113] Y.-S. Seo, Y. Ichikawa, and K. Kawamura. Stress-strain response of rock forming minerals by md simulations. Mater. Sci. Res. Int., 5, 1999.
- [114] S.A. Silling and R.B. Lehoucq. Peridynamic theory of solid mechanics. Technical Report 1, Sandia National Laboratories, Albuquerque, New Mexico 87185-1322 USA, 4 2010.
- [115] J.M. Skotheim and L. Mahadevan. Physical limits and design principles for plant and fungal movements. Science, 308(5726), 2005.

- [116] R. Snurr, A. Bell, and D. Theodorou. Prediction of adsorption of aromatic hydrocarbons in silicalite from grand canonical monte carlo simulations with biased insertions. J. Phys. Chem., 97(51):13742–13752, 1993.
- [117] H.E. Stanley. Intorduction to phase transitions and critical phenomena. Clarendon Press, Oxford, 1971.
- [118] S. Succi. The Lattice Boltzmann Equation for Fluid Dynamics and Beyond. Oxford University Press, 2001.
- [119] P. Suquet. Elements of homogenization for inelastic solid mechanics. 1987.
- [120] M.L. Szulczewski, C.W. MacMinn, H.J. Herzog, and R. Juanes. Lifetime of carbon capture and storage as a climate-change mitigation technology. Proc. Natl. Acad. Sci. USA, 109(14), 2012. 5185-5189.
- [121] K. Tai, M. Dao, S. Suresh, A. Palazoglu, and C. Ortiz. Nanoscale heterogeneity promotes energy dissipation in bone. Nat. Mat., 6, 2007.
- [122] J.F. Jr. Thomas. Failure of cauchy relation in cubic metals. Acta Metall. Mater., 5:787–790, 1971.
- [123] B.P. Tissot and D.H. Welte. Petroleum formation and occurrence. Springer-Verlag, 1984.
- [124] V. Topin, J.-Y. Delenne, F. Radjai, L. Brendel, and F. Mabilie. Strength and failure of cemented granular matter. Eur. Phys. J.E., 23, 2007.
- [125] S. Torquato. Random heterogeneous materials - microstructure and macroscopic properties. Springer, 2002.
- [126] F.-J. Ulm, M. Vandamme, C. Bobko, J.A. Ortega, K. Tai, and C. Ortiz. Statistical indentation techniques for hydrated nanocomposites: concrete, bone, and shale. J. Am. Chem. Soc., 90(9):2677–2692, 2007.
- [127] M. Vandamme, L. Brochard, B. Lecampion, and O. Coussy. Adsorption and strain: The CO<sub>2</sub>-induced swelling of coal. J. Mech. Phys. Solids, 58(10), 2010.
- [128] M. Vaughan and S. Guggenheim. Elasticity of muscovite and its relationship to crystal structure. J. Geophys. Res., 91, 1986.
- [129] D. Veneziano. Computational Fluid and Solid Mechanics. Elsevier, Cambridge, Massachusetts, 2003.
- [130] W. Weibull. A statistical theory of the strength of materials. The Royal Swedish Institute of Engineering Research (Ingenors Vetenskaps Akadiens Handlingar), 151, 1939.
- [131] W. Weibull. A statistical distribution function of wide applicability. J. Appl. Mech., 18:293–297, 1951.

- [132] G. J. Weng. Some elastic properties of reinforced solids with special reference to isotropic ones containing spherical inclusions. Int. J. Eng. Sci., 22:845–856, 1984.
- [133] S. Younis, Y. Kauffmann, L. Bloch, and E. Zolotoyabko. Inhomogeneity of nacre lamellae on the nanometer length scale. Cryst. Growth Des., 12(9):4574–4579, 2012.
- [134] A. Zaoui. Continuum micromechanics: A survey. J. Eng. Mech., 8, 2002.
- [135] G.-F. Zhao, J. Fang, and J. Zhao. A 3d distinct lattice spring model for elasticity and dynamic failure. Int. J. Numer. Anal. Methods Geomech., 35(8):859–885, 2011.
- [136] E.T. Zhou, K. Ioannidou, F.-J. Ulm, M.Z. Bazant, and R. J.-M. Pellenq. Multi-scale poromechanics of wet cement paste. Proc. Natl. Acad. Sci. USA, 2019. Under review.
- [137] T. Zhou, K. Ioannidou, E. Masoero, M. Mirzadeh, Roland J.-M. Pellenq, and M. Z. Bazant. Capillary stress and structural relaxation in moist granular materials. Langmuir, 2019. in press.